SOURCE LOCALIZATION AND POWER ESTIMATION IN AEROACOUSTIC NOISE MEASUREMENTS

By

TARIK YARDIBI

A DISSERTATION PRESENTED TO THE GRADUATE SCHOOL
OF THE UNIVERSITY OF FLORIDA IN PARTIAL FULFILLMENT
OF THE REQUIREMENTS FOR THE DEGREE OF
DOCTOR OF PHILOSOPHY

UNIVERSITY OF FLORIDA

2009

To my beloved wife and my parents

ACKNOWLEDGMENTS

I would like to express my most sincere gratitude to my advisor Prof. Jian Li for the enormous help and guidance she has provided to me both technically and personally in the last three years of my life. Her endless energy and pleasant personality together with her vast technical knowledge made this graduate study a productive and enjoyable journey. I very much appreciate the opportunities and the peaceful working environment she provided me during my studies.

I am very thankful to my co-advisor Prof. Louis N Cattafesta III for his incredible support and advices. I am grateful for the many office hours he spent on discussing my research problems. He has always been an excellent leader and a very understanding person, which made the experimental part of my research a cultivating experience.

I would like to thank Prof. Mark Sheplak for serving in my committee and for his advices on various issues. I would also like to thank Prof. Henry Zmuda and Prof. Clint Slatton for serving in my committee.

I am grateful to Prof. Petre Stoica for his guidance in a wide variety of topics. It was a pleasure having the opportunity to work with such a distinguished scholar in array processing.

I would like to thank to my labmates from the Spectral Analysis Lab, Zhaofu Chen, Yubo Cheng, Lin Du, Dr. Bin Guo, Hao He, Arsen Ivanov, Jun Ling, William Roberts, Enrique Santiago, Xiang Su, Xing Tan, Duc Vu, Dr. Luzhou Xu, Ming Xue, Dr. Xiayu Zheng, and Dr. Xumin Zhu. I would also like to thank Chris Bahr, Dr. Fei Liu, Drew Wetzel, and Nikolas Zawodny from the Interdisciplinary Microsystems Group.

I am also thankful to my Master's thesis advisor Prof. Ezhan Karasan, and to Prof. Defne Aktas, Prof. Tolga Duman and Prof. Tugrul Dayar for their supports and helps that made it possible for me to enter graduate school in the first place.

My love, Ozlem, you know I could not have survived here (or anywhere) without you and your support. I hope that one day we can read these lines and smile to the challenges and hardships we had to face in a country far far away from our homes. Don't forget that I (Ben) love (seni) you (seviyorum)!

I cannot forget about my dear friends back at home: Emre Alsahan, Erman Kayakesen, Utku Harpaslan, Fatih Demir, Nida Berberoglu, Sinan Tasdelen, and many more that were always there for me even though I could only see them every once in a while. I am also thankful to Murat Keceli and Sevnur Komurlu Keceli for their friendships in Gainesville.

Finally, a special thanks goes to my mom Hatice Yardibi, my dad Cengiz Yardibi, my sister Emine Nur Yardibi and my parents-in-law Fatma and Osman Subakan. Also, a belated thank you to Erkan Yardibi for his helps in my undergraduate senior project.

This work was supported by the National Aeronautics and Space Administration (NASA) under Grant No. NNX07AO15A.

TABLE OF CONTENTS

LIST OF TABLES

LIST OF FIGURES

Abstract of Dissertation Presented to the Graduate School
of the University of Florida in Partial Fulfillment of the
Requirements for the Degree of Doctor of Philosophy

SOURCE LOCALIZATION AND POWER ESTIMATION
IN AEROACOUSTIC NOISE MEASUREMENTS

By

Tarik Yardibi

August 2009

Chair: Jian Li
Major: Electrical and Computer Engineering

Using microphone arrays for noise source localization and power estimation has become common practice in aeroacoustic measurements, with the ultimate goal being the development of acoustic treatments to reduce overall airframe noise. This dissertation discusses the challenges involved in aeroacoustic testing with microphone arrays and develops a number of new signal processing techniques to overcome these challenges. The proposed algorithms are validated using both simulations and experimental data acquired at the University of Florida Aeroacoustic Flow Facility (UFAFF) with a 63-element microphone array.

The standard delay-and-sum (DAS) beamformer is the most widely employed beamforming algorithm due to its simplicity and robustness, although it suffers from high sidelobe level and low resolution problems. Deconvolution can be used to eliminate the effects of the array response function from the DAS estimates. In this dissertation, the deconvolution problem is carried onto the sparse signal representation area and a sparsity constrained deconvolution approach (SC-DAMAS) as well as a sparsity preserving covariance matrix fitting approach (CMF) area presented. These algorithms are shown to offer better performance than several existing methods.

Next, a systematic experimental analysis of DAS, deconvolution approach for the mapping of acoustic sources (DAMAS), SC-DAMAS, CMF, and CLEAN based on spatial source coherence (CLEAN-SC) is presented using uncorrelated and coherent sources as

well as a NACA Mod 63-215 Mod B airfoil model. The source localization and absolute signal power estimation performance of the aforementioned algorithms are analyzed.

To deal with correlated sources, the CMF-C algorithm, which is an extension to CMF, is proposed as an alternative to DAMAS-C, which is the extension of DAMAS to the correlated case. Since DAMAS-C and CMF-C are computationally impractical, an alternative algorithm, named mapping of acoustic correlated sources (MACS), is also presented. MACS is shown to work with simulated and experimental data containing correlated (or coherent) sources within a reasonable amount of time.

Furthermore, a systematic uncertainty analysis of the DAS beamformer and a widely used array calibration procedure is presented. It is shown using experimental data that the uncertainties in the DAS beamformer integrated levels can be expected to be larger than about ± 1 dB. It is also shown that the array calibration procedure is essential when the assumed steering vectors are expected to contain errors.

Most existing array processing algorithms for aeroacoustic noise measurement applications assume the presence of monopole sources. The last chapter of the dissertation addresses the problem of directive sources with unknown steering vectors. An algorithm for estimating non-diagonal measurement noise covariance matrices is also presented in this chapter as an alternative to diagonal removal.

CHAPTER 1
INTRODUCTION

Due to the ever-increasing demand for commercial air transportation, airports have to accommodate more airplanes every year. This results in increased noise pollution and disturbance to the nearby residents, and, accordingly, stricter regulations on airplane noise levels are being imposed to address this problem. Although the dominant noise component of an airplane is the jet engines during take-off, the airframe noise is especially significant while an airplane is landing since the engines are usually in low thrust mode during this phase. As noise can be the determining factor on the number of airplanes that can be accommodated during a certain time period in some airports, it is essential to accurately localize and estimate the strengths of dominant airframe noise components, in an attempt to develop acoustic treatments for reducing overall airframe noise. For this purpose, it is important to both provide systematic analyses of existing measurement and data reduction methodologies for aeroacoustic measurements and develop novel signal processing techniques that can mitigate the shortcomings of the existing techniques.

The use of microphone arrays for noise source localization and power estimation has become common practice in aeroacoustic measurements in the recent years. As opposed to using a single microphone, microphone arrays can be electronically steered into desired regions in space to create an image of acoustic sources at a given frequency [1, 2]. This image consists of the estimated sound pressure level of each scanning grid point on the model under investigation and can be used to identify the model components primarily responsible for the generated noise. A typical microphone array consists of a number of microphones arranged in a certain geometry, which is carefully designed to meet given 3-dB beamwidth and sidelobe specifications within a frequency range of interest. Figure 1-1 A shows an example microphone array, the small aperture directional array (SADA) [1, 3, 4] which consists of 33 microphones; a microphone is placed at the center of the array and the others are arranged in four circular rings of 8 microphones each. This array,

being relatively small in aperture, is mainly used for measuring source directivity and is designed for the frequency range of 10 kHz to 40 kHz. Since the resolution of an array decreases with decreasing frequency for a given aperture size, a larger array is required in order to achieve sufficient resolution at lower frequencies. An example of such a large aperture array is the large aperture microphone directional array (LAMDA) shown in Figure 1-1 B, which consists of 63 microphones arranged in a logarithmic spiral structure. LAMDA can be effectively utilized at frequencies as low as 1 kHz. The logarithmic spiral layout of the microphones results in lower sidelobe levels compared to a circular layout (see [5, 6] for a detailed treatment on array design).

1.1 Notation

The following notations will be used throughout this dissertation. Vectors and matrices are denoted by boldface lowercase and boldface uppercase letters, respectively. The kth component of a vector $\mathbf{x}$ is written as x_k. The kth diagonal element of a matrix $\mathbf{P}$ is written as P_k and $\hat{\mathbf{s}}$ denotes the estimate of $\mathbf{s}$. See Table 1-1 for other symbols and their meanings. All sound pressure levels (SPLs) presented in this dissertation are in dB ref. 20 μPa.

1.2 Background

The most commonly used beamforming algorithm in practice is the delay-and-sum (DAS) beamformer [1, 2, 4, 6–8] which sums the delayed and weighted versions of each microphone signal so that the actual source signals are reinforced and the unwanted noise signals tend to cancel. A well-known issue with the classical delay-and-sum approach is that the beamforming maps are usually contaminated with large sidelobes. Sidelobes can cause both the smearing and leakage of the sources [8, 9]. Consider a scenario with two closely spaced sources so that the response of the array to the first source does not wither away before the response to the second source starts. This will result in the smoothing, or smearing, of the spectrum in the sense that the two peaks will be merged into a single broad peak. Looking from a different perspective, a strong source can yield power at other

locations, where no source is present, through the convolution with the sidelobes. This latter form of degradation is called leakage. Therefore, it is usually difficult to identify the true source locations and strengths through the beamforming map obtained via the DAS method. Another problem with DAS is that the beamwidth tends to increase with decreasing frequency.

Various other microphone array processing methods have been developed in order to mitigate the drawbacks of the DAS beamformer. Weighting schemes that maintain a constant beamwidth over a frequency range when used in conjunction with the DAS beamformer have been discussed in the literature [10, 11]. Also, several robust adaptive beamforming techniques have been proposed as alternatives to DAS [12–16]. Most of these techniques are parametric approaches that require the number of sources to be known [15, 16], and Capon type beamformers cannot provide a sparse representation of the imaging scene and fail to work for coherent sources [12].

In order to remedy the sidelobe problem of the DAS beamformer, a post processing technique called the deconvolution approach for the mapping of acoustic sources (DAMAS) was developed [17, 18]. This approach is considered a breakthrough in aeroacoustic measurements and has been used widely in practice. Assuming that the source waveforms are uncorrelated, it can be shown that the DAS data reduction equation is a linear function of the actual signal powers and the coefficients of this linear function are known. DAMAS solves this inverse problem for the signal powers after evaluating the DAS data reduction equation at every scanning point. Due to the matrix involved in this linear system being ill-conditioned (matrix inverse does not exist), DAMAS uses the iterative Gauss-Seidel method. One drawback of using the Gauss-Seidel method for solving this linear system of equations is computation time. (The number of iterations required by the Gauss-Seidel was reported to be on the order of thousands [18].) Many other algorithms related to DAMAS have been proposed in the literature [19]. Localization and optimization of array results (LORE) [20] is a deconvolution method that uses a

two stage process to solve the inverse problem. In the first step a method similar to DAMAS is used to reduce the problem dimensions and in the second step an optimization scheme is used to solve the reduced inverse problem. DAMAS2 and DAMAS3 [21] offer alternatives and extensions to DAMAS by using the fast Fourier transform (FFT) and assuming that the point spread function is shift-invariant. DAMAS has also been applied to the three dimensional source localization problem [22]. Aside from the aforementioned deconvolution algorithms, CLEAN based on spatial source coherence (CLEAN-SC) is another widely used algorithm which, unlike the above algorithms, does not assume the true steering vectors to be known. Instead, CLEAN-SC iteratively builds up the steering vectors corresponding to the dominant sources using the previously estimated signal powers and assuming that the sidelobes are coherent with the peak for a given source. After estimating the steering vectors and the signal powers, CLEAN-SC constructs a clean image of the scanning region similar to the original CLEAN algorithm [23]. One drawback of CLEAN-SC is that it requires the selection of four user parameters (a wrong selection could result in poor performance), whereas DAMAS is a user parameter-free algorithm. All of the aforementioned algorithms assume that the sources are uncorrelated and the literature on the deconvolution of correlated sources is sparse to the best of the author's knowledge. DAMAS-C [24] extends DAMAS to the correlated case using a very similar methodology and assuming that the cross-correlation between any two sources is real-valued. Although requiring high computational resources, this approach is the first deconvolution algorithm considering correlated sources in aeroacoustic measurements.

In this dissertation, we make use of the sparse signal representation framework several times and therefore we find it useful to review the background on this subject before describing our contributions. Sparse signal representation is an extensively studied topic in many areas including statistics and signal processing for the recovery of signals consisting of only few nonzero elements with a known linear relation to the measured data. The sparse signal representation problem mainly aims to find the sparsest $\bar{\mathbf{x}}$ such

that $\bar{\mathbf{y}} = \bar{\mathbf{A}}\bar{\mathbf{x}}$ is satisfied. Stated more formally, the objective is to minimize $\|\bar{\mathbf{x}}\|_0$ such that $\bar{\mathbf{y}} = \bar{\mathbf{A}}\bar{\mathbf{x}}$ where $\bar{\mathbf{A}}$ is known and $\bar{\mathbf{y}}$ is measured. The problem in its original form is a combinatorial problem and has an exponential complexity making it impractical [25]. Fortunately, when $\bar{\mathbf{x}}$ is sufficiently sparse [25], $\|\bar{\mathbf{x}}\|_0$ can be replaced by $\|\bar{\mathbf{x}}\|_1$ which leads to a convex optimization problem that can be solved much more easily using least absolute shrinkage and selection operator (LASSO) [26] or basis pursuit (BP) [27, 28] type of algorithms. There are many studies in the literature elaborating on this relaxation from the ℓ_0-norm to the ℓ_1-norm both in the noiseless and noisy case [25, 29–31]. It is shown that when $\bar{\mathbf{x}}$ contains a small number of nonzero elements with respect to its size, the solutions with the ℓ_0- and ℓ_1-norms coincide under some mild conditions. Alternatively, the focal underdetermined system solution (FOCUSS) [32–35] algorithm can be used to iteratively solve the sparse problem by minimizing a cost function that promotes sparsity. This method requires the proper selection of two user parameters. Nevertheless, FOCUSS algorithms have been successfully applied to brain electroencephalography (EEG) signals and far-field source localization problems. A Bayesian approach, such as sparse Bayesian learning (SBL) [36–38] or the approach in [39], can also be used to estimate $\bar{\mathbf{x}}$ using various prior probability distributions to enforce sparsity. Although these approaches do not require a user parameter, they usually have high computational complexity. Note that LASSO can also be thought of as a Bayesian approach assuming a Gaussian likelihood for $\bar{\mathbf{y}}$ and a Laplacian prior for $\bar{\mathbf{x}}$ which is known to enforce sparsity. Another algorithm, the ℓ_1-SVD algorithm [40–43], where SVD stands for the matrix singular value decomposition, is proposed for estimating source locations in a manner similar to BP but for the multiple snapshot and complex case. This algorithm requires an estimate for the number of sources. Although this estimate does not have to be exact, a small error is required for good performance. More importantly, this algorithm contains a user parameter whose selection is very difficult and could result in significant performance loss when tuned improperly [44]. Note that this method is designed to work with the time signals. In aeroacoustic

applications, however, huge amounts of time data are collected and it is preferred to work with the covariance matrix since it requires much less storage space and is more convenient to deal with. Finally, Fuchs [45] also discusses methods for the recovery of source locations for the far-field linear array case by appending a noise basis vector to the steering matrix and using deconvolution together with sparsity. It is interesting to note that these approaches in the signal processing literature are similar to DAMAS. Fuchs also provides an extension to his method by using a uniform circular array and a sparse algorithm similar to BP [46]. In this method, the user parameter is selected to be a constant, which can introduce errors.

1.3 Organization of the Dissertation

The dissertation begins by formulating the aeroacoustic source localization and power estimation problem in Chapter 2. The widely used DAS beamformer and a popular array calibration method [2] is also presented in this chapter.

Chapter 3 describes deconvolution approaches for uncorrelated sources. After reviewing DAMAS, we describe the sparsity constrained DAMAS algorithm (SC-DAMAS), which is an application of a slightly modified version of LASSO to the specific inverse problem of DAMAS. In contrast to selecting a constant [46], the user parameter of SC-DAMAS is selected by an adaptive and simple method which uses the eigenvalues of the cross spectral matrix (CSM). We also discuss a way to significantly speed up SC-DAMAS. Moreover, we propose another algorithm called the covariance matrix fitting (CMF), which also exploits sparsity for deconvolution but in a different way than the DAMAS formulation. Both SC-DAMAS and CMF are formulated as convex optimization problems. These algorithms are guaranteed to converge to the globally optimal solution and they take less computation time than DAMAS. The CMF algorithm is more robust to noise than both DAMAS and SC-DAMAS. We provide numerical examples that demonstrate the performance of the proposed algorithms.

Chapter 4 provides a systematic comparison of DAS, DAMAS, SC-DAMAS, CMF and CLEAN-SC using experimental data acquired at the University of Florida Aeroacoustic Flow Facility (UFAFF) using LAMDA [47]. The test cases considered include a single source, two uncorrelated sources with similar and different powers, and two coherent sources. The source localization capability of the algorithms as well as their accuracy in estimating the absolute signal powers will be analyzed.

In Chapter 5, we extend our analysis to deal with correlated (or even coherent) sources. We first propose CMF-C, which is an extension of CMF to the correlated case. However, DAMAS-C and CMF-C require extreme computation times for even small number of scanning points. Therefore, we present a new covariance fitting approach for the mapping of acoustic correlated sources (MACS). MACS is a cyclic algorithm based on convex optimization and sparsity, and can work with uncorrelated, partially correlated or even coherent sources with a reasonably low computational complexity. It is shown via simulations as well as experimental data that MACS can successfully localize correlated acoustic sources and estimate both the auto-correlation level of each source and the cross-correlation levels between the sources.

Chapter 6 provides a systematic uncertainty analysis of the DAS beamformer and the array calibration procedure under the assumption that the underlying mathematical model of uncorrelated, monopole sources is correct. An analytical multivariate method based on a first-order Taylor series expansion and a numerical Monte-Carlo method based on assumed uncertainty distributions for the input variables are considered. The uncertainty of calibration is analyzed using the Monte-Carlo method, whereas the uncertainty of the DAS beamformer is analyzed using both the complex multivariate and the Monte-Carlo methods. It is shown that the array calibration procedure is essential when errors in the assumed steering vectors are expected. It is also shown using experimental data that the uncertainty in the DAS power estimates can be as large as ± 1 dB (and even larger at high frequencies).

Most existing array processing algorithms for aeroacoustic noise measurement applications assume the presence of monopole sources. In Chapter 7, an eigenvalue decomposition based algorithm for the localization of directive sources with unknown steering vectors is presented. Since subspace methods are sensitive to measurement noise, an iterative algorithm that makes use of convex programming for extracting the measurement noise covariance matrix, which can be either diagonal or non-diagonal, from the array covariance matrix is also presented. Numerical examples are provided to validate the proposed algorithms.

Finally, the dissertation is concluded in Chapter 8 where a discussion on potential future research directions is also provided.

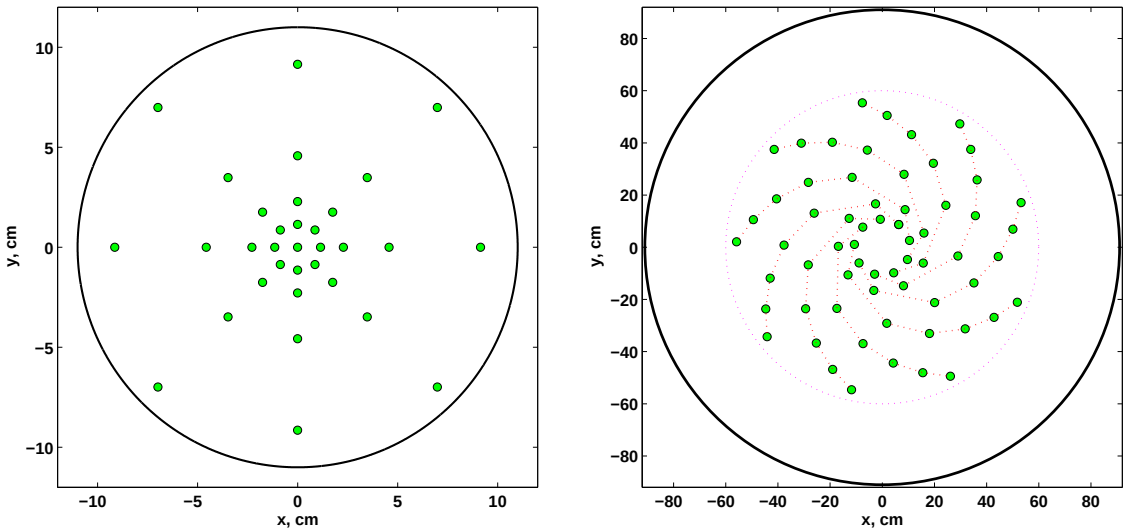

Figure 1-1. The microphone layouts of two arrays. A) SADA with 33 microphones. B) LAMDA with 63 microphones.

Table 1-1. Mathematical notation used in the dissertation.

Notation	Explanation
$\mathrm{E}[\cdot]$	Expectation operation
$\lvert \cdot \rvert$	Absolute value of a scalar
$\lVert \cdot \rVert_0$	ℓ_0-norm, i.e., the number of non-zero elements of a vector
$\lVert \cdot \rVert_1$	ℓ_1-norm, i.e., the sum of the absolute value of each element in a vector
$\lVert \cdot \rVert_2$	ℓ_2-norm
$\lVert \cdot \rVert_{\mathrm{F}}$	Frobenius norm of a matrix
$\odot$	The Hadamard (elementwise) matrix product
$\mathrm{tr}(\cdot)$	Trace of a matrix
$(\cdot)^*$	Complex conjugate of a scalar
$(\cdot)^T$ and $(\cdot)^H$	Transpose and conjugate transpose of a vector or matrix
$\mathbf{P} \succeq 0$	$\mathbf{P}$ is a positive semi-definite matrix
$\mathrm{vec}(\cdot)$	The column-by-column vectorization of a matrix
$\mathbb{R}^{n_r \times n_c}$ and $\mathbb{C}^{n_r \times n_c}$	Real and complex matrices with n_r rows and n_c columns
$\mathbf{I}$	Identity matrix of appropriate dimension
$\mathrm{Re}[\cdot]$ and $\mathrm{Im}[\cdot]$	Real and imaginary parts of the argument
$\mathrm{diag}(\cdot)$	A diagonal matrix with the vector argument in its diagonal

CHAPTER 2
FUNDAMENTALS OF BEAMFORMING

In this chapter we introduce the traditional data model used in aeroacoustic measurements, and describe the standard DAS beamforming algorithm and the array calibration procedure introduced by Dougherty [2].

2.1 Data Model

Consider the wave field generated by L monopole acoustic sources where the three-dimensional location of the lth source is denoted by $(\tilde{x}_l, \tilde{y}_l, \tilde{z}_l)$ for $l = 1, \ldots, L$. The data reduction process for frequency domain beamforming starts with the computation of the CSM at each frequency of interest. For this purpose, the pressure data recorded at each microphone for T_{acq} seconds is divided into v percent overlapping blocks of length H, where $0 \leq v < 100$. The resulting number of blocks, B, can be computed as follows:

$$B = \left\lfloor 1 + \frac{T_{\text{acq}} f_s / H - 1}{1 - v/100} \right\rfloor, \tag{2–1}$$

where $\lfloor \cdot \rfloor$ denotes the nearest integer less than or equal to the argument and f_s denotes the sampling frequency. Next, the H-point FFT of each block is computed (an appropriate spectral window can be applied to the data before taking the Fourier transforms), where H is a power of 2. This results in a frequency resolution of f_s/H. The hth element of each frequency domain block corresponds to the narrow-band frequency $f_h = h f_s / H$, where $h = 0, \ldots, H/2$ and only the single-sided spectrum is considered.

Consider an M-element microphone array with the mth microphone located at (x_m, y_m, z_m), where $m = 1, \ldots, M$. Let the frequency of interest be f. Following the spherical wave propagation model [48], the frequency domain pressure data at all the microphones can be used to obtain the following set of equations (see Figure 2-1) [7–9]

$$\mathbf{y}(b) = \sum_{l=1}^{L} \mathbf{a}_l s_l(b) + \mathbf{e}(b), \quad b = 1, \ldots, B, \tag{2–2}$$

where

$$\mathbf{y}(b) = \begin{bmatrix} y_1(b) \\ y_2(b) \\ \vdots \\ y_M(b) \end{bmatrix}, \ \mathbf{a}_l = \begin{bmatrix} e^{-jkr_{l,1}}/r_{l,1} \\ e^{-jkr_{l,2}}/r_{l,2} \\ \vdots \\ e^{-jkr_{l,M}}/r_{l,M} \end{bmatrix}, \ \mathbf{e}(b) = \begin{bmatrix} e_1(b) \\ e_2(b) \\ \vdots \\ e_M(b) \end{bmatrix}, \tag{2–3}$$

$y_m(b)$ is the frequency domain pressure data of microphone m at block b, $\mathbf{a}_l$ is the steering vector (or the wave propagation vector) corresponding to the lth monopole source, $r_{l,m} = \sqrt{(\tilde{x}_l - x_m)^2 + (\tilde{y}_l - y_m)^2 + (\tilde{z}_l - z_m)^2}$ is the Euclidean distance between the lth source and the mth microphone, $k = 2\pi f/c$ is the wavenumber, c is the speed of sound in air, $s_l(b)$ is the acoustic waveform of the lth source at block b, and $e_m(b)$ is the additive contamination (or measurement) noise (due to electronic noise and acoustic sources other than the L sources considered as well as reflections and scattering) at the mth microphone at block b. Note that $\{\mathbf{y}(b)\}$, $\mathbf{a}_l$ and $\{\mathbf{e}(b)\}$ are all complex vectors of size $M \times 1$, and $\{s_l(b)\}$ are complex scalars. In addition, $\{\mathbf{y}(b)\}$ and $\mathbf{a}_l$ are known, whereas $\{s_l(b)\}$ and $\{\mathbf{e}(b)\}$ are unknown quantities. Note also that the indices l, m and b run from 1 to L, M and B, respectively.

Eq. 2–2 can also be written in a more compact form as

$$\mathbf{y}(b) = \mathbf{A}\mathbf{s}(b) + \mathbf{e}(b), \quad b = 1, \ldots, B, \tag{2–4}$$

where $\mathbf{A} = [\mathbf{a}_1, \ldots, \mathbf{a}_L] \in \mathbb{C}^{M \times L}$ and $\mathbf{s}(b) = [s_1(b), \ldots, s_L(b)]^T \in \mathbb{C}^{L \times 1}$.

2.2 Delay-and-Sum Beamformer

The DAS beamformer basically sums the delayed and weighted versions of each microphone signal in order to reinforce the signal from the source of interest while suppressing the contribution from other sources and contamination noise. The delays and weights are designed according to the relative distances between the microphones. In the frequency domain, this corresponds to applying appropriate phase shifts and weighting factors. Beamforming is usually done independently at each narrow-band frequency

of interest and therefore in the following analysis, we will consider only one particular frequency f or, equivalently, one particular wavenumber k (the same analysis is repeated at all frequencies of interest). The DAS estimate of the lth source waveform is defined as [1, 17]

$$\tilde{s}_l(b) = \frac{1}{M}\tilde{\mathbf{a}}_l^H \mathbf{y}(b), \quad l = 1, \ldots, L,\ b = 1, \ldots, B, \tag{2–5}$$

where

$$\tilde{\mathbf{a}}_l = \frac{1}{r_{l,0}} \left[r_{l,1} e^{-jkr_{l,1}}, r_{l,2} e^{-jkr_{l,2}}, \ldots, r_{l,M} e^{-jkr_{l,M}} \right]^T, \tag{2–6}$$

$r_{l,0} = \sqrt{(\tilde{x}_l - \bar{x})^2 + (\tilde{y}_l - \bar{y})^2 + (\tilde{z}_l - \bar{z})^2}$ is the distance from the lth scanning point to the array center, and $\bar{x}$ is the x component of the array center ($\bar{y}$ and $\bar{z}$ are defined similarly). Note that $\tilde{\mathbf{a}}_l$, which is an $M \times 1$ complex vector that is known, is used to account for the different distances traveled by the wave before reaching each microphone. The purpose of normalizing $\tilde{\mathbf{a}}_l$ by $r_{l,0}$ is to match the estimated signal power to what a single microphone in the center of the array would measure. The underlying assumption behind DAS is that while $r_{l,0}\tilde{\mathbf{a}}_l^H \mathbf{a}_l = M$, $r_{l',0}\tilde{\mathbf{a}}_{l'}^H \mathbf{a}_l$ is relatively small for $l' \neq l$, $l, l' = 1, \ldots, L$. This assumption is evaluated by analyzing the so-called point spread function, psf(l), defined as $|\tilde{\mathbf{a}}_l^H \mathbf{a}_0|/M^2$ for the lth scanning point where $\mathbf{a}_0$ denotes the steering vector of a source located at the center of the scanning region. The psf is also used to compute the 3-dB beamwidth (and the resolution) of the array.

Consequently, DAS estimates the power level of the lth source (as measured at the array center) as follows

$$\hat{P}_l^{(\text{D})} = \frac{2}{\omega_0 B} \sum_{b=1}^{B} |\tilde{s}_l(b)|^2 = \frac{1}{M^2}\tilde{\mathbf{a}}_l^H \mathbf{G} \tilde{\mathbf{a}}_l, \quad l = 1, \ldots, L, \tag{2–7}$$

where ω_0 is the spectral window correction factor and

$$\mathbf{G} = \frac{2}{\omega_0 B} \sum_{b=1}^{B} \mathbf{y}(b)\mathbf{y}^H(b) \tag{2–8}$$

is the CSM. (The factor of 2 is due to the use of the single-sided spectrum.) The CSM is a $M \times M$ complex symmetric matrix and hence consists of M^2 real-valued distinct components. In general, it is preferable to work with the CSM, $\mathbf{G}$, and Eq. 2–7 rather than the frequency domain pressure data, $\{\mathbf{y}(b)\}$, and Eq. 2–5 as the CSMs require much less storage space and are more convenient for analysis.

In practice, a scanning grid that covers the region of interest with a certain resolution is constructed and every point of this grid is considered as a potential source whose power will be estimated (see Figure 2-2). As a result, a beamforming map (or image) that shows the signal powers at each scanning point will be obtained. Consequently, L is considered to be the number of scanning points instead of the number of sources.

In general, each of the array microphones do not possess flat frequency response with zero phase, and this is accounted for via a frequency-dependent diagonal calibration matrix $\tilde{\mathbf{D}} = \mathrm{diag}(\tilde{D}_1, \ldots, \tilde{D}_M) \in \mathbb{C}^{M \times M}$, where $\tilde{D}_m$ denotes the complex correction factor for microphone m. The calibrated DAS data reduction equation then becomes

$$\hat{P}_l^{(\mathrm{D})} = \frac{1}{M^2} \tilde{\mathbf{a}}_l^H \tilde{\mathbf{D}} \mathbf{G} \tilde{\mathbf{D}}^H \tilde{\mathbf{a}}_l, \quad l = 1, \ldots, L. \tag{2–9}$$

Note that if a microphone is known to be problematic, simply placing a 0 in the corresponding diagonal entry of $\tilde{\mathbf{D}}$ and changing M to $M - 1$ will prevent it from propagating through the data reduction equation. The next subsection describes how $\tilde{\mathbf{D}}$ can be obtained in practice.

2.3 Array Calibration

In order for DAS to give accurate source location and strength estimates, the assumed steering vectors have to be close to the true ones. Errors in microphone locations and temperature (through its effect on the sound speed) can have major effects on the DAS signal power estimates, especially at relatively high frequencies, since these errors are multiplied by the wavenumber before propagating through the DAS data reduction equation. This section describes a widely used calibration procedure introduced by

Dougherty [2] to remedy this problem. The calibration setup consists of a speaker that resembles a point source and is driven with a broadband signal (or a tonal signal where the tone frequency is varied). The speaker is placed near the model location and a temporary anechoic enclosure is recommended for a hardwall wind tunnel to minimize source reflections [2]. Array data is collected with no flow and the resulting CSM is analyzed at each frequency to obtain frequency-dependent complex correction factors for all the microphones.

Theoretically, the measurements in the presence of a single source are modeled as (see Eq. 2–2)

$$\mathbf{y}(b) = \mathbf{a}_{\text{cal}} s_{\text{cal}}(b), \quad b = 1, \ldots, B, \tag{2–10}$$

where $\mathbf{a}_{\text{cal}}$ is the actual steering vector (unknown) corresponding to the location of the calibration speaker, $s_{\text{cal}}(b)$ is the calibration speaker waveform (unknown) and the noise term $\mathbf{e}(b)$ is neglected. According to Eq. 2–8, the CSM becomes

$$\mathbf{G}_{\text{cal}} = P_{\text{cal}} \mathbf{a}_{\text{cal}} \mathbf{a}_{\text{cal}}^H, \tag{2–11}$$

where P_{cal} is the signal power of the calibration speaker. Since $\mathbf{G}_{\text{cal}}$ is an outer product (and hence rank-1), it has only a single non-zero eigenvector equal to $\boldsymbol{\lambda}_{\text{cal}} = \mathbf{a}_{\text{cal}} e^{j\phi} / \|\mathbf{a}_{\text{cal}}\|_2$ and a single non-zero eigenvalue equal to $v_{\text{cal}} = P_{\text{cal}} \|\mathbf{a}_{\text{cal}}\|_2^2$, where $0 \leq \phi \leq 2\pi$ is an arbitrary phase value. In practice, although the remaining eigenvalues will not be identically zero, the dominant eigenvalue is expected to be noticeably larger with a good quality speaker that produces sufficient sound [2]. The measurement of the mth microphone is then scaled by the complex coefficient

$$\tilde{D}_m = \frac{(\boldsymbol{\lambda}_{\text{theory}})_m}{(\boldsymbol{\lambda}_{\text{cal}})_m}, \quad m = 1, \ldots, M, \tag{2–12}$$

where $(\cdot)_m$ denotes the mth element of the vector argument, $\boldsymbol{\lambda}_{\text{theory}} = \mathbf{a}_{\text{theory}} / \|\mathbf{a}_{\text{theory}}\|_2$, and $\mathbf{a}_{\text{theory}}$ is given by Eq. 2–3 where $r_{l,m}$ is replaced by the distance between the calibration speaker and the mth microphone. It is assumed that $\|\mathbf{a}_{\text{cal}}\|_2 \approx \|\mathbf{a}_{\text{theory}}\|_2$

and therefore

$$\mathbf{y}_{\text{calibrated}}(b) = \tilde{\mathbf{D}}\mathbf{y}(b) = \frac{\|\mathbf{a}_{\text{cal}}\|_2 e^{-j\phi}}{\|\mathbf{a}_{\text{theory}}\|_2}\mathbf{a}_{\text{theory}} s_{\text{cal}}(b) \approx e^{-j\phi}\mathbf{a}_{\text{theory}} s_{\text{cal}}(b), \quad b = 1, \ldots, B. \quad (2\text{–}13)$$

The constant phase offset $e^{-j\phi}$ will disappear when the power levels are considered. The reason for the normalization $\|\mathbf{a}_{\text{cal}}\|_2/\|\mathbf{a}_{\text{theory}}\|_2$ is because only v_{cal} is known in practice and not $\mathbf{a}_{\text{cal}}$ or $\|\mathbf{a}_{\text{cal}}\|_2$ (i.e., there is a scaling ambiguity). An important aspect of the calibration is that it will correct the phase mismatch perfectly for the calibration data. As the distance between the beamforming source (during testing) and the calibration speaker locations increase, the benefit of calibration is expected to degrade [2].

The calibration procedure described above corrects the frequency response differences between the microphones. An additional step can be employed where an overall array correction factor is obtained with respect to a reference microphone that is assumed to be calibrated separately. Note that the dominant eigenvalue of the calibrated CSM, $\tilde{\mathbf{D}}\mathbf{G}_{\text{cal}}\tilde{\mathbf{D}}^H$, is approximately $v = P_{\text{cal}}M/r_c^2$, where r_c is the distance from the calibration speaker to the array center, and the reference microphone will measure $P_{\text{ref}} = P_{\text{cal}}/r_{\text{ref}}^2$, where r_{ref} is the distance from the calibration speaker to the reference microphone. The overall array correction factor is then given as

$$P_{\text{ref}}\left(\frac{r_{\text{ref}}}{r_c}\right)^2 \frac{M}{v}. \quad (2\text{–}14)$$

Therefore, at each frequency, M complex-valued correction factors (see Eq. 2–12) will be used to scale the microphone measurements and a single real-valued correction factor (see Eq. 2–14) will be used to scale the final array estimated power levels.

When all the assumptions mentioned above are met, calibration will provide accurate correction factors for a source near the calibration speaker location. However, in practice, many sources of uncertainty are present during calibration. Errors in CSM and reference microphone levels are two such uncertainty sources. In addition, it might be easier to measure the distance between the calibration speaker and the array than it is to measure

the distance between a complex test model and the array. This will cause uncertainties in the array broadband distance, which is the distance from the array center to the center of the scanning region, for which calibration cannot account. We will consider these uncertainties in detail in Chapter 6.

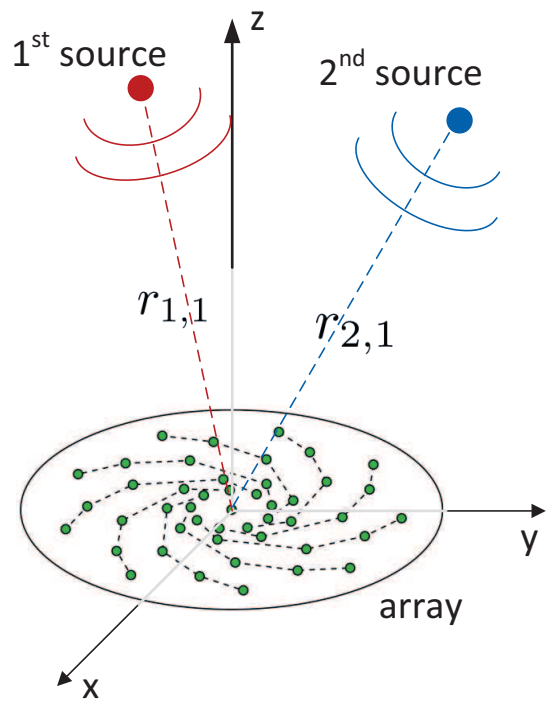

Figure 2-1. A microphone array extending in the xy-plane with M microphones (shown by the circles) and in the presence of two near-field acoustic sources. The microphone at the array center is assumed to be indexed by $m = 1$ in this figure.

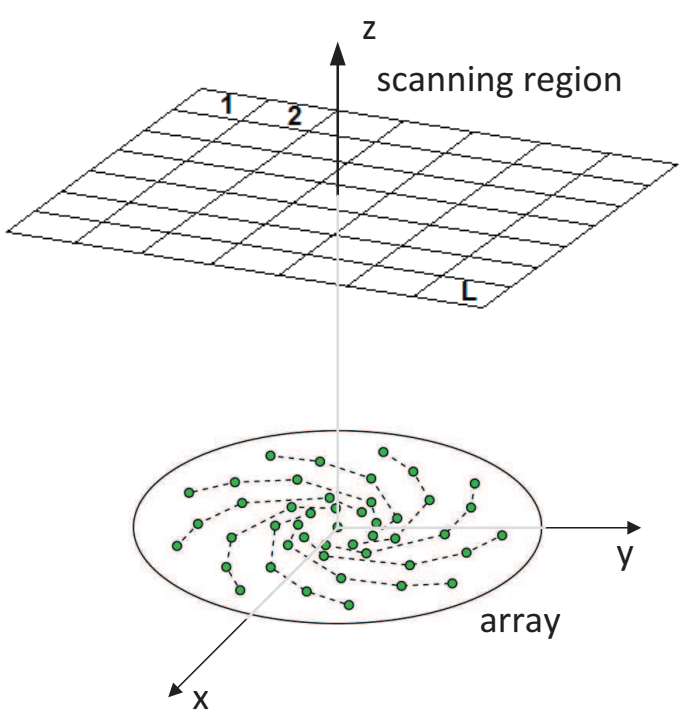

Figure 2-2. A scanning region with a given resolution is used to obtain a beamforming image by steering the array at each of the L grid points.

CHAPTER 3
DECONVOLUTION WITH UNCORRELATED SOURCES

Assume that the measurement noise $\{\mathbf{e}(b)\}$ and acoustic signals $\{\mathbf{s}(b)\}$ are independent and have zero-mean values. Then,

$$\mathrm{E}[\mathbf{s}(b)\mathbf{e}^H(b)] = \mathrm{E}[\mathbf{e}^H(b)\mathbf{s}(b)] = 0. \tag{3–1}$$

Furthermore, when the measurement noise is white with power σ^2, i.e., $\mathrm{E}[\mathbf{e}(b)\mathbf{e}^H(b)] = \sigma^2\mathbf{I}$, the array covariance matrix, denoted as $\mathbf{G} \in \mathbb{C}^{M\times M}$, can be written as (see Eq. 2–4):

$$\mathbf{G} = \mathrm{E}[\mathbf{y}(b)\mathbf{y}^H(b)] = \mathbf{APA}^H + \sigma^2\mathbf{I}, \tag{3–2}$$

where $\mathbf{P} = \mathrm{E}[\mathbf{s}(b)\mathbf{s}^H(b)] \in \mathbb{C}^{L\times L}$ is the signal covariance matrix. Since $\mathbf{G}$ is not available in practice, it is replaced by the CSM, $\hat{\mathbf{G}}$, which was defined in Eq. 2–8.

The acoustic signals are assumed to be uncorrelated when the correlation between any two sources is small compared to the auto-correlation of the sources, i.e., when

$$\left|\frac{1}{B}\sum_{b=1}^{B} s_l(b)s_{l'}^*(b)\right| \ll \frac{1}{B}\sum_{b=1}^{B}|s_l(b)|^2, \quad l \neq l',\ \ l,l' = 1,\ldots,L, \tag{3–3}$$

and in this case, $\mathbf{P}$ in Eq. 3–2 is approximately a diagonal matrix with the unknown signal powers $\{P_l\}_{l=1}^{L}$ on its diagonal. The problem of interest, then, is to estimate these L real-valued non-negative signal powers. When sources are partially correlated (or coherent), Eq. 3–3 is no longer valid. Deconvolution algorithms that can deal with correlated sources will be presented in Chapter 5, whereas the algorithms presented in this Chapter will be based on the assumption given in Eq. 3–3.

3.1 An Existing Deconvolution Approach

In this section, the inverse equation solved in DAMAS will be obtained from a slightly different perspective than the derivation in the original paper [18]. DAMAS uses the DAS beamformer results to obtain the deconvolved source strengths. Hence, substituting

Eq. 2–8 in Eq. 2–7, we obtain

$$\hat{P}_l^{(\mathrm{D})} = \frac{1}{M^2}\tilde{\mathbf{a}}_l^H \left(\frac{2}{\omega_0 B} \sum_{b=1}^{B} \mathbf{y}(b)\mathbf{y}^H(b) \right) \tilde{\mathbf{a}}_l, \tag{3–4}$$

and by substituting Eq. 2–4 in Eq. 3–4, we obtain

$$\hat{P}_l^{(\mathrm{D})} = \frac{1}{M^2}\tilde{\mathbf{a}}_l^H \left[\frac{2}{\omega_0 B} \sum_{b=1}^{B} (\mathbf{a}_1 s_1(b) + \ldots + \mathbf{a}_L s_L(b))(\mathbf{a}_1 s_1(b) + \ldots + \mathbf{a}_L s_L(b))^H + \sigma^2 \mathbf{I} \right] \tilde{\mathbf{a}}_l \tag{3–5}$$

for $l = 1, \ldots, L$, where the number of blocks is assumed to be sufficiently large such that the measurement noise covariance matrix is approximately equal to the ensemble average. The cross terms in Eq. 3–5 are negligible when the sources are uncorrelated (see Eq. 3–3). In DAMAS, Eq. 3–5 is approximated by also neglecting the measurement noise term $\sigma^2\mathbf{I}$ to obtain

$$\hat{P}_l^{(\mathrm{D})} = \frac{1}{M^2}\tilde{\mathbf{a}}_l^H \left[\sum_{l'=1}^{L} \frac{2}{\omega_0 B} \sum_{b=1}^{B} |s_{l'}(b)|^2 \mathbf{a}_{l'}\mathbf{a}_{l'}^H \right] \tilde{\mathbf{a}}_l = \sum_{l'=1}^{L} \tilde{A}_{l,l'} P_{l'}, \tag{3–6}$$

where $P_{l'} = \frac{2}{\omega_0 B}\sum_{b=1}^{B} |s_{l'}(b)|^2$ is the ensemble estimate for the signal power of source l and

$$\tilde{A}_{l,l'} = \frac{1}{M^2}|\tilde{\mathbf{a}}_l^H \mathbf{a}_{l'}|^2, \quad l, l' = l, \ldots, L. \tag{3–7}$$

Stacking up all $\hat{P}_l^{(\mathrm{D})}$, $l = 1, \ldots, L$, generates the following linear system of equations:

$$\underbrace{\begin{bmatrix} \hat{P}_1^{(\mathrm{D})} \\ \vdots \\ \hat{P}_L^{(\mathrm{D})} \end{bmatrix}}_{\hat{\mathbf{p}}^{(\mathrm{D})}} = \underbrace{\frac{1}{M^2}\begin{bmatrix} |\tilde{\mathbf{a}}_1^H \mathbf{a}_1|^2 & |\tilde{\mathbf{a}}_1^H \mathbf{a}_2|^2 & \ldots & |\tilde{\mathbf{a}}_1^H \mathbf{a}_L|^2 \\ \vdots & \vdots & \ddots & \vdots \\ |\tilde{\mathbf{a}}_L^H \mathbf{a}_1|^2 & |\tilde{\mathbf{a}}_L^H \mathbf{a}_2|^2 & \ldots & |\tilde{\mathbf{a}}_L^H \mathbf{a}_L|^2 \end{bmatrix}}_{\tilde{\mathbf{A}}} \underbrace{\begin{bmatrix} P_1 \\ \vdots \\ P_L \end{bmatrix}}_{\mathbf{p}}, \tag{3–8}$$

where $\hat{\mathbf{p}}^{(\mathrm{D})} \in \mathbb{R}^{L\times 1}$ and $\tilde{\mathbf{A}} \in \mathbb{R}^{L\times L}$ are known, $\tilde{A}_{l,l'}$, which was defined in Eq. 3–7, denotes the element in the lth row and $l'^{,\,\text{th}}$ column of $\tilde{\mathbf{A}}$, and the goal is to estimate $\mathbf{p} \in \mathbb{R}^{L\times 1}$, which consists of the unknown signal powers at each scanning point.

DAMAS estimates $\mathbf{p}$ iteratively using the Gauss-Seidel method [49] as follows:

$$\hat{P}_l^{(i)} = \frac{1}{\tilde{A}_{l,l}} \max\left(0, \hat{P}_l^{(\mathrm{D})} - \left[\sum_{l'=1}^{l-1} \tilde{A}_{l,l'} \hat{P}_{l'}^{(i)} + \sum_{l'=l+1}^{L} \tilde{A}_{l,l'} \hat{P}_{l'}^{(i-1)} \right] \right), \tag{3–9}$$

where i is the current iteration number limited above by a user defined maximum number of iterations, $\hat{P}_l^{(i)}$ is the DAMAS estimate of P_l at the ith iteration, $\hat{P}_l^{(0)} = 0$, $l = 1, \ldots, L$, and the non-negativity of each $\hat{P}_l^{(i)}$ is enforced since $\hat{P}_l$, $l = 1, \ldots, L$, represent power.

DAMAS requires many iterations, on the order of thousands, to show good performance, and hence DAMAS can become very time consuming depending on the scanning resolution, i.e., L. In addition, the Gauss-Seidel method is not guaranteed to converge unless $\tilde{\mathbf{A}}$ is diagonally dominant, i.e., for each row, the absolute value of the diagonal term is greater than the sum of absolute values of other terms which is usually not true [19]. Nevertheless, DAMAS has been successfully employed in many practical applications [18].

3.2 Diagonal Removal

Omitting the noise term in Eq. 3–6 can be justified by the use of the diagonal removal (DR) technique, which eliminates the white measurement noise that appears in the diagonal of $\hat{\mathbf{G}}$ by simply removing the diagonal elements, i.e., making them zero [2, 18]. In this case, the DAS output is calculated as

$$\hat{P}_l^{(\mathrm{D})} = \frac{1}{M^2 - M} \tilde{\mathbf{a}}_l^H \tilde{\mathbf{G}}^{\mathrm{DR}} \tilde{\mathbf{a}}_l, \tag{3–10}$$

where $\tilde{\mathbf{G}}^{\mathrm{DR}}$ is obtained by removing the diagonal elements of $\hat{\mathbf{G}}$. Then, Eq. 3–8 becomes $\hat{\mathbf{p}}^{(\mathrm{D})} = \tilde{\mathbf{A}}^{\mathrm{DR}} \mathbf{p}$ where,

$$\tilde{A}_{l,l'}^{\mathrm{DR}} = \frac{1}{M^2 - M} \tilde{\mathbf{a}}_l^H [\mathbf{a}_{l'} \mathbf{a}_{l'}^H]_{\mathrm{diag.}=0} \tilde{\mathbf{a}}_l, \quad l, l' = l, \ldots, L, \tag{3–11}$$

and $[\cdot]_{\mathrm{diag.}=0}$ means that the diagonal of the matrix argument is set to zero. In the rest of this chapter, DAMAS is applied with DR in all cases. Otherwise, the performance becomes worse as σ^2 increases. Consequently, we will denote $\tilde{A}_{l,l'}^{\mathrm{DR}}$ as $\tilde{A}_{l,l'}$ (and $\tilde{\mathbf{A}}^{\mathrm{DR}}$ as $\tilde{\mathbf{A}}$) in order to simplify the notation. It can be shown that DR does not affect the signal-of-interest term in the DAS output, but it has a slight effect on the interference term [2].

3.3 Sparsity Constrained Deconvolution

3.3.1 Sparsity Constrained Formulation

Assume that a measured vector $\bar{\mathbf{y}}$ exists which is known to satisfy the linear relation $\bar{\mathbf{y}} = \bar{\mathbf{A}}\bar{\mathbf{x}}$ where $\bar{\mathbf{A}}$ is known and $\bar{\mathbf{x}}$ is an unknown quantity that is to be estimated (see Eq. 3–8). In its simplest form, sparse modeling can be stated as follows:

$$\min \quad \|\bar{\mathbf{x}}\|_0 \quad \text{s.t.} \quad \bar{\mathbf{y}} = \bar{\mathbf{A}}\bar{\mathbf{x}}. \tag{3–12}$$

Usually, this problem is a combinatorial problem which becomes intractable quickly as the dimension of $\bar{\mathbf{x}}$ increases [25]. If the solution is sufficiently sparse, the ℓ_0-norm can be replaced with the ℓ_1-norm to make the problem convex [25]. The important point in Eq. 3–12 is that the matrix $\bar{\mathbf{A}}$ is usually ill-conditioned and not invertible. Otherwise, the solution could be obtained by taking the inverse, had $\bar{\mathbf{A}}$ been a square matrix, or by the least squares method otherwise.

Following the discussion above, the problem in Eq. 3–8 is directly applicable in the sparse signal representation context by observing that $\mathbf{p}$ is sparse since the number of scanning points is much larger than the actual number of sources present. Thus, we can immediately think of applying a slightly modified version of LASSO [26] to this problem,

$$\min_{\mathbf{p}} \quad \|\hat{\mathbf{p}}^{(\mathrm{D})} - \tilde{\mathbf{A}}\mathbf{p}\|_2^2 \quad \text{s.t.} \quad \sum_{l=1}^{L} |P_l| \leq \lambda, \quad P_l \geq 0, \quad l = 1, \ldots, L, \tag{3–13}$$

where the modification is to enforce every element of $\mathbf{p}$ to be non-negative. The following section describes a simple method for choosing the parameter λ automatically. Also, it is empirically observed that the method in Eq. 3–13 is not very sensitive to the selection of λ. In fact, if we let $\lambda \rightarrow \infty$, the formulation will reduce to a non-negative least squares problem. However, using prior knowledge about the sparsity of $\mathbf{p}$ will improve the estimate in most cases. The problem in Eq. 3–13 is a quadratic convex optimization problem which can be solved efficiently via readily available interior point methods [50, 51] to find the globally optimal solution for $\mathbf{p}$. Self-dual minimization (SeDuMi) [50] is an

extensively used public domain software package in the signal processing community for solving optimization problems over symmetric cones including linear, quadratic, second order conic and semi-definite programs. The detailed discussion of advanced optimization methods is beyond the scope of this dissertation and the interested reader is referred to a standard textbook on convex optimization [52].

3.3.2 Estimating the User Parameter

In the formulation Eq. 3–13, λ constrains the ℓ_1-norm of $\mathbf{p}$, i.e., the total power of the signals. Since this value is unknown, a way of determining λ has to be found for practicality. Without loss of generality, assume that each column of $\mathbf{A}$ has been normalized such that it has unit Euclidean norm [53]. Consider Eq. 3–2 again. The eigenvalue decomposition (EVD) of $\mathbf{APA}^H$ can be written as $\mathbf{APA}^H = \mathbf{U\Lambda U}^H$, where the columns of the unitary matrix $\mathbf{U}$ denote the eigenvectors of $\mathbf{APA}^H$ and the diagonal elements of the diagonal matrix $\mathbf{\Lambda}$ are the corresponding eigenvalues, denoted as $\lambda_1 \geq \lambda_2 \geq \ldots \geq \lambda_{L_0} \geq 0 = \ldots = 0$, where L_0 is the true number of sources. Note that $\mathbf{\Lambda} \in \mathbb{R}^{M\times M}$ where $M \gg L_0$. Then, $\mathbf{G}$ can be written as:

$$\mathbf{G} = \mathbf{U}\left(\mathbf{\Lambda} + \sigma^2\mathbf{I}\right)\mathbf{U}^H = \mathbf{U\Gamma U}^H, \tag{3–14}$$

where the diagonal elements of the diagonal matrix $\mathbf{\Gamma} \in \mathbb{R}^{M\times M}$ are $\gamma_1 \geq \gamma_2 \geq \ldots \geq \gamma_{L_0} \geq \sigma^2 = \ldots = \sigma^2$. Note that

$$\mathrm{tr}(\mathbf{\Lambda}) \;=\; \mathrm{tr}(\mathbf{U\Lambda U}^H) = \mathrm{tr}(\mathbf{APA}^H) = \mathrm{tr}(\mathbf{PA}^H\mathbf{A}) = \mathrm{tr}(\mathbf{P}) = \sum_{l=1}^{L} P_l, \tag{3–15}$$

which is the total power of the sources. Here, we have used the fact that the columns in $\mathbf{A}$ have unit norm and $\mathbf{P}$ is diagonal. (Note that we have also used the fact that $\mathrm{tr}(\mathbf{APA}^H) = \mathrm{tr}(\mathbf{A}^H\mathbf{AP}) = \mathrm{tr}(\mathbf{PA}^H\mathbf{A})$, which follows from the properties of the matrix trace operation [8].)

In practice, we only have the estimated covariance matrix given in Eq. 2–8 instead of the true covariance matrix $\mathbf{G}$. Let $\hat{\mathbf{G}} = \hat{\mathbf{U}}\hat{\mathbf{\Gamma}}\hat{\mathbf{U}}^H$ denote the EVD of $\hat{\mathbf{G}}$ with the eigenvalues

of $\hat{\mathbf{G}}$, i.e., the diagonal elements of $\hat{\mathbf{\Gamma}}$, arranged in non-increasing order. Then, we can determine the user parameter λ in Eq. 3–13 as:

$$\lambda = \mathrm{tr}(\hat{\mathbf{\Gamma}} - \hat{\gamma}_M \mathbf{I}), \tag{3–16}$$

where $\hat{\gamma}_M$ is the smallest diagonal element of $\hat{\mathbf{\Gamma}}$. We refer to the approach of solving Eq. 3–13 using the λ determined in Eq. 3–16 as the sparsity constrained DAMAS (SC-DAMAS). We will show using numerical examples that SC-DAMAS is computationally more efficient than DAMAS. Note that SC-DAMAS also uses DR in Eq. 3–13, whereas when estimating the user parameter, the full CSM (without removing the diagonal) is used, and the noise terms are removed as in Eq. 3–16 by using the smallest eigenvalue of $\hat{\mathbf{G}}$.

3.3.3 A More Efficient Implementation

The DAS estimate $\hat{\mathbf{p}}^{(\mathrm{D})}$ usually contains redundant information due to the wide 3-dB beamwidth of the DAS beamformer. Therefore, it is not always necessary to beamform at all L scanning points for deconvolution with SC-DAMAS. Beamforming at fewer points reduces the size of $\mathbf{p}$ and increases the speed of SC-DAMAS. In this case, Eq. 3–8 becomes,

$$\begin{bmatrix} \hat{P}_1^{(\mathrm{D})} \\ \vdots \\ \hat{P}_{L_0}^{(\mathrm{D})} \end{bmatrix} = \frac{1}{M^2} \begin{bmatrix} |\tilde{\mathbf{a}}_1^H \mathbf{a}_1|^2 & |\tilde{\mathbf{a}}_1^H \mathbf{a}_2|^2 & \dots & |\tilde{\mathbf{a}}_1^H \mathbf{a}_L|^2 \\ \vdots & \vdots & \ddots & \vdots \\ |\tilde{\mathbf{a}}_{L_0}^H \mathbf{a}_1|^2 & |\tilde{\mathbf{a}}_{L_0}^H \mathbf{a}_2|^2 & \dots & |\tilde{\mathbf{a}}_{L_0}^H \mathbf{a}_L|^2 \end{bmatrix} \begin{bmatrix} P_1 \\ \vdots \\ P_L \end{bmatrix}, \tag{3–17}$$

where $L_0 < L$. Note that $\tilde{\mathbf{A}}$ has now become a fat matrix, i.e., the number of its rows is smaller than the number of its columns. It will be shown in the numerical examples section that this approach can save a significant amount of computation time without degrading the performance. A similar approach cannot be used with DAMAS since DAMAS requires L equations to solve for the L unknowns in $\mathbf{p}$. Formulating the same problem as a sparse problem alleviates the need for L equations.

3.4 Covariance Matrix Fitting

Instead of using the sample covariance matrix to obtain the DAS estimates and then trying to deconvolve the results, we introduce a method for estimating source locations and strengths based directly on the CSM, i.e., $\hat{\mathbf{G}}$. Specifically, the covariance matrix fitting approach determines σ^2 and $\{P_l\}$ via,

$$\min_{\mathbf{P},\sigma^2} \quad \|\hat{\mathbf{G}} - \mathbf{APA}^H - \sigma^2\mathbf{I}\|_{\mathrm{F}}^2, \quad \text{s.t.} \quad \sum_{l=1}^{L} |P_l| \leq \lambda, \quad P_l \geq 0, \quad l = 1, \ldots, L, \tag{3–18}$$

which is a quadratic convex optimization problem where λ is defined in Eq. 3–16 and $\mathbf{P}$ is a diagonal matrix with $\{P_l\}_{l=1}^{L}$ on its diagonal.

The idea behind CMF is quite intuitive in the sense that it basically tries to fit the unknown signal powers and the noise power to the model in Eq. 3–2 such that the solution is sparse. In contrast to deleting the diagonals of $\hat{\mathbf{G}}$, CMF tries to extract the noise and use the signal components in the diagonal. Moreover, this formulation does not require the implementation of the DAS beamformer as an initial step and it converges quickly thanks to the convex formulation. Similar to SC-DAMAS, CMF is quite insensitive to λ.

Figure 3-1 shows a pictorial representation of Eq. 3–8, and DAS, DAMAS, SC-DAMAS and CMF. As mentioned previously, DAMAS and SC-DAMAS deconvolve the true signal powers from the DAS results, whereas CMF deconvolves the signal powers using the CSM directly. Note that the deconvolution approaches will estimate the signal powers at the source locations. Therefore, in order to match the array output levels to what a single microphone would measure at the array center, P_l should be divided by $r_{l,0}^2$ for $l = 1, \ldots, L$ after being estimated with DAMAS, SC-DAMAS and CMF.

3.5 Numerical Examples

In this section, we evaluate the performance of DAMAS, SC-DAMAS and CMF using SADA (see Figure 1-1(a)) [1, 3]. We assume that SADA is at a distance of 1.50 m from the region of interest similar to the DAMAS paper [17, 18]. The scanning region extends from -25.40 cm to 25.40 cm in both the x- and y-axes and the resolution in both directions

is 2.54 cm. We simulate the received signal at each microphone according to Eq. 2–4. The noise components $\{\mathbf{e}(n)\}$ in Eq. 2–4 are assumed to be uncorrelated with the source signals and distributed as circularly symmetric independent and identically distributed (i.i.d.) complex Gaussian random variables with zero-mean values and variance σ^2 [8]. The signal waveforms are also distributed as circularly symmetric i.i.d. complex Gaussian random variables with zero-mean values and a certain power level which is assumed to be 25 dB. This value is chosen without loss of generality since σ^2 will be varied throughout the experiments.

There are three parameters which affect the performances of the algorithms directly: number of FFT blocks B, noise variance σ^2, and frequency of interest f. The incoherence assumption breaks down as the number of FFT blocks decreases since the cross terms in Eq. 3–5 become significant and also the additional noise term in Eq. 3–5 is no longer $\sigma^2\mathbf{I}$ but a non-diagonal matrix. Noise affects all the algorithms negatively as in all applications. Finally, the frequency determines the resolution of the algorithms since as the frequency increases, the difference in the steering vectors for nearby sources increases and hence it is easier for the algorithms to discriminate them.

We start our simulations with a relatively easy scenario where the number of FFT blocks is large ($B = 10,000$) and $\sigma^2 = 0$, in which case the assumptions of the algorithms are almost correct. The resulting beamforming maps are shown in Figures 3-2 A and B, where the horizontal axis and the vertical axis represent the 2-D scanning plane and the power levels are represented in a gray color scale over a span of 10 dB. As expected, DAS merges the peaks as if there were a single source. CMF works quite well and SC-DAMAS and DAMAS show good performance when the frequency is high. Next, the noise variance σ^2 is increased to 100. As shown in Figure 3-2 C, CMF is more robust to noise than DAMAS and SC-DAMAS. Note that for all the examples in this section, DAMAS has been run for 10,000 iterations after which no significant improvement was observed.

Next, we decrease the number of FFT blocks to 500 and increase the frequency to 20 kHz to resolve a more complicated source distribution. The results are shown in Figure 3-3 for $\sigma^2 = 0$ and 5. The location estimates of SC-DAMAS for some of the sources are inaccurate and DAMAS is not able to discriminate the sources. CMF, however, is able to recover the sources reasonably well in both cases. If the frequency is decreased to $f = 5$ kHz, DAMAS performance degrades significantly as also observed in other studies [22]. Figure 3-4 shows the beamforming maps for $\sigma^2 = 0$ and 4 with $B = 500$. DAMAS is not able to recover the source location for $f = 5$ kHz even after $50,000$ iterations. We again observe offsets in the location estimates of SC-DAMAS and when the noise is increased, the results become worse. This is due to the fact that SC-DAMAS is solving the same DAMAS inverse problem. In Figure 3-4 A, the highest outlier for CMF is 5 dB below the actual signal levels and in Figure 3-4 B, CMF provides the best performance. This performance gain can be attributed to the different formulation of CMF than DAMAS and SC-DAMAS. Recall that CMF does not rely on the DAS beamformer estimates and does not delete the diagonals. Note that the source distribtution considered for the last case is simpler than the other two since the frequency is low.

A qualitative assessment of the algorithms is given in Table 3-1. The computational complexity of DAMAS was higher than that of SC-DAMAS and CMF in our simulations. Note that the public domain solver [50] we use for finding the optimal solutions to the SC-DAMAS and CMF problems works up to $L = 1,000$ scanning points when the signals are complex-valued. However, a commercial software designed for this purpose can go up to many more variables and hence the formulations are applicable to higher resolutions if desired. Table 3-2 shows the computation times of each algorithm for the examples considered in this section. We observe that SC-DAMAS is the fastest and CMF takes almost thrice the time of SC-DAMAS. DAMAS takes almost twice the time of CMF and eight times the time of SC-DAMAS. Furthermore, as mentioned in Section 3.3.3, the sparse formulation of SC-DAMAS allows us to reduce the size of $\hat{\mathbf{p}}^{(\mathrm{D})}$ in Eq. 3–8 and this

in turn provides more improvements in speed. In Table 3-3, we noted the computation time of SC-DAMAS for different values of L_0 for the example considered in Figure 3-2 B. In Figure 3-5, the performance of SC-DAMAS using four different L_0 values is shown for the example considered in Figure 3-2 B (note that in this figure, 1D representations of the images are shown where the horizontal axis represents the grid points and the vertical axis represents the power estimated at each grid point). It is observed that the performance of SC-DAMAS undergoes only a minor degradation when $L_0 > 36$. Below that, the algorithm does not provide accurate results. The savings are huge and the problem can be solved in almost 1 second when $L_0 = 36$ which should be compared with 167 seconds for DAMAS and 62 seconds for CMF keeping in mind that CMF provides better results than SC-DAMAS and SC-DAMAS provides better results than DAMAS. In any case, SC-DAMAS offers a fast way of solving Eq. 3–8.

3.6 Conclusions

In this chapter, sparsity contrained convex optimization methods, namely SC-DAMAS and CMF, for the deconvolution of uncorrelated sources have been presented. SC-DAMAS is an extension of DAMAS and tries to solve the same basic equation by exploiting sparsity. Similarly to DAMAS, SC-DAMAS employs DR to mitigate the effects of noise, whereas the CMF algorithm eliminates noise without deleting the diagonals of the CSM completely. Also, DAMAS and SC-DAMAS algorithms require the implementation of DAS and implicitly depend on the performance of this method. On the other hand, CMF is independent of DAS. It was shown with simulations that CMF shows better performance than DAS, DAMAS and SC-DAMAS and SC-DAMAS shows better results than DAMAS. An alternative implementation of SC-DAMAS was provided which offers a fast algorithm as compared to DAMAS and CMF.

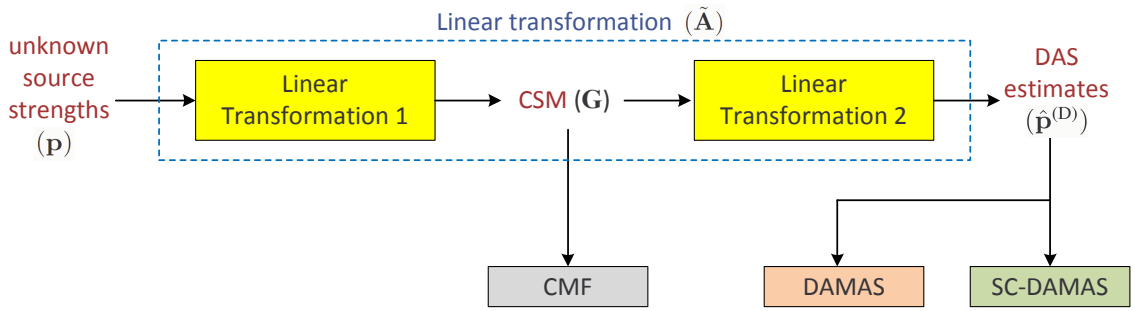

Figure 3-1. Methodology of DAS, DAMAS, SC-DAMAS and CMF.

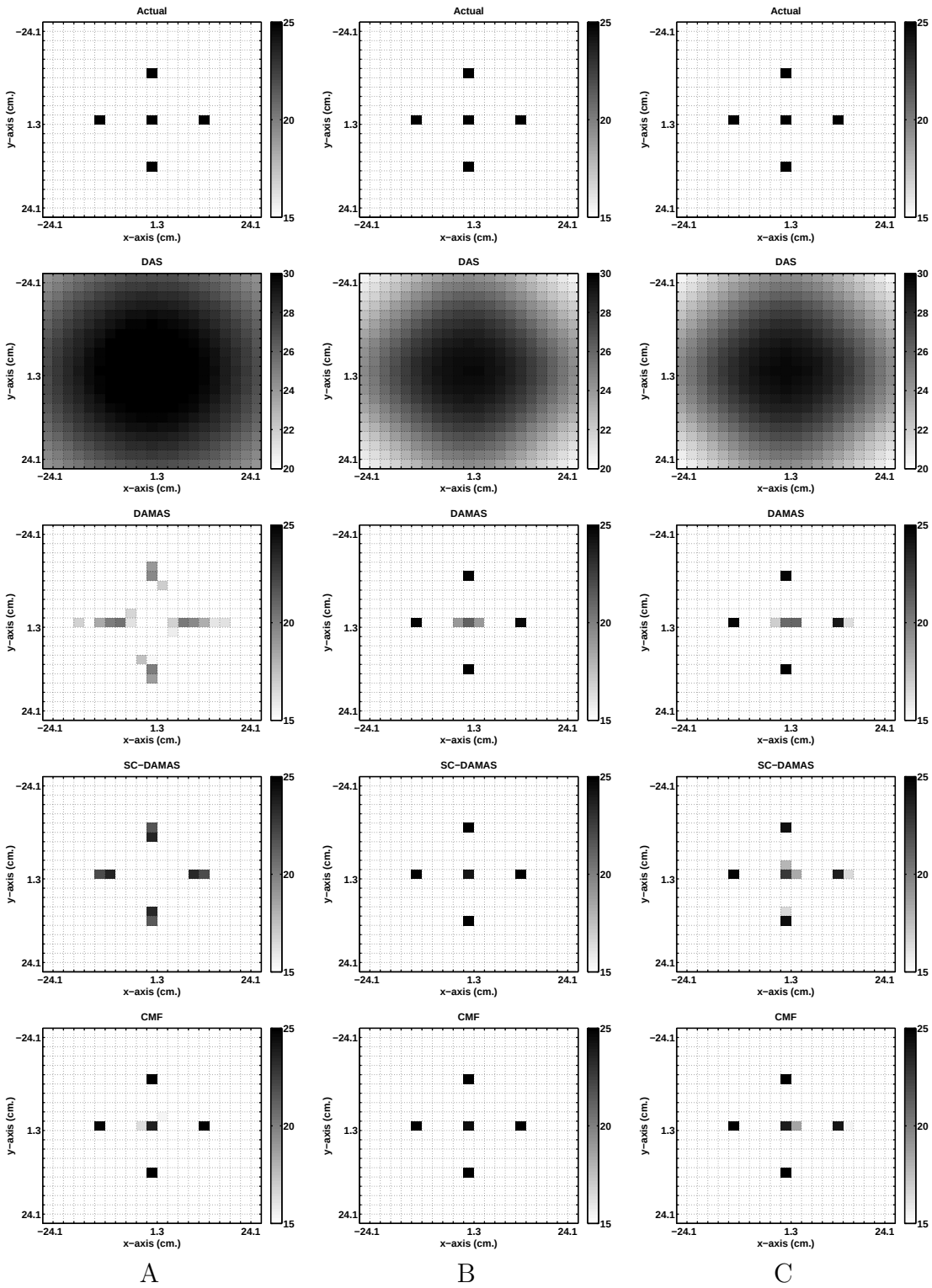

Figure 3-2. The beamforming maps of the actual sources, DAS, DAMAS, SC-DAMAS and CMF with three different settings as follows: $B = 10,000$, A) $f = 10$ kHz and $\sigma^2 = 0$, B) $f = 15$ kHz and $\sigma^2 = 0$, and C) $f = 15$ kHz and $\sigma^2 = 100$. The 2-D plots represent the scanning region and the power levels are in dB.

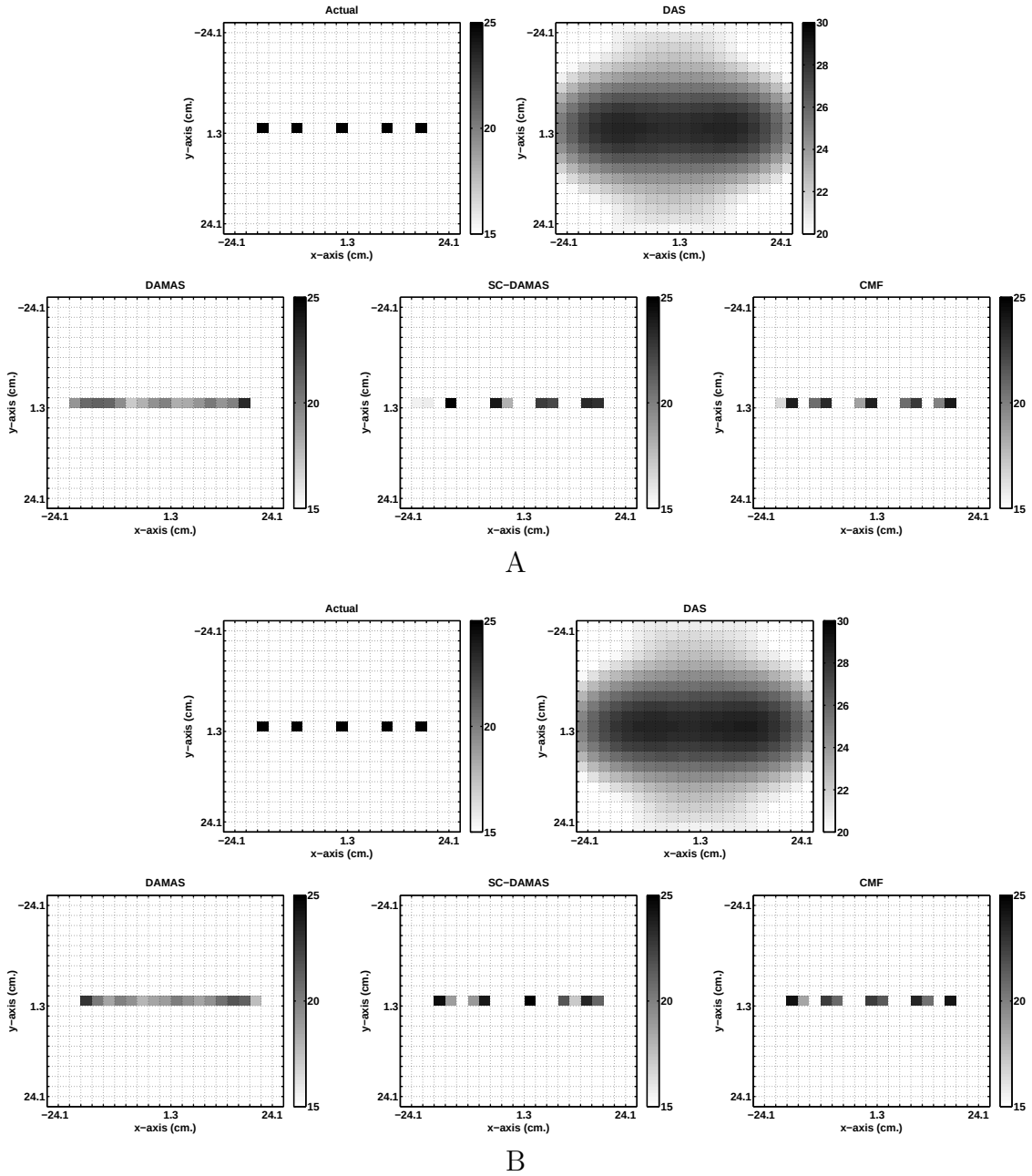

Figure 3-3. The beamforming maps of the actual sources, DAS, DAMAS, SC-DAMAS and CMF with $f = 20$ kHz and $B = 500$. A) $\sigma^2 = 0$. B) $\sigma^2 = 5$. The 2-D plots represent the scanning region and the power levels are in dB.

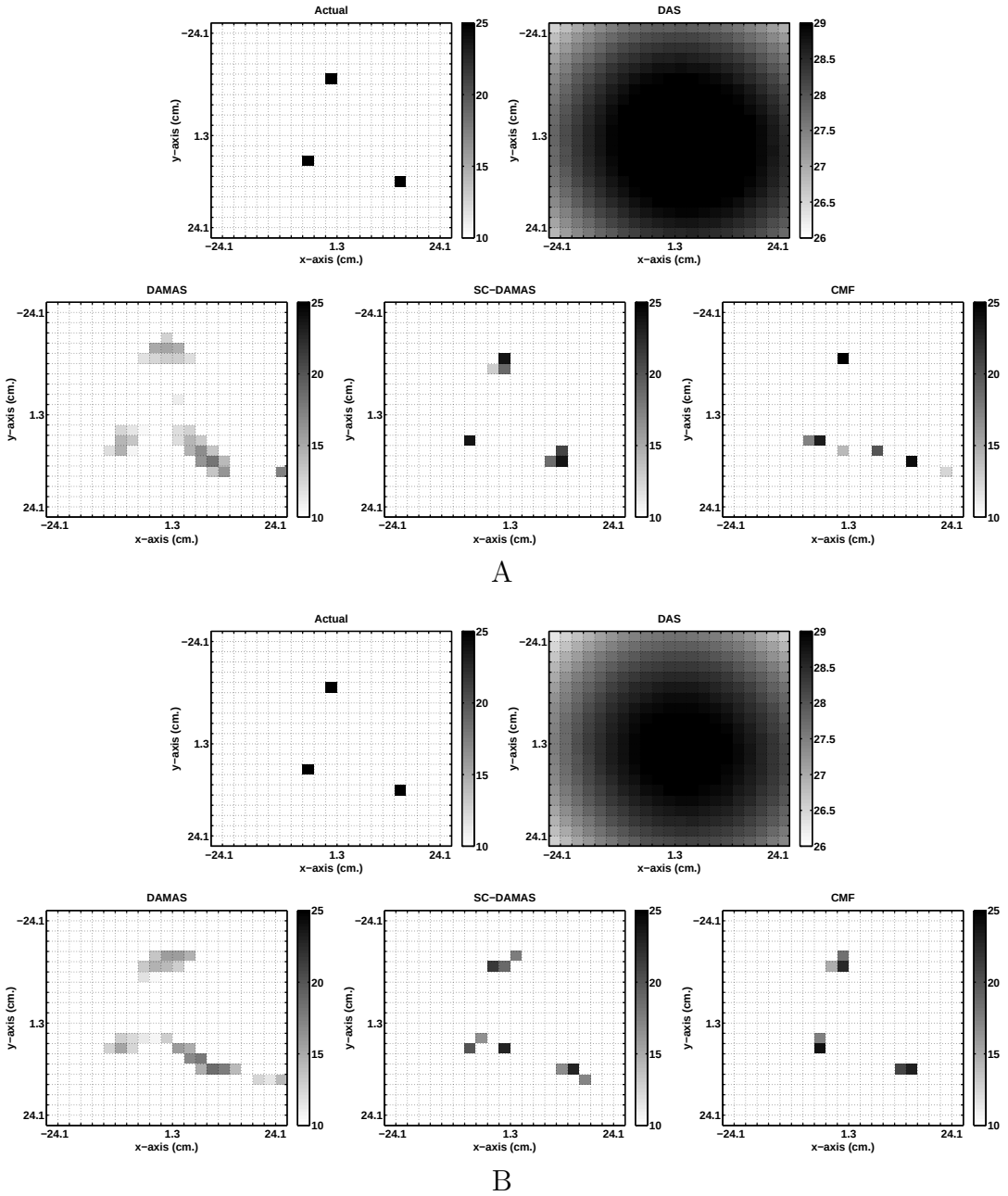

Figure 3-4. The beamforming maps of the actual sources, DAS, DAMAS, SC-DAMAS and CMF with $f = 5$ kHz and $B = 500$. A) $\sigma^2 = 0$. B) $\sigma^2 = 4$. The 2-D plots represent the scanning region and the power levels are in dB.

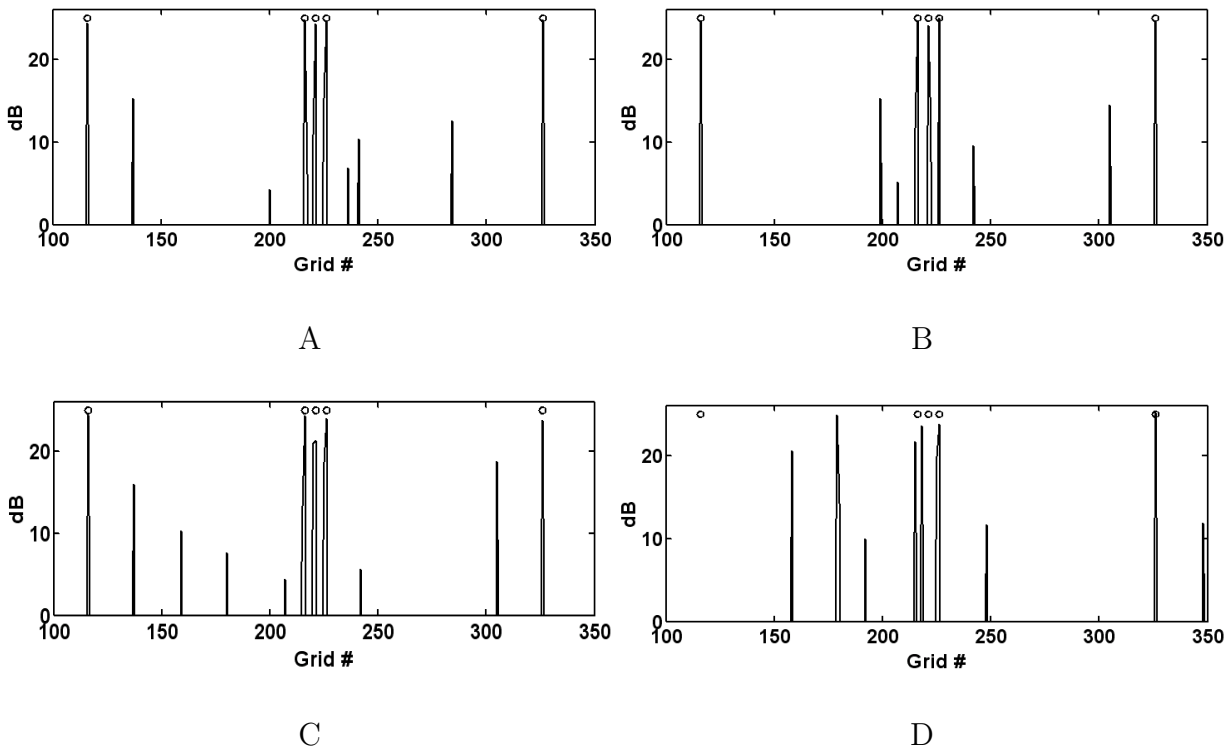

Figure 3-5. Performance of SC-DAMAS when L_0 is varied for the example considered in Figure 3-2 B. A) $L_0 = 441$. B) $L_0 = 121$. C) $L_0 = 36$. D) $L_0 = 16$. Note that $L = 441$. In each plot, the horizontal axis represents the grid points and the vertical axis represents the power estimated at each grid point. The circles indicate the true source locations and powers.

Table 3-1. Characteristics of the acoustic imaging algorithms.

	DAS	DAMAS	SC-DAMAS	CMF
Resolution	Low	Medium	High	High
Sensitivity to noise	Low	Medium	Medium	Low
Computation time	Low	High	Medium	Medium
Max. number of variables	High	Medium	Low	Low

Table 3-2. Computation times of DAMAS, SC-DAMAS and CMF in seconds on personal computer, 2.0 GHz dual core processor, 2 GB of RAM.

	Fig. 1			Fig. 2		Fig. 3	
	(a)	(b)	(c)	(a)	(b)	(a)	(b)
DAMAS	160	165	161	160	160	180	162
SC-DAMAS	24	24	24	23	24	21	22
CMF	66	65	71	69	65	75	73

Table 3-3. Speeding up of SC-DAMAS for the example of Figure 3-2(b). Timing values are in seconds.

L_0	441	196	121	81	36
Time	24.0	12.7	4.2	2.8	1.3

CHAPTER 4
EXPERIMENTAL RESULTS

The purpose of this chapter[1] is to provide a comparison of DAS, DAMAS, SC-DAMAS, CMF and CLEAN-SC using experiments consisting of a single source, two uncorrelated sources with similar and different powers and two coherent sources. The experimental data was acquired at the UFAFF using LAMDA. The source localization capability of the algorithms as well as their accuracy in estimating the absolute signal powers will be analyzed. The absolute signal powers estimated by the beamforming algorithms will be compared with those measured by a reference microphone placed at the center of the microphone array.

4.1 Microphone Array

LAMDA is a zero redundancy spiral aperture array built on a 1.82 m diameter rigid aluminum plate, that consists of 90 flush-mounted Panasonic WM-61A microphones, and it has been used in all the experiments in this chapter. LAMDA was designed by the procedures described by Underbrink [5, 6] and was fabricated for use at the UFAFF [47]. LAMDA contains two nested spiral arrays: *i)* a small aperture inner array consisting of 45 microphones and *ii)* a larger aperture outer array consisting of 63 microphones. We consider only the outer array, which is shown in Figure 4-1 A (note that this is the same plot shown in Figure 1-1 B but with a reference microphone placed at the center), in this dissertation due to its higher resolution at lower frequencies of operation (we refer to the outer LAMDA array simply as LAMDA). Figure 4-1 B shows the 3-dB beamwidth of the array versus frequency at a beamforming distance of 1.48 m from the array plate. A 0.03 m diameter Bruel and Kjaer (B&K) microphone is placed at the center of the array and referred to as the reference microphone throughout this chapter. The reference microphone

[1] The author would like to thank to Nikolas Zawodny, Christopher Bahr, Dr. Fei Liu, Alberto Gordon, Tom Kennedy and Adam Edstrand of the University of Florida for their assistance on wind tunnel testing.

is calibrated using a pistonphone at 1 kHz. The array output levels will be compared with the levels measured by this reference microphone. The reference microphone is also used in the second step of array calibration.

4.2 Experimental Setup

The data analyzed in this chapter was acquired by using a 68-channel National Instruments PXI-1045 chassis with 17 NI PXI-4462 data acquisition (DAQ) cards. Each channel has 24-bit resolution with 118 dB dynamic range. All measurements were ac coupled with a -3 dB cut-on at 3.4 Hz, and appropriate anti-aliasing filters were applied. Unless specified otherwise, the following set of parameters were used for data analysis and reduction. The sampling frequency used in the measurements was 65,536 Hz and the block length was set to 4096 samples, resulting in a 16 Hz narrowband bin width. The data acquisition time was 15 seconds. Hanning windows with 75% overlap were applied to each block of data before taking the FFTs. The resulting number of blocks was 957 (498 effective blocks [54]).

The acoustic sources used in the experiments were custom built using JBL type 2426H speakers. An aluminium tube of diameter 0.03 m and length 0.52 m was attached at the output of each JBL speaker to facilitate plane wave propagation and eliminate higher order modes, and acoustic foam was used to mitigate reflections as shown in Figure 4-2 A. The measurements were conducted without flow. Two sets of experiments were conducted; one with a single source and one with two sources as shown in Figures 4-2 B and C, respectively. In the latter set of experiments, the signal powers and the coherence between the sources have been varied. Figure 4-3 shows pictures of the two speakers and LAMDA during testing.

Unless otherwise specified, the beamforming scanning regions are set from -0.3 m to 0.3 m with a resolution of 0.03 m in both the x and y directions for the single source experiments, and from -0.4 m to 0.2 m in the x direction and from -0.3 m to 0.3 m

in the y direction with a resolution of 0.025 m in both the x and y directions for the experiments containing two sources.

4.3 Software

Custom software has been written in MATLAB[2] and LabVIEW[3] for data acquisition and analysis. The data were acquired using LabVIEW and the time series of each microphone was stored in binary format. MATLAB was used for the reduction and post-processing of the time data.

Figure 4-4 and Figure 4-5 show snapshots from the data analysis software which has been coded in MATLAB. The first graphical user interface (GUI), shown in Figure 4-4, is used to compute the CSMs from the raw microphone measurements in time. This program outputs the frequency-dependent CSMs and an information file containing the parameters used for computing the CSMs. The second GUI, which is shown in Figure 4-5, is used to beamform using the CSMs and the information file produced by the first user interface. The beamforming GUI allows the user to enter the center frequency of interest, height of the beamforming plane and the resolution, and it can be used to implement DAS, DAMAS, SC-DAMAS, CMF and CLEAN-SC as well as some other algorithms which are in the development phase. A different scanning resolution can be used for the basic algorithms such as DAS and the more advanced ones such as DAMAS, SC-DAMAS and CMF. Other options offered by the beamforming GUI are the array calibration procedure described in Section 2.3, the shear layer correction (SLC) procedure described in [1, 55] and DR (see Section 3.2). The beamforming results can be obtained in narrow-band, $1/3^{\text{rd}}$ or $1/12^{\text{th}}$ octave bands using the procedure described in [20], i.e., by summing up the CMSs at each narrow-band frequency in a given octave band and then beamforming only once using the steering vectors corresponding to the center frequency.

[2] MATLAB is a registered trademark of The MathWorks.

[3] LabVIEW is a registered trademark of National Instruments.

4.4 Absolute Levels

The absolute signal powers are estimated using the integration method with DAS, DAMAS, SC-DAMAS, and CMF, whereas CLEAN-SC uses the clean spectrum it constructs to estimate the signal powers. With DAS, the integrated SPL is computed by summing the DAS power estimates inside the integration region (which is within the scanning region) and normalizing the result by a scaling factor obtained by summing the psf values over the same integration region. Stated mathematically, the integrated DAS level is defined as $\sum_{l\in\mathcal{L}} P_l / \sum_{l\in\mathcal{L}} \mathrm{psf}(l)$, where $\mathcal{L}$ is a set containing the indices of the scanning grid points within the integration region [3, 56] and psf was defined in Section 2.2. With DAMAS, SC-DAMAS and CMF, there is no need for the normalization since the array response is already eliminated from the results and only summing the estimated power levels within the integration region suffices. CLEAN-SC uses the average of the diagonal of the clean cross spectral matrix that it constructs by considering only the contributions from sources within the integration region [57].

4.5 Array Calibration Performance

Consider a calibration setup with a single speaker placed at $(x, y, z) = (0, 0, 1.48)$ m, where the array center is at $(x, y, z) = (0, 0, 0)$ m and the array plate extends in the xy-plane. The integrated DAS levels are shown in Figure 4-6 A alongside with the reference microphone levels when array calibration is not applied and the nominal sensitivities (30 mV/Pa as used at the UFAFF) of the microphones are used for beamforming. The integration region is a square centered at $(x, y) = (0, 0)$ m and each side of the square is 0.4 m long. It is observed that there are differences, as large as 5 dB, between the array estimated levels and the reference microphone levels. On the other hand, when array calibration is applied, the DAS integrated levels match the reference microphone levels as shown in Figure 4-6 B. This simple example shows that array calibration is essential for matching the array output levels to the reference microphone levels. Calibration procedure was also shown to be necessary for reducing the

uncertainties in the beamforming levels when errors are expected in microphone locations and/or temperature [58]. Therefore, in the results presented below, array calibration is always applied.

4.6 Single Source

Consider the experimental setup shown in Figure 4-2 B with a single speaker generating broadband noise at a distance of 1.48 m from the array. Figure 4-7 shows the beamforming plots obtained with DAS, DAMAS, SC-DAMAS, CMF and CLEAN-SC together with the array psf at 2 kHz. The integration region is indicated with the solid rectangle and the integrated (Int.) and maximum (Max.) levels are noted in the upper right corner of each plot. The true source location is indicated by the cross. We observe that all the algorithms recover the source location successfully and also indicate consistent integrated levels with each other. In Figure 4-8 we plot the integrated SPLs obtained with all the beamforming algorithms over a frequency range of 0.5 kHz to 12 kHz with both simulated and experimental data. In the simulations, circularly symmetric i.i.d. complex Gaussian random variables are used to generate the signal and measurement noise waveforms which are then used to obtain the synthetic microphone measurements using Eq. 2–2 and Eq. 2–3. The simulated signal power is set to 50 dB and 458 effective blocks are used similar to the experimental scenario. The measurement noise power is set to 30 dB. We observe that the integrated SPLs of all the algorithms are in good agreement with the reference microphone SPLs with both simulated and acquired data.

4.7 Two Uncorrelated Sources

Consider the experimental setup shown in Figure 4-2 C with two speakers generating uncorrelated broadband noise. Uncorrelated broadband noise is generated by feeding the two speakers with independent white noise signals from two different outputs of a function generator. We consider two scenarios; in the first case, the two speakers generate signals of similar powers and in the second case, the second speaker generates a weaker signal than the first one. In Figure 4-9 the reference microphone levels when *i)* only speaker 1

is on, *ii)* only speaker 2 is on, *iii)* both speakers are on and *iv)* the computed sum from *i)* and *ii)* are plotted. The noise floor of the reference microphone is also shown in Figure 4-9. Figure 4-9 A and B are for the cases when the speakers generate signals of similar and different powers, respectively. From Figure 4-9 A, we observe that the powers of the two sources are very similar; the average signal power over the entire frequency range is 47.7 dB for speaker 1, 47.6 dB for speaker 2 and 50.8 dB for both speakers (computed sum is 50.9 dB). From Figure 4-9 B, on the other hand, we observe that source 2 has lower power than source 1 at most of the frequencies; the average signal power over the entire frequency range is 49.0 dB for speaker 1, 43.8 dB for speaker 2 and 50.3 dB for both speakers (computed sum is 50.4 dB). From Figure 4-9, we also observe that the computed sum matches the measured levels, especially for frequencies above approximately 800 Hz. This shows that the sources are indeed uncorrelated for those frequencies.

In Figures 4-10 and 4-11, the beamforming maps obtained with equal and different signal powers, respectively, are shown at a frequency of 2 kHz. It is observed that DAS is unable to distinguish the two sources in both of the cases, whereas DAMAS, SC-DAMAS and CMF can distinguish the two sources successfully. The estimated power levels for the two sources are similar in Figure 4-10 and the estimated power level for the second source is lower than that of the first one in Figure 4-11 with DAMAS, SC-DAMAS and CMF. CLEAN-SC, on the other hand, identifies the location of the second source inaccurately (it was observed in results not shown here that at higher frequencies, CLEAN-SC was able to recover the locations of both of the sources accurately). The integrated levels obtained with the beamforming algorithms are shown in Figure 4-12. It is observed that all the algorithms yield very similar integrated levels with each other and the reference microphone. We observe that although CLEAN-SC is unable to recover the second source location very accurately, its integrated level estimates line up with those of the other algorithms.

Next, we consider the ability of the advanced algorithms in estimating the signal powers of the two speakers individually. For this purpose, the integration region for estimating the signal power of the first source (Reg. 1) and the integration region for estimating the signal power of the second source (Reg. 2) are defined as shown in Figure 4-13. In Figure 4-14 A we show the integrated levels (computed using Reg. 1) obtained with DAS and SC-DAMAS when only speaker 1 is on and when both of the speakers are on. Similarly, in Figure 4-14 B we show the integrated levels (computed using Reg. 2) when only speaker 2 is on and when both of the speakers are on. We also show the reference microphone levels obtained when either one of the speakers is on in these two figures. From Figure 4-14 A it is observed that SC-DAMAS levels obtained when only one of the speakers is on is consistent with the levels obtained when both of the speakers are on and the integration region covers only the source of interest. On the other hand, for DAS, due to low resolution, these levels do not coincide well for frequencies lower than about 2 kHz. From Figure 4-14 B, we observe that DAS performance is even worse when estimating the power of the second (the weaker) source since the sidelobes from the stronger source are causing the DAS estimates to be larger than the true signal power. It is also observed that the array levels match the reference microphone levels better in Figure 4-14 A (with the stronger source) than in Figure 4-14 B (with the weaker source). The results with DAMAS and CMF are similar to those obtained with SC-DAMAS, whereas the CLEAN-SC result (shown in Figure 4-15) is slightly worse than DAMAS, SC-DAMAS and CMF but better than DAS.

4.8 Two Coherent Sources

Consider the experimental setup shown in Figure 4-2 C again with two speakers but now generating coherent broadband noise. Coherent broadband noise is generated by feeding the two speakers with a single white noise waveform (this is done by using a T connection at the output of the function generator). Figures 4-16 A and B show the SPLs measured by the reference microphone and the LAMDA microphones when the two

sources are uncorrelated with similar powers (the same example considered in Figures 4-9 A and 4-10) and when the two sources are coherent, respectively. We observe that the sound spectra of the LAMDA microphones become very different at frequencies above 2 kHz in the latter case. A discussion on this issue is presented below.

All of the aforementioned beamforming algorithms are based on the assumption that the sources are uncorrelated. In Figure 4-17 we show the beamforming maps obtained with two coherent sources at 2 kHz. As expected, the algorithms fail to distinguish the two sources. DAS and CLEAN-SC point a single source approximately in the middle of the true source locations. Although DAMAS, SC-DAMAS and CMF identify two sources, the locations are inaccurate. In Figure 4-18 we show the beamforming maps at 4 kHz for the coherent sources case. It is observed that all the beamforming algorithms except CLEAN-SC can now identify the sources relatively more accurately. Since CLEAN-SC is based on removing the correlated source components with the peaks in the beamforming map, it only identifies one of the coherent sources regardless of the frequency and treats the other coherent sources as the sidelobes due to the identified source.

In Figure 4-19 the integrated levels are shown using both simulated and experimental data with coherent sources. In the simulations, the signals originating from the two speakers are generated as identical waveforms and the signal power of each source is set to 50 dB. We observe that all the beamforming algorithms still yield consistent results with each other but different from the reference microphone, especially above 5 kHz. In fact, the reference microphone level decreases with frequency (with both simulations and experiments), whereas the array estimates do not.

To understand this phenomenon, consider the measurement of the mth microphone, modeled as (see Eq. 2–2 and Eq. 2–3)

$$y_m(b) = \exp(-jkr_{1,m})/r_{1,m}s_1(b) + \exp(-jkr_{2,m})/r_{2,m}s_2(b), \quad b = 1, \ldots, B, \tag{4–1}$$

in the presence of only two sources and no contaminating noise. When the two speaker waveforms are identical, i.e., when $s_1(b) = s_2(b)$ for $b = 1, \ldots, B$ (the two waveforms might differ in practice due to disparities in wiring, speakers and so on), then

$$\begin{aligned} y_m(b) &= (\exp(-jkr_{1,m})/r_{1,m} + \exp(-jkr_{2,m})/r_{2,m})\, s_1(b) \\ &= (\exp(-jkr_{1,m})/r_{1,m} + \exp(-jkr_{2,m})/r_{2,m})\, s_2(b). \end{aligned} \tag{4–2}$$

In Figure 4-20 A, the autospectra of all the LAMDA microphones and the reference microphone, i.e., $\frac{1}{B}\sum_{b=1}^{B} |y_m(b)|^2$ for $m = 0, \ldots, M$, where $m = 0$ corresponds to the reference microphone, is plotted. In this figure, $s_1(b)$, $b = 1, \ldots, B$, (which is equal to $s_2(b)$) are simulated as i.i.d. Gaussian random variables with zero mean and unit variance for $B = 498$. Note that $\frac{1}{B}\sum_{b=1}^{B} |s_1(b)|^2$ (and $\frac{1}{B}\sum_{b=1}^{B} |s_2(b)|^2$) is normalized so that the signal power is 50 dB. It is observed that due to the coherence of the sources, each microphone observes significant cancellation at different frequencies. The reason why the array levels do not decrease as fast as the reference microphone level in Figure 4-19 is because there is always a set of microphones in the array which do not encounter severe cancellation and these microphones help keep the array output estimate larger than the reference microphone level.

In Figure 4-20 B, the simulated and measured autospectrum of a single LAMDA microphone located at $(x, y, z) = (-0.56, 0.02, 0)$ m is shown together with the microphone noise floor. It is observed that the experimental data matches the simulated pattern, especially for frequencies above 2 kHz. This serves as a justification that the interference pattern observed at the array microphones is in fact due to the coherence of the sources. When the two sources are uncorrelated, the autospectrum of $y_m(b)$ (see Eq. 4–1) does not contain the cross term between the two sources and hence the exponential terms do not have an effect on the outcome (since they will be cancelled out after being magnitude squared), whereas when the sources are highly correlated, the exponential terms come into

play. In fact, all the curves in Figure 4-20 A become straight lines at the same level when the sources are uncorrelated (results not shown for brevity).

Coherent sources violate the fundamental incoherence assumption of the beamforming algorithms. Approaches that can deal with coherent sources will be presented in the next chapter.

4.9 Computational Complexity

We now elaborate on the computational complexities of the beamforming algorithms with the scanning resolutions used in this chapter. Table 4-1 shows the computation times required by each algorithm for the two scanning region settings used in the analysis presented above. We observe that DAS and CLEAN-SC are the fastest algorithms followed by SC-DAMAS, CMF and DAMAS (5000 iterations have been employed with DAMAS). Note that although CLEAN-SC is faster than the other advanced algorithms, its performance depends on the selection of four user parameters (significant degradations in performance might be encountered when these parameters are not selected properly).

One advantage of SC-DAMAS over DAMAS and CMF is that while solving Eq. 3–8, $\hat{\mathbf{p}}^{(\mathrm{D})}$ can be evaluated at fewer points than L while still being able to estimate the power at all the L grid points as described in Section 3.3.3. A rule of thumb is to select the scanning grid resolution to be at most half the 3-dB beamwidth of the array at a given frequency. The results obtained using the fast version of SC-DAMAS for the single source ($L_0/L = 0.38$) and two uncorrelated sources ($L_0/L = 0.27$) with similar powers case are shown in Figure 4-21 (compare with the SC-DAMAS images in Figures 4-7 and 4-10). Note that the performance of SC-DAMAS did not degrade significantly compared to using all the L grid points when evaluating DAS. The computation time required by SC-DAMAS by setting the resolution to 0.05 m (which is approximately $1/5^{\mathrm{th}}$ the 3-dB beamwidth of the array at 2 kHz) is also given in Table 4-1.

4.10 An Example with an Airfoil Model

As a final case, we analyze the performance of the beamforming algorithms with the NACA 63-215 Mod B airfoil [47, 59]. The schematic of the test setup is give in Figure 4-22 and a picture of the airfoil is shown in Figure 4-23. (The details of this aeroacoustic experiment are given by Bahr et al. [47] and hence omitted here for brevity.) Note that in these experiments, the reference microphone at the array center was not present. The beamforming images of the airfoil at 2.6 kHz is shown in Figure 4-24, where two locations with dominant noise can be identified on the trailing edge (T.E.) which is located at $x = 0$ m. The leading edge is located at $x = 0.74$ m and not shown in the beamforming image since the T.E. is the dominant noise source. Note that in the beamforming map, the scanning region extends from -0.5 m to 0.5 m in the x direction and from -0.6 m to 0.6 m in the y direction with a common resolution of 0.04 m, and the model is at a broadband distance of 1.30 m with respect to the array plane. The Mach number is 0.17. Due to the presence of flow during the airfoil testing, DR is applied (see Section 3.2). Moreover, SLC has also been employed [1, 55]. The data acquisition time was 5 seconds, sampling frequency was 65,536 Hz and the block length was 2048 samples (frequency resolution of 32 Hz). A Hanning window with 75% overlap has been employed leading to 331 effective averages [47]. We observe that the estimated noise sources are well aligned with the T.E. of the airfoil. The deconvolution algorithms indicate dominant sources at consistent locations and the integrated levels of these algorithms are in good agreement. Note that the integration region is from -0.2 to 0.2 m in the x-axis and from -0.5 to 0.5 m in the y-axis as shown in the plots.

4.11 Conclusions

In this chapter we compared the performance of DAS, DAMAS, SC-DAMAS, CMF and CLEAN-SC using experimental data consisting of several test cases including a setup with a single source, another setup with two uncorrelated sources of similar and different powers and a setup with two coherent sources. From the results presented above, it was

observed that DAMAS, SC-DAMAS and CMF yield the most reliable estimates in terms of source locations and powers. The integrated levels obtained by all the algorithms were shown to collapse with the reference microphone levels over a frequency range from 0.5 kHz to 12 kHz. It was shown that with coherent sources, none of the algorithms can distinguish the sources unless the frequency is high (in which case all algorithms except CLEAN-SC was shown to perform reasonably well). It was also shown that the coherence of the sources results in severe interference losses over the array aperture. Finally, DAS and CLEAN-SC were shown to be fastest in terms of computation followed by SC-DAMAS, CMF and DAMAS.

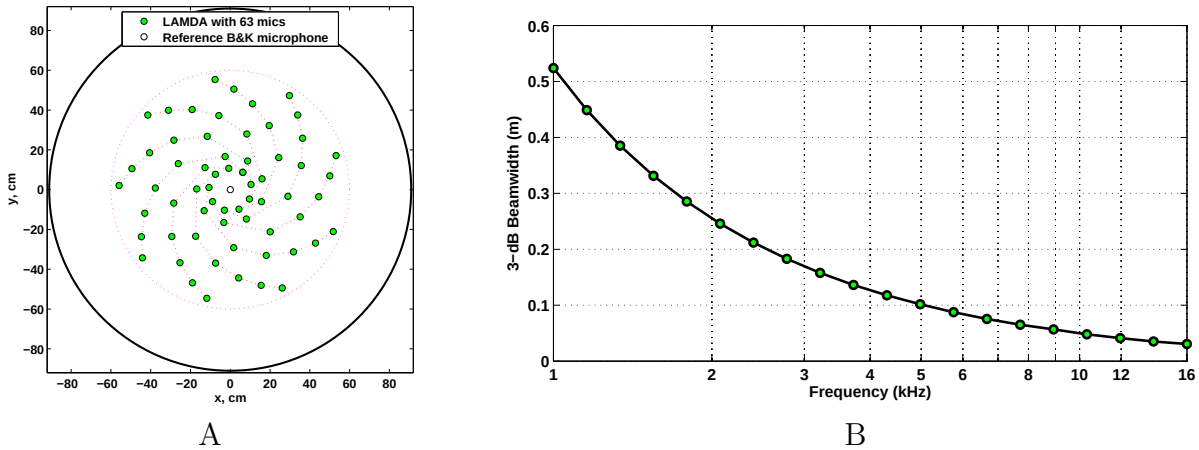

Figure 4-1. LAMDA characteristics. A) The microphone layout of LAMDA. The solid circle shows the aluminum plate of LAMDA. A reference B&K microphone (not an element of LAMDA) is included in the array center for comparison purposes. B) The 3-dB beamwidth of LAMDA versus frequency.

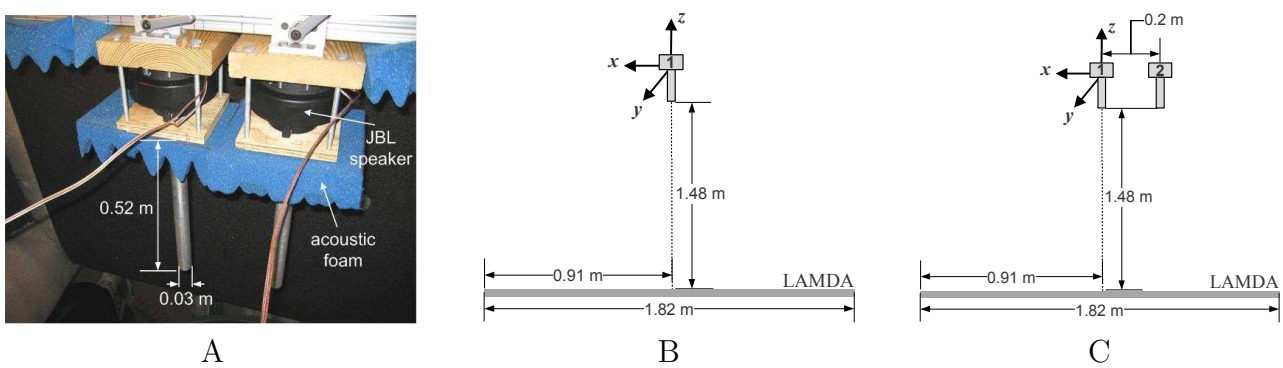

Figure 4-2. Experimental setup. A) Speakers used in the experiments were custom built using JBL type 2426H speakers. B) Setup 1 consists of a single source placed 1.48 m above the LAMDA plate. C) Setup 2 consists of two sources placed 0.20 m apart from each other.

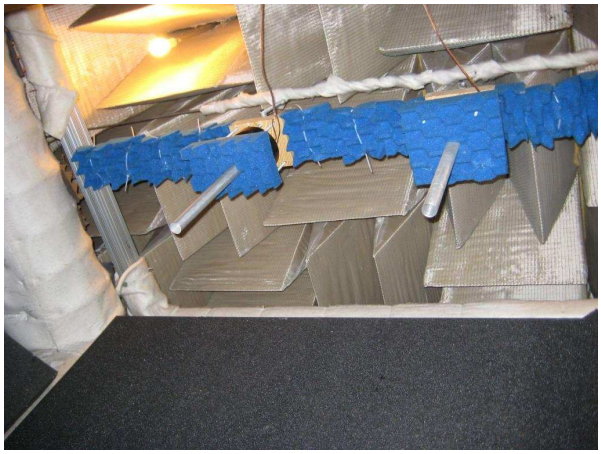

A

B

Figure 4-3. Pictures from the experiments. A) A picture of the two speakers as seen from near the array plate during testing. B) A picture of LAMDA during testing.

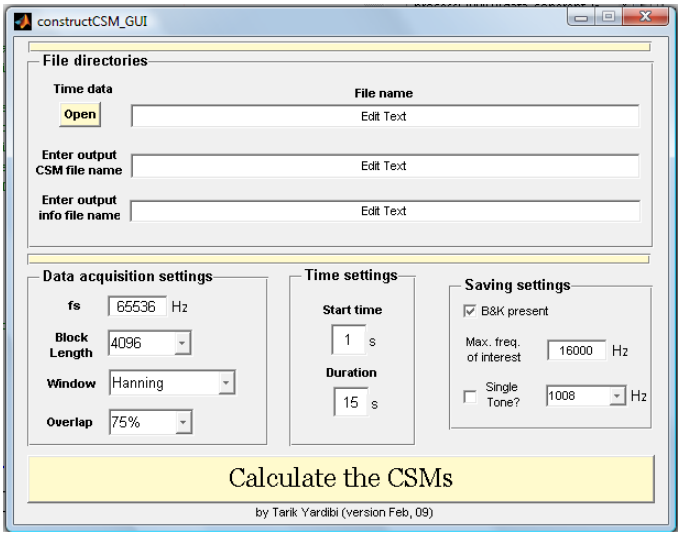

Figure 4-4. The GUI used for constructing the CSMs from the raw time data.

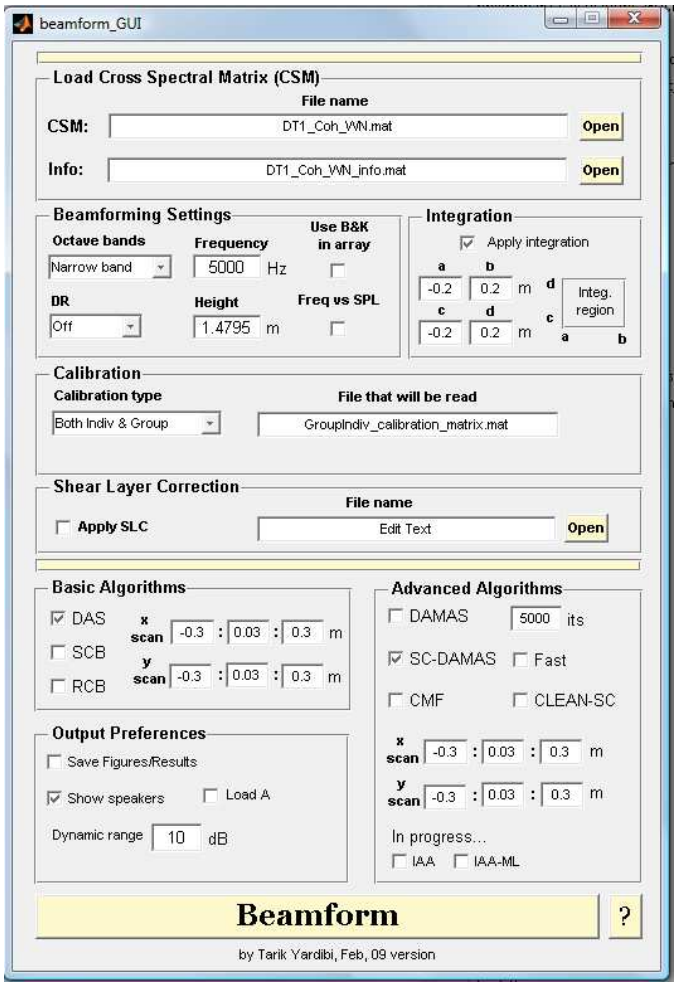

Figure 4-5. The beamforming GUI used for the post-processing of the CSMs.

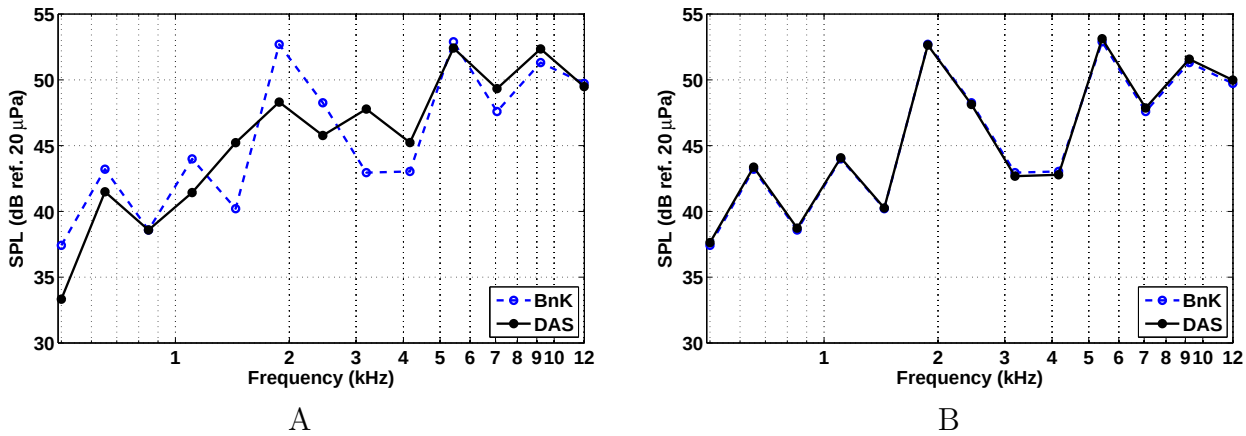

Figure 4-6. Comparison of DAS integrated levels with the reference B&K microphone levels A) without array calibration and B) with array calibration.

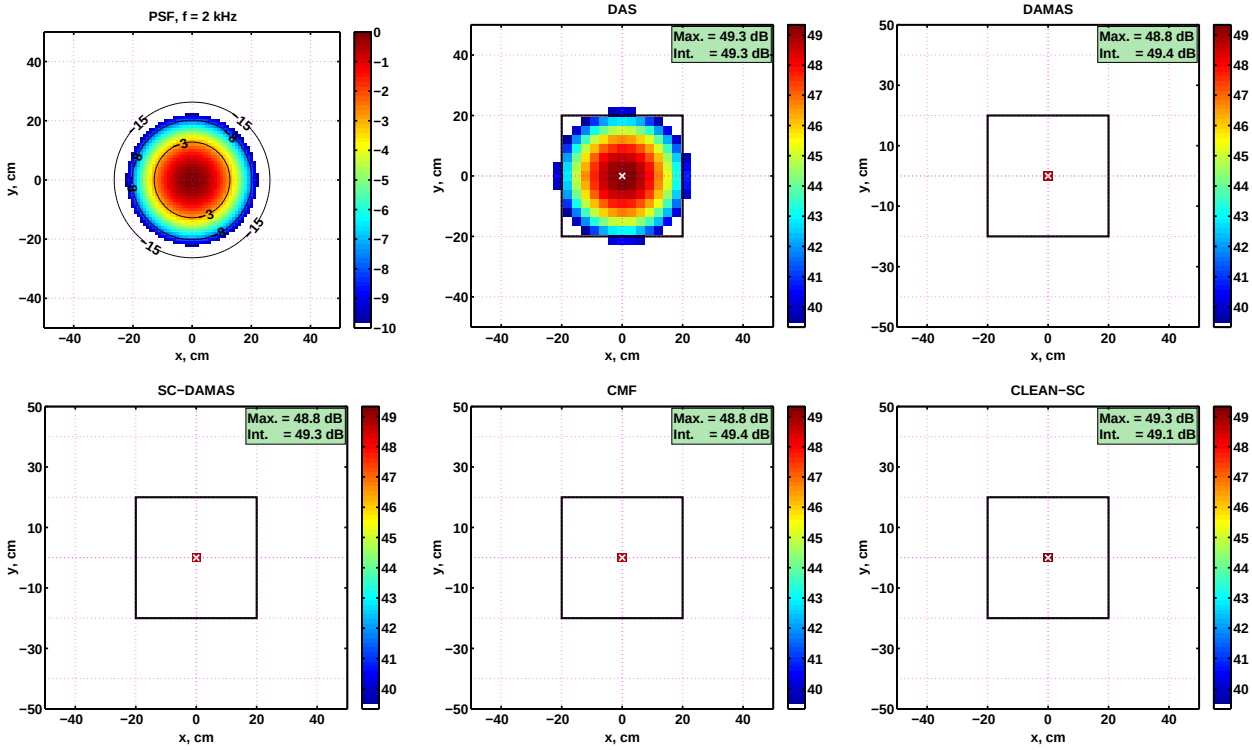

Figure 4-7. The array point spread function (levels in normalized dB) and the beamforming images (levels in dB) obtained using DAS, DAMAS, SC-DAMAS, CMF and CLEAN-SC for a single source located at a distance of 1.48 m from the array center (setup 1). The integration region is indicated with the solid rectangle, and the integrated (Int.) and maximum (Max.) levels are shown in the upper right corner of each plot. The true source location is indicated by the cross. Beamforming frequency is 2 kHz and the reference microphone level is 49.4 dB. The results are obtained using experimental data.

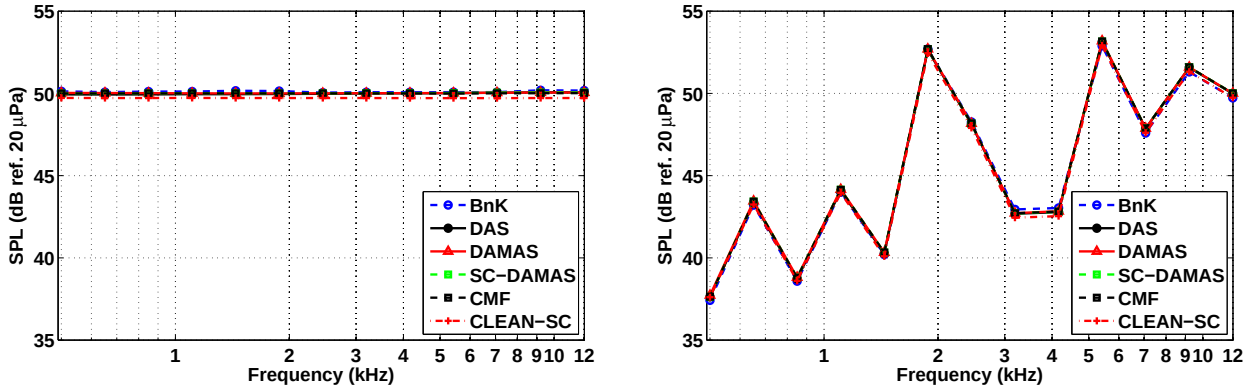

A B

Figure 4-8. Comparison of the beamformer integrated levels with the reference B&K microphone levels for a single source located at a distance of 1.48 m from the array center (setup 1). A) Simulated data and B) experimental data.

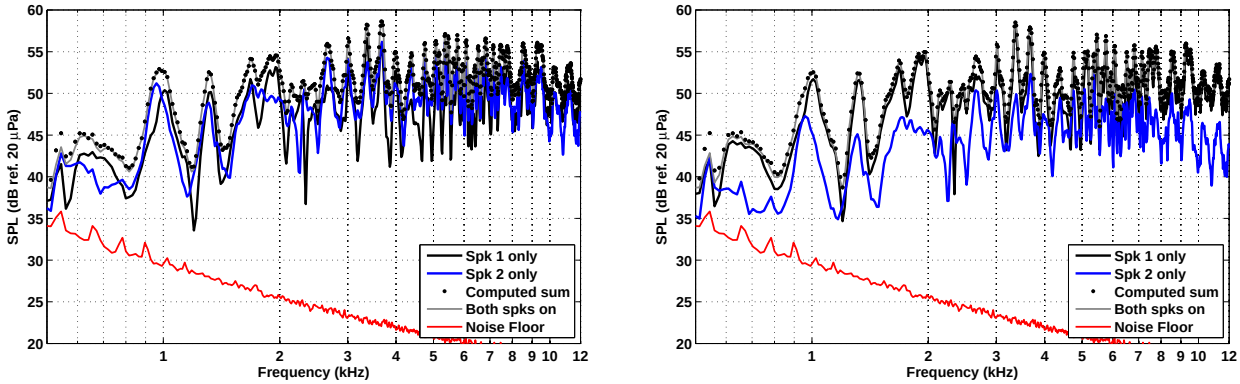

A B

Figure 4-9. The reference microphone levels when the speakers generate signals with A) similar powers and B) different powers. The levels when either one of the speakers is on and both of the speakers are on are shown together with the computed sum of the levels obtained when either one of the speakers is on. The results are obtained using experimental data.

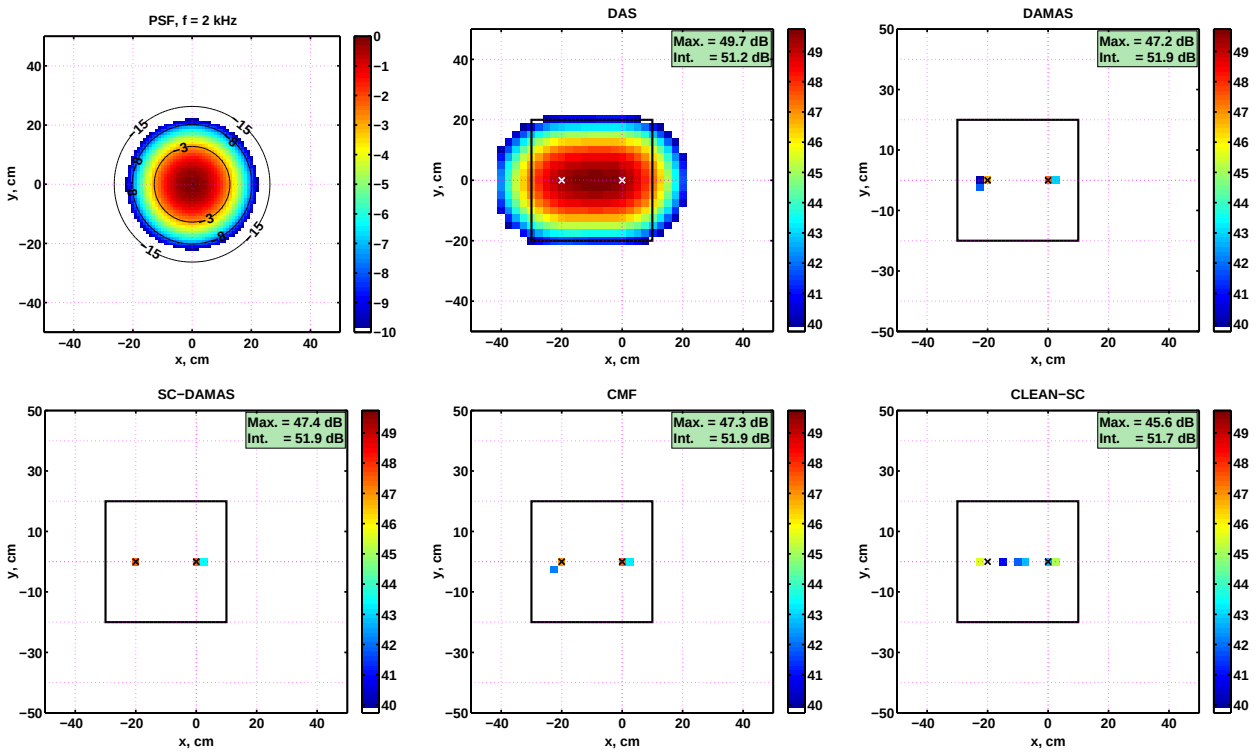

Figure 4-10. The array point spread function (levels in normalized dB) and the beamforming images (levels in dB) obtained using DAS, DAMAS, SC-DAMAS, CMF and CLEAN-SC for two uncorrelated sources with similar powers located 0.20 m apart from each other (setup 2). The integration region is indicated with the solid rectangle, and the integrated (Int.) and maximum (Max.) levels are shown in the upper right corner of each plot. The true source locations are indicated by the crosses. Beamforming frequency is 2 kHz and the reference microphone level is 52.6 dB. The results are obtained using experimental data.

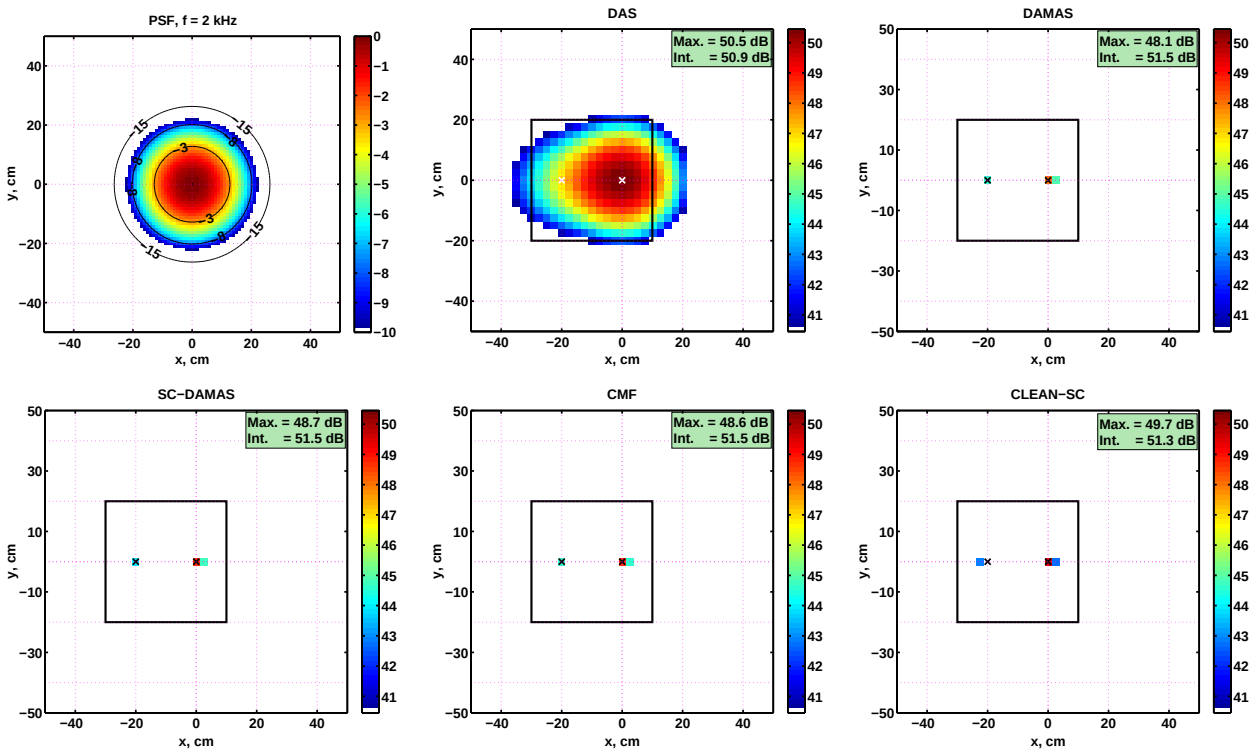

Figure 4-11. The array point spread function (levels in normalized dB) and the beamforming images (levels in dB) obtained using DAS, DAMAS, SC-DAMAS, CMF and CLEAN-SC for two uncorrelated sources with different powers located 0.20 m apart from each other (setup 2). The integration region is indicated with the solid rectangle, and the integrated (Int.) and maximum (Max.) levels are shown in the upper right corner of each plot. The true source locations are indicated by the crosses. Beamforming frequency is 2 kHz and the reference microphone level is 52.3 dB. The results are obtained using experimental data.

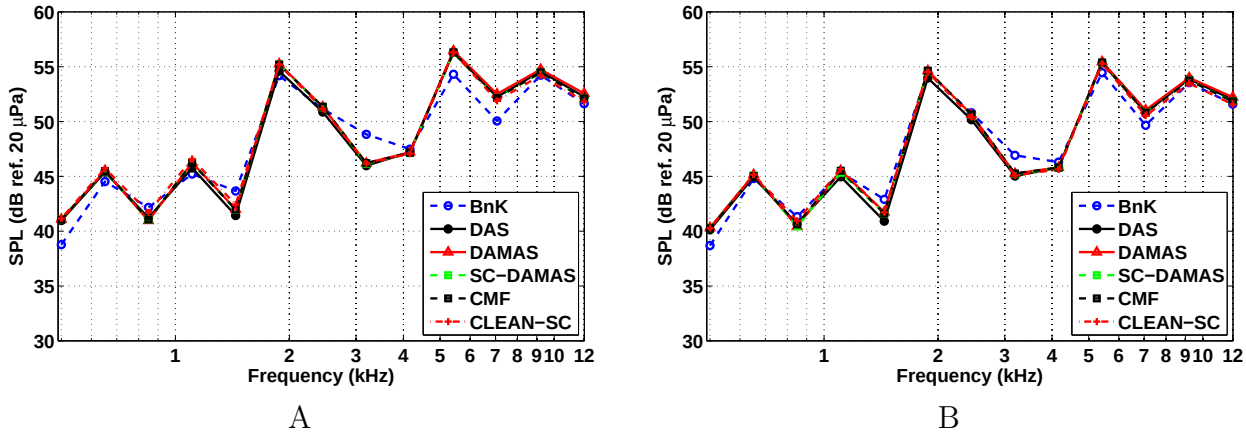

Figure 4-12. Comparison of the beamformer integrated levels with the reference microphone levels for two uncorrelated sources located 0.20 m apart from each other (setup 2). A) The two sources are of similar power in A) and the source at $(x, y) = (0, 0)$ m is stronger than the source at $(x, y) = (-0.2, 0)$ m in B). The results are obtained using experimental data.

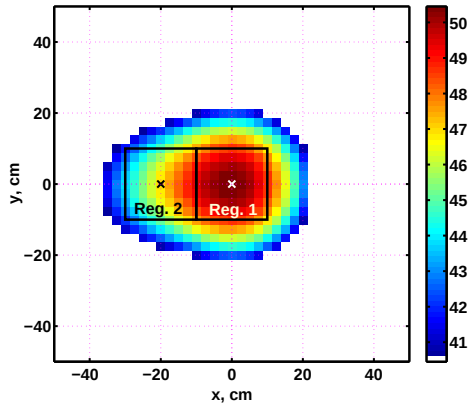

Figure 4-13. Integration region 1 (Reg. 1) and integration region 2 (Reg. 2) are used when estimating the power of sources 1 and 2, respectively.

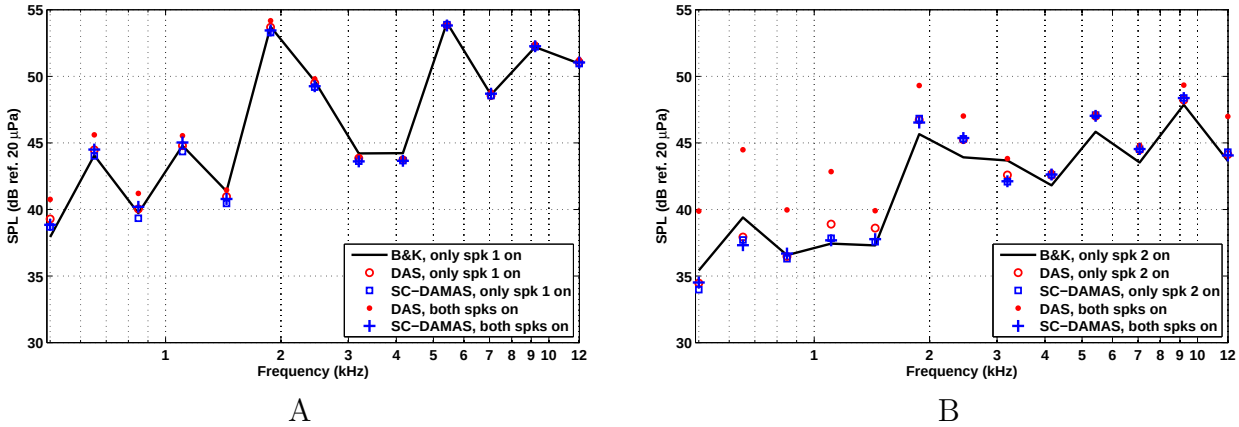

Figure 4-14. Comparison of the DAS and SC-DAMAS integrated levels with the reference microphone levels for two uncorrelated sources with different powers located 0.20 m apart from each other (setup 2). A) DAS and SC-DAMAS integrated levels for source 1 (calculated over Reg. 1) are shown when only speaker 1 is on and when both speakers are on. The reference B&K microphone levels are shown when only speaker 1 is on. B) DAS and SC-DAMAS integrated levels for source 2 (calculated over Reg. 2) are shown when only speaker 2 is on and when both speakers are on. B&K levels are shown when only speaker 2 is on. The results are obtained using experimental data.

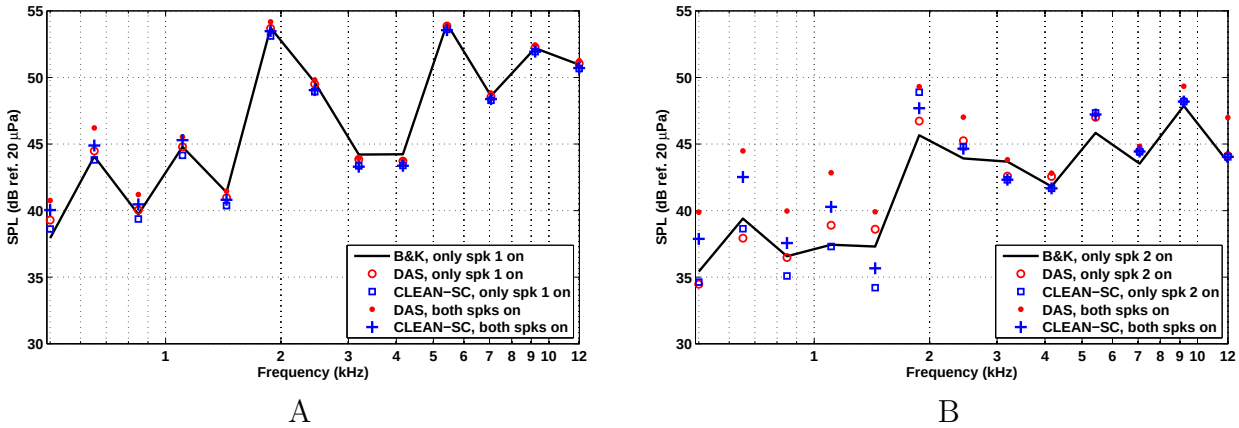

Figure 4-15. Comparison of the DAS and CLEAN-SC integrated levels with the reference microphone levels for two uncorrelated sources with different powers located 0.20 m apart from each other (setup 2). A) DAS and SC-DAMAS integrated levels for source 1 (calculated over Reg. 1) are shown when only speaker 1 is on and when both speakers are on. The reference B&K microphone levels are shown when only speaker 1 is on. B) DAS and SC-DAMAS integrated levels for source 2 (calculated over Reg. 2) are shown when only speaker 2 is on and when both speakers are on. B&K levels are shown when only speaker 2 is on. The results are obtained using experimental data.

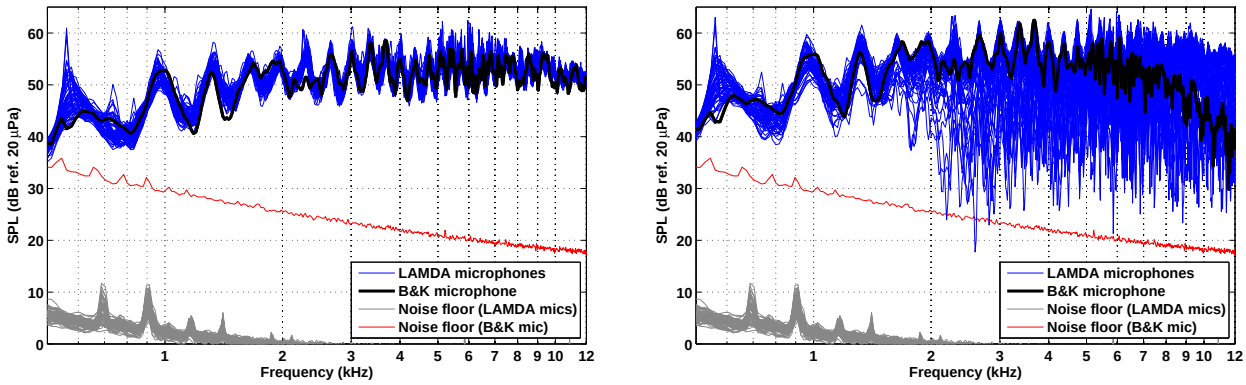

Figure 4-16. The sound pressure levels measured by the reference B&K microphone and the LAMDA microphones when the two sources are A) uncorrelated with similar powers and B) coherent.

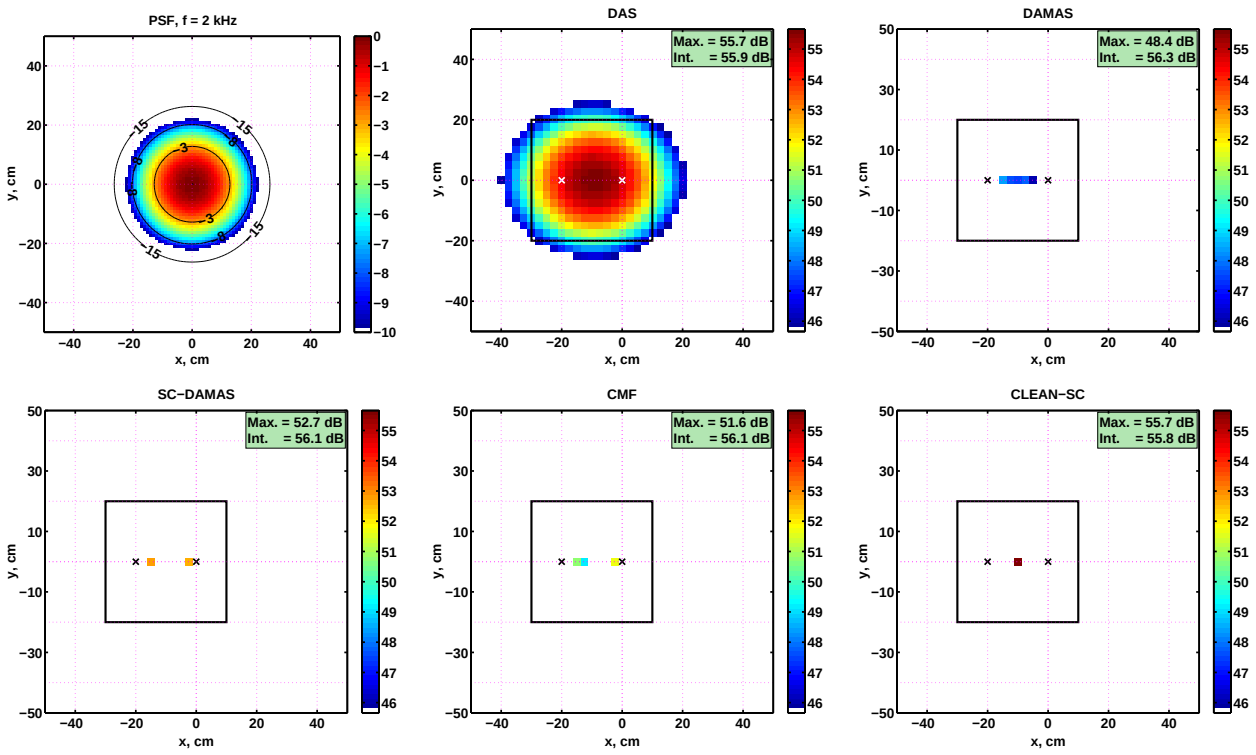

Figure 4-17. The array point spread function (levels in normalized dB) and the beamforming images (levels in dB) obtained using DAS, DAMAS, SC-DAMAS, CMF and CLEAN-SC for two coherent sources located 0.20 m apart from each other (setup 2). The integration region is indicated with the solid rectangle, and the integrated (Int.) and maximum (Max.) levels are shown in the upper right corner of each plot. The true source locations are indicated by the crosses. Beamforming frequency is 2 kHz and the reference microphone level is 58.2 dB. The results are obtained using experimental data.

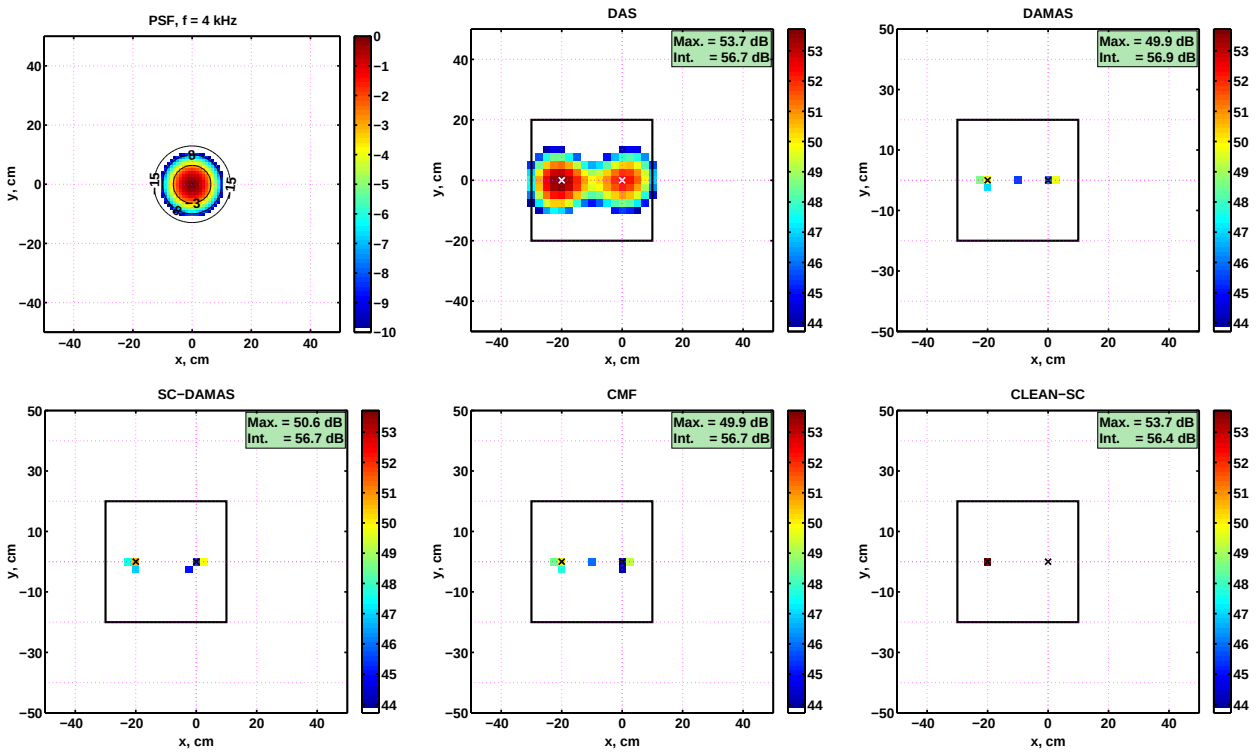

Figure 4-18. The array point spread function (levels in normalized dB) and the beamforming images (levels in dB) obtained using DAS, DAMAS, SC-DAMAS, CMF and CLEAN-SC for two coherent sources located 0.20 m apart from each other (setup 2). The integration region is indicated with the solid rectangle, and the integrated (Int.) and maximum (Max.) levels are shown in the upper right corner of each plot. The true source locations are indicated by the crosses. Beamforming frequency is 4 kHz and the reference microphone level is 58.3 dB. The results are obtained using experimental data.

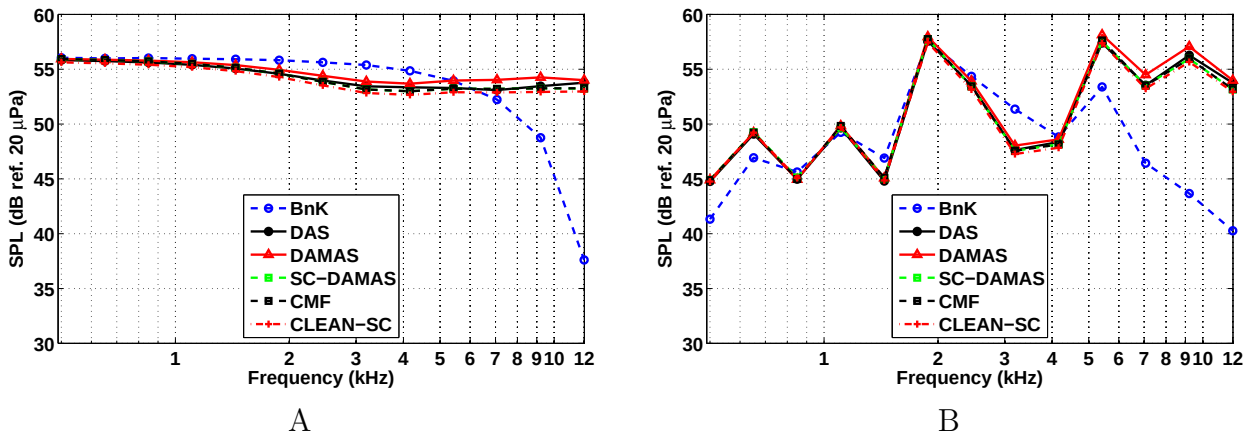

Figure 4-19. Comparison of the beamformer integrated levels with the reference microphone levels for two coherent sources located 0.20 m apart from each other (setup 2). A) Simulated data and B) experimental data.

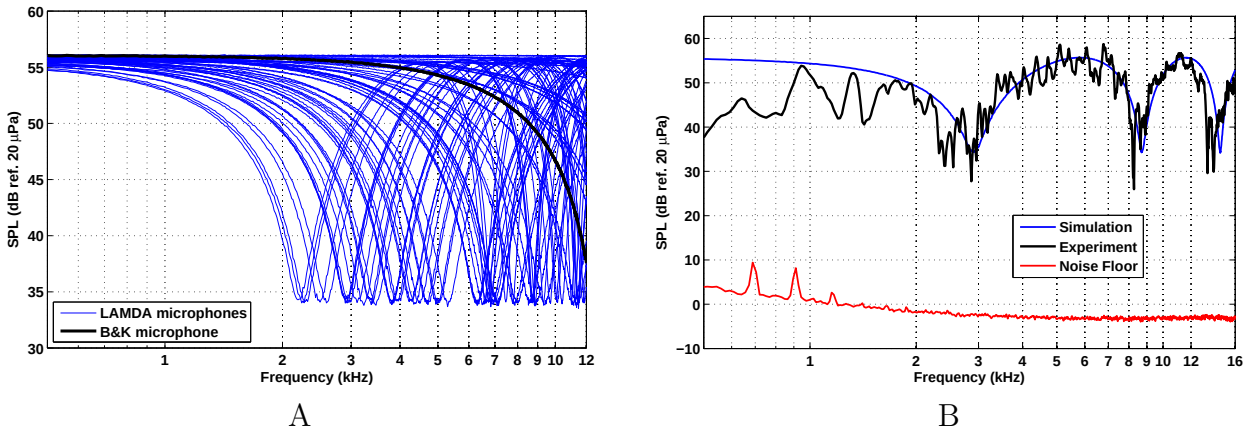

Figure 4-20. Interference due to source coherence. A) The interference induced by the coherence of the sources at each microphone (using simulated data). B) The comparison of the simulated with measured interference effect.

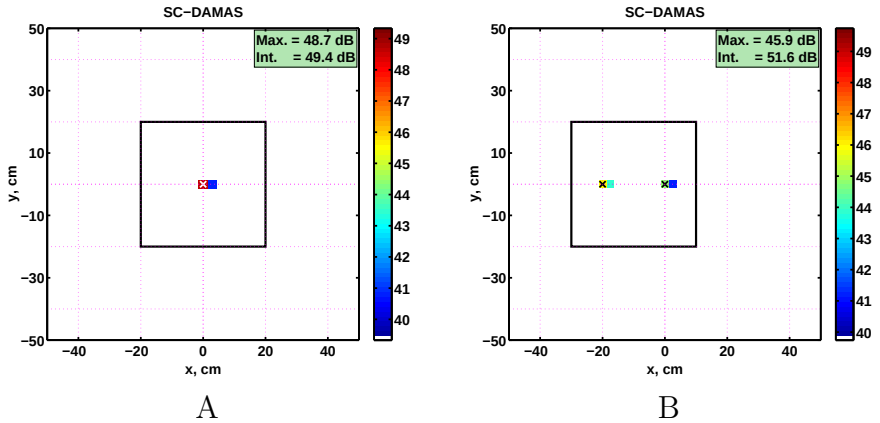

Figure 4-21. The beamforming maps obtained using the fast SC-DAMAS. A) For a single source located at a distance of 1.48 m from the array center (setup 1). Compare to Figure 4-7. B) For two uncorrelated sources with similar powers located 0.20 m apart from each other (setup 2). Compare to Figure 4-10.

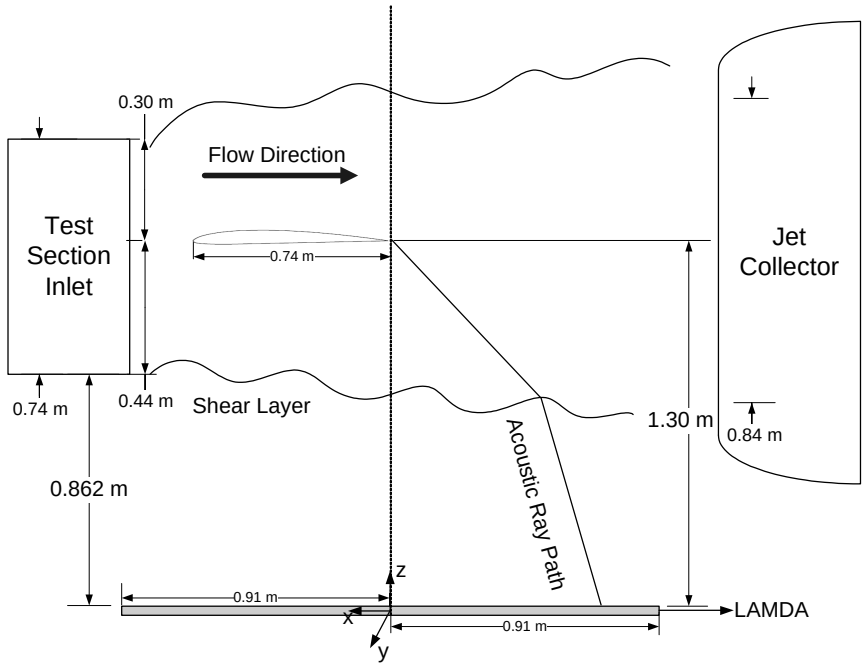

Figure 4-22. The experimental setup for the NACA 63-215 Mod-B airfoil acoustic measurements. Courtesy of Chris Bahr.

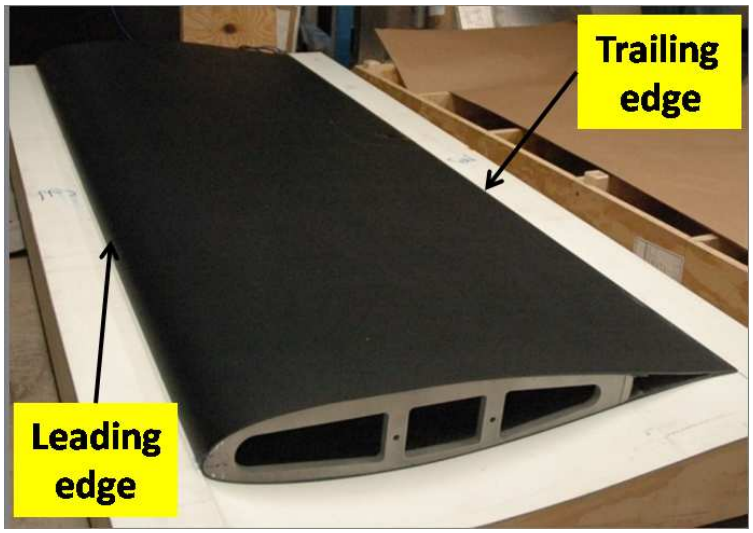

Figure 4-23. Picture of the NACA 63-215 Mod-B airfoil. Courtesy of Chris Bahr.

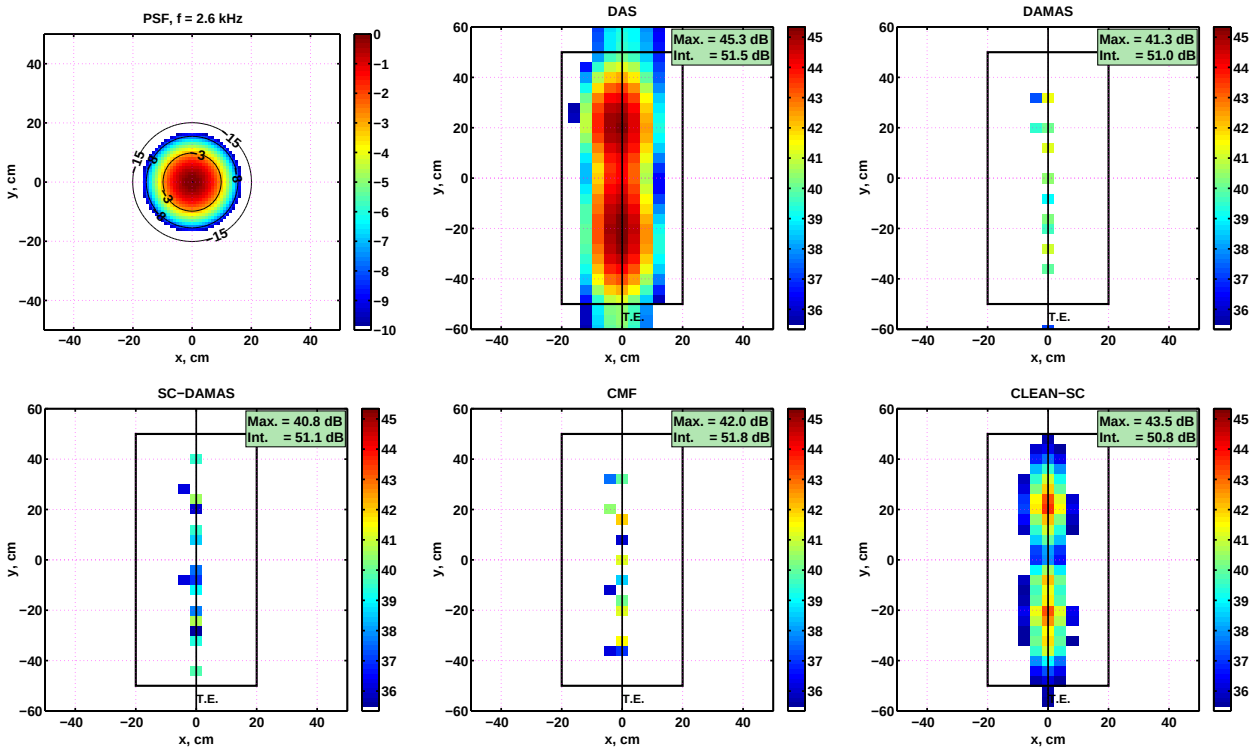

Figure 4-24. The array point spread function (levels in normalized dB) and the beamforming images (levels in dB) obtained using DAS, DAMAS, SC-DAMAS, CMF and CLEAN-SC for the NACA 63-215 airfoil and with a Mach number of 0.17. The integration region is indicated with the solid rectangle, and the integrated (Int.) and maximum (Max.) levels are shown in the upper right corner of each plot. The solid line at $x = 0$ m indicates the trailing edge (T.E.) and the leading edge is at x=0.74 m (not shown). Beamforming frequency is 2.6 kHz. The results are obtained using experimental data.

Table 4-1. Computation times (in seconds) on a personal computer (2.53 GHz processor and 3 Gbytes of RAM).

No. of grids	DAS	DAMAS	SC-DAMAS	CMF	CLEAN-SC	SC-DAMAS (Fast)
441	0.3	78.0	12.3	69.2	1.2	4.2
625	0.6	138.0	31.8	123.5	1.6	11.6

CHAPTER 5
DECONVOLUTION WITH CORRELATED SOURCES

When the acoustic signals generated by the sources are correlated, Eq. 3–3 is no longer valid and, as a result, the number of real-valued unknowns in $\mathbf{P} = \mathrm{E}[\mathbf{s}(b)\mathbf{s}^H(b)]$ (see Eq. 3–2) increases to L^2 (note that $\mathbf{P}$ is no longer a diagonal matrix now but it is Hermitian symmetric, i.e., $\mathbf{P}^H = \mathbf{P}$). In the following, the measurement noise is assumed to be removed from $\hat{\mathbf{G}}$. Discussions on how this can be done in practice are provided in Section 5.4.

The DAS power estimates for correlated sources becomes [24]

$$\hat{P}_{l,l'}^{(\mathrm{D})} = \frac{1}{M^2}\tilde{\mathbf{a}}_l^H \hat{\mathbf{G}} \tilde{\mathbf{a}}_{l'}, \quad l, l' = 1, \ldots, L, \tag{5–1}$$

and this algorithm is referred to as DAS-C.

5.1 An Existing Deconvolution Approach

The counterpart of DAMAS for correlated sources, DAMAS-C, solves

$$\underbrace{\begin{bmatrix} \hat{P}_{1,1}^{(\mathrm{D})} \\ \vdots \\ \hat{P}_{1,L}^{(\mathrm{D})} \\ \hat{P}_{2,2}^{(\mathrm{D})} \\ \vdots \\ \hat{P}_{L,L}^{(\mathrm{D})} \end{bmatrix}}_{\hat{\mathbf{p}}_{\mathrm{c}}^{(\mathrm{D})}} = \frac{1}{M^2} \underbrace{\begin{bmatrix} |\tilde{\mathbf{a}}_1^H \mathbf{a}_1|^2 & \tilde{\mathbf{a}}_1^H \mathbf{a}_1 \mathbf{a}_2^H \tilde{\mathbf{a}}_1 & \ldots & \tilde{\mathbf{a}}_1^H \mathbf{a}_L \mathbf{a}_L^H \tilde{\mathbf{a}}_1 \\ \vdots & \vdots & \ddots & \vdots \\ \tilde{\mathbf{a}}_1^H \mathbf{a}_1 \mathbf{a}_1^H \tilde{\mathbf{a}}_L & \tilde{\mathbf{a}}_1^H \mathbf{a}_1 \mathbf{a}_2^H \tilde{\mathbf{a}}_L & \ldots & \tilde{\mathbf{a}}_1^H \mathbf{a}_L \mathbf{a}_L^H \tilde{\mathbf{a}}_L \\ \tilde{\mathbf{a}}_2^H \mathbf{a}_1 \mathbf{a}_1^H \tilde{\mathbf{a}}_2 & \tilde{\mathbf{a}}_2^H \mathbf{a}_1 \mathbf{a}_2^H \tilde{\mathbf{a}}_2 & \ldots & \tilde{\mathbf{a}}_2^H \mathbf{a}_L \mathbf{a}_L^H \tilde{\mathbf{a}}_2 \\ \vdots & \vdots & \ddots & \vdots \\ \tilde{\mathbf{a}}_L^H \mathbf{a}_1 \mathbf{a}_1^H \tilde{\mathbf{a}}_L & \tilde{\mathbf{a}}_L^H \mathbf{a}_1 \mathbf{a}_2^H \tilde{\mathbf{a}}_L & \ldots & |\tilde{\mathbf{a}}_L^H \mathbf{a}_L|^2 \end{bmatrix}}_{\tilde{\mathbf{A}}_{\mathrm{c}}} \underbrace{\begin{bmatrix} P_{1,1} \\ \vdots \\ P_{1,L} \\ P_{2,2} \\ \vdots \\ P_{L,L} \end{bmatrix}}_{\mathbf{p}_{\mathrm{c}}}, \tag{5–2}$$

for $\mathbf{p}_{\mathrm{c}} \in \mathbb{C}^{L(L+1)/2\times 1}$ given $\hat{\mathbf{p}}_{\mathrm{c}}^{(\mathrm{D})} \in \mathbb{C}^{L(L+1)/2\times 1}$ and $\tilde{\mathbf{A}}_{\mathrm{c}} \in \mathbb{C}^{L(L+1)/2\times L(L+1)/2}$. Note that since $\mathbf{P}$ is Hermitian symmetric, only $P_{l,l'}$ for $l' \geq l$, $l, l' = 1, \ldots, L$, should be estimated. DAMAS-C also uses the Gauss-Seidel method (see Eq. 3–9), as described previously, to solve Eq. 5–2. A major drawback of DAMAS-C is that it assumes that the cross-correlation level of any two sources is real and non-negative, i.e., $P_{l,l'} \geq 0$ for $l, l' = 1, \ldots, L$.

5.2 Covariance Matrix Fitting with Correlated Sources

We devise CMF-C, which is an extension of CMF to the correlated source case, as an alternative to DAMAS-C. CMF-C solves [53]:

$$\min_{\mathbf{P}} \quad \|\hat{\mathbf{G}} - \mathbf{A}\mathbf{P}\mathbf{A}^H\|_{\mathrm{F}}^2, \quad \text{s.t.} \quad \mathrm{tr}(\mathbf{P}) \leq \beta, \quad \mathbf{P} \succeq 0, \tag{5–3}$$

which is a convex semi-definite program (SDP) that can be solved with SeDuMi. CMF-C allows for complex-valued cross-correlation values and hence is more general than DAMAS-C. Note that CMF-C reduces to CMF when the sources are uncorrelated.

Due to the significant increase in the number of unknowns in the presence of correlated sources (from L to L^2), DAMAS-C and CMF-C are impractical computation-wise even for a small number of scanning grids (an example using only 36 scanning points was shown in [53]). Therefore, beamforming algorithms that can work with correlated (even coherent) sources with much lower computational complexities are desirable. We present such an approach in the following and demonstrate its ability to separate partially correlated or coherent sources using simulations as well as experimental data.

5.3 A Fast Beamformer for Correlated Sources

The algorithm presented in this section makes use of the fact that the number of non-zero eigenvalues of the (noise-free) CSM is smaller than or equal to the number of sources [8, 9], which is much smaller than the number of scanning points. Therefore, if a rough estimate of the number of sources is available, the problem dimension can be reduced significantly as will be shown below. Moreover, as shown in the results section, the proposed algorithm is quite insensitive to the (over) estimation of the number of sources.

The first step in reducing the problem dimension is to truncate the eigenvalues of the CSM that are almost zero. For this purpose, let $\hat{\mathbf{G}} = \mathbf{U}\mathbf{\Lambda}\mathbf{U}^H$ be the EVD of $\hat{\mathbf{G}}$, where the columns of the unitary matrix $\mathbf{U} \in \mathbb{C}^{M\times M}$ are the eigenvectors of $\hat{\mathbf{G}}$ and the diagonal elements of the diagonal matrix $\mathbf{\Lambda} \in \mathbb{R}^{M\times M}$ are the corresponding eigenvalues $\{\lambda_m\}_{m=1}^M$

such that $\lambda_1 \geq \ldots \geq \lambda_M \geq 0$. Furthermore, let $\mathbf{G}_{\hat{L}} \in \mathbb{C}^{M\times M}$ denote the covariance matrix obtained by keeping only the $\hat{L} \ll M$ largest eigenvalues of $\hat{\mathbf{G}}$ (since the rest of the eigenvalues will be very small when the noise is removed from the CSM), i.e.,

$$\mathbf{G}_{\hat{L}} = \mathbf{U} \begin{bmatrix} \mathbf{\Lambda}_{\hat{L}} & \mathbf{0} \\ \mathbf{0} & \mathbf{0} \end{bmatrix} \mathbf{U}^H = \mathbf{U}_{\hat{L}} \mathbf{\Lambda}_{\hat{L}} \mathbf{U}_{\hat{L}}^H, \tag{5–4}$$

where $\hat{L}$ is an estimate of the number of sources, $\mathbf{U}_{\hat{L}} \in \mathbb{C}^{M\times \hat{L}}$ consists of the first $\hat{L}$ columns of $\mathbf{U}$, $\mathbf{U}_{\hat{L}}^H \mathbf{U}_{\hat{L}} = \mathbf{I}$, and

$$\mathbf{\Lambda}_{\hat{L}} = \begin{bmatrix} \lambda_1 & & \mathbf{0} \\ & \ddots & \\ \mathbf{0} & & \lambda_{\hat{L}} \end{bmatrix}. \tag{5–5}$$

Replacing $\hat{\mathbf{G}}$ by $\mathbf{G}_{\hat{L}}$, Eq. 5–3 can be written as:

$$\min_{\mathbf{P}} \quad \|\mathbf{G}_{\hat{L}} - \mathbf{A}\mathbf{P}\mathbf{A}^H\|_{\mathrm{F}}^2, \quad \text{s.t.} \quad \mathrm{tr}(\mathbf{P}) \leq \beta, \quad \mathbf{P} \succeq 0, \tag{5–6}$$

where $\beta = \mathrm{tr}(\mathbf{\Lambda})$ [53].

The second step for reducing the problem dimension is to replace $\mathbf{P}$ in the above optimization with a smaller matrix $\mathbf{C} \in \mathbb{C}^{L\times \hat{L}}$ of rank less than or equal to $\hat{L}$, such that $\mathbf{C}\mathbf{C}^H = \mathbf{P}$. This ensures that $\mathbf{P}$ is Hermitian symmetric, positive semi-definite and of rank at most $\hat{L}$, as desired. Then, Eq. 5–6 becomes

$$\min_{\mathbf{C}} \quad \|\mathbf{G}_{\hat{L}} - \mathbf{A}\mathbf{C}(\mathbf{A}\mathbf{C})^H\|_{\mathrm{F}}^2, \quad \text{s.t.} \quad \|\mathbf{C}\|_{\mathrm{F}}^2 \leq \beta. \tag{5–7}$$

However, even after these simplifications, it is still difficult to solve the quartic problem in Eq. 5–7. Therefore, in an attempt to further simplify Eq. 5–7, we write it in the following equivalent form:

$$\min_{\mathbf{C}} \quad \|(\tilde{\mathbf{G}}\mathbf{Q}^H)(\tilde{\mathbf{G}}\mathbf{Q}^H)^H - \mathbf{A}\mathbf{C}(\mathbf{A}\mathbf{C})^H\|_{\mathrm{F}}^2, \quad \text{s.t.} \quad \|\mathbf{C}\|_{\mathrm{F}}^2 \leq \beta, \quad \mathbf{Q}^H\mathbf{Q} = \mathbf{I}, \tag{5–8}$$

where $\tilde{\mathbf{G}} = \mathbf{U}_{\hat{L}}(\mathbf{\Lambda}_{\hat{L}})^{1/2} \in \mathbb{C}^{M\times\hat{L}}$ such that $\tilde{\mathbf{G}}\tilde{\mathbf{G}}^H = \mathbf{G}_{\hat{L}}$, and $\mathbf{Q} \in \mathbb{C}^{\hat{L}\times\hat{L}}$ is an arbitrary unitary matrix such that $\mathbf{Q}^H\mathbf{Q} = \mathbf{Q}\mathbf{Q}^H = \mathbf{I}$. The auxiliary variable $\mathbf{Q}$ has been introduced in Eq. 5–8 to obtain a more convenient cost function whose minimization should give similar results to those obtained from Eq. 5–7 [60–62]:

$$\min_{\mathbf{Q},\mathbf{C}} \quad \|\tilde{\mathbf{G}}\mathbf{Q}^H - \mathbf{A}\mathbf{C}\|_{\mathrm{F}}^2, \quad \text{s.t.} \quad \|\mathbf{C}\|_{\mathrm{F}}^2 \leq \beta, \quad \mathbf{Q}^H\mathbf{Q} = \mathbf{I}. \tag{5–9}$$

Indeed, if the cost function in Eq. 5–9 can be minimized to a small value, then the cost function in Eq. 5–8 will also be small and vice versa (more details on this transition is provided in [62]).

Solving the problem in Eq. 5–9 requires the joint estimation of both $\mathbf{Q}$ and $\mathbf{C}$, which can be done by means of a cyclic methodology in which the cost function is minimized in an alternating fashion with respect to $\mathbf{Q}$ or $\mathbf{C}$, while the other variable is assumed given. After performing a certain number of iterations, the estimate of $\mathbf{P}$, denoted as $\hat{\mathbf{P}}$, will be given by $\hat{\mathbf{C}}\hat{\mathbf{C}}^H$, where $\hat{\mathbf{C}}$ is the final estimate of $\mathbf{C}$. This approach is much faster than trying to solve Eq. 5–3 as the number of unknowns when estimating $\mathbf{Q}$ or $\mathbf{C}$ is much smaller than the number of unknowns when estimating $\mathbf{P}$.

However, the Frobenius norm constraint on $\mathbf{C}$ does not lead to good performance in general since $\mathbf{C}$ is expected to be sparse (as $\mathbf{P}$ is sparse) and the Frobenius norm does not promote sparsity [28]. Accordingly, one can replace the Frobenius norm in Eq. 5–9 with the ℓ_1-norm, which is widely used in the literature on recovery of sparse signals, see, e.g., [28], to achieve a sparse estimate of $\mathbf{C}$ (and consequently $\mathbf{P}$):

$$\min_{\mathbf{Q},\mathbf{C}} \quad \|\tilde{\mathbf{G}}\mathbf{Q}^H - \mathbf{A}\mathbf{C}\|_{\mathrm{F}}^2, \quad \text{s.t.} \quad \|\mathbf{c}\|_1 \leq \xi, \quad \mathbf{Q}^H\mathbf{Q} = \mathbf{I}, \tag{5–10}$$

where $\mathbf{c} = \mathrm{vec}(\mathbf{C})$ and the user parameter ξ is selected by using the Cauchy-Schwartz inequality [63] as follows (recall that $\beta = \mathrm{tr}(\mathbf{\Lambda})$):

$$\sum_{l=1}^{L\hat{L}} |c_l| \leq \sqrt{\sum_{l=1}^{L\hat{L}} |c_l|^2 (L\hat{L})} \leq \sqrt{\beta L\hat{L}} = \xi. \tag{5–11}$$

For given $\mathbf{Q}$, the problem in Eq. 5–10 is a second-order cone program (SOCP) that can be solved for $\mathbf{C}$ efficiently by using SeDuMi. Furthermore, for given $\mathbf{C}$, Eq. 5–10 can be solved for $\mathbf{Q}$ by using the method described in [64]. Note that

$$\|\tilde{\mathbf{G}}\mathbf{Q}^H - \mathbf{A}\mathbf{C}\|_{\mathrm{F}}^2 = \phi - 2\mathrm{Re}\left[\mathrm{tr}(\tilde{\mathbf{G}}^H\mathbf{A}\mathbf{C}\mathbf{Q})\right], \tag{5–12}$$

where ϕ is some constant term not depending on $\mathbf{Q}$. Let $\tilde{\mathbf{G}}^H\mathbf{A}\mathbf{C} = \hat{\mathbf{U}}\tilde{\mathbf{\Sigma}}\tilde{\mathbf{U}}^H$ be the singular-value decomposition (SVD) of $\tilde{\mathbf{G}}^H\mathbf{A}\mathbf{C}$, where $\hat{\mathbf{U}} \in \mathbb{C}^{\hat{L}\times\hat{L}}$ and $\tilde{\mathbf{U}} \in \mathbb{C}^{\hat{L}\times\hat{L}}$. Then, the solution to Eq. 5–10 is given by [64]:

$$\hat{\mathbf{Q}} = \tilde{\mathbf{U}}\hat{\mathbf{U}}^H. \tag{5–13}$$

The algorithm that estimates $\mathbf{C}$ via Eq. 5–10 and $\mathbf{Q}$ via Eq. 5–13 in an iterative manner is referred to as MACS. For implementing MACS, first $\mathbf{I}$ is used as an initial estimate for $\mathbf{Q}$ and $\mathbf{C}$ is estimated. Then given the estimated $\mathbf{C}$, $\mathbf{Q}$ is updated and so on. Table 5-1 outlines the MACS algorithm. MACS is a cyclic algorithm, i.e., the cost function is guaranteed to decrease at each iteration, and this ensures that MACS will converge at least locally. It was empirically observed that usually no significant improvement in performance is achieved with MACS after 5 iterations (it is also possible to implement the algorithm until no significant improvement in $\hat{\mathbf{P}}$ is achieved in two consecutive iterations).

The computational complexity of MACS per iteration is mainly dictated by the complexity of the SOCP in Eq. 5–10, which is given by $\mathcal{O}(L^3\hat{L}^3)$ [65] (the complexity of CMF-C is $\mathcal{O}(L^6)$ and that of DAMAS-C is $\mathcal{O}(L^4)$ times the number of DAMAS-C iterations required for convergence which is usually on the order of ten thousands [24]). It is important to note that the actual computation time does not depend solely on the number of multiplication and division operations as considered when reporting the complexity of the algorithm but rather is a function of the memory access time, the implementation software and hardware, and the number of computations combined

together. Sample running times for MACS will be provided in the numerical examples section.

Note that $P_{l,l'}$ estimated with DAMAS-C, CMF-C and MACS should be divided by $r_{l,0}r_{l',0}$ for $l, l' = 1, \ldots, L$ to match the levels estimated with DAS-C.

5.4 Measurement Noise

Note that as in the uncorrelated case, DAS-C and DAMAS-C employ DR, whereas CMF-C minimizes $\|\hat{\mathbf{G}} - \mathbf{APA}^H - \sigma^2\mathbf{I}\|_{\mathrm{F}}^2$ with respect to both $\mathbf{P}$ and σ^2, thus estimating σ^2 alongside with $\mathbf{P}$. So similar to CMF, CMF-C only extracts the noise from $\hat{\mathbf{G}}$, while keeping the signal portion of the diagonal of $\hat{\mathbf{G}}$ intact. When using MACS, the white noise power is estimated using $\hat{\sigma}^2 = \frac{1}{M-\hat{L}}\sum_{m=\hat{L}+1}^{M}\lambda_m$. Then, $\mathbf{G}_{\hat{L}}$ (defined in Eq. 5–4) is replaced by

$$\mathbf{G}_{\hat{L}} = \mathbf{U}\begin{bmatrix} \mathbf{\Lambda}_{\hat{L}} - \hat{\sigma}^2\mathbf{I} & \mathbf{0} \\ \mathbf{0} & \mathbf{0} \end{bmatrix}\mathbf{U}^H = \mathbf{U}_{\hat{L}}\tilde{\mathbf{\Lambda}}_{\hat{L}}\mathbf{U}_{\hat{L}}^H. \tag{5–14}$$

and $\mathbf{\Lambda}_{\hat{L}}$ is replaced by $\tilde{\mathbf{\Lambda}}_{\hat{L}}$ in Table 5-1.

5.5 Numerical Examples

This section demonstrates the performance of DAS-C and MACS using SADA and LAMDA (see Figure 1-1). Recall that LAMDA has a much larger aperture size compared to SADA and hence has higher resolution. Both simulated and experimental data will be used to evaluate the performance of MACS.

5.5.1 Simulations

In the simulations, the noise waveforms, i.e., $\{\mathbf{e}(b)\}$ in Eq. 2–2, are generated as zero-mean circularly symmetric i.i.d. complex Gaussian random processes. The correlated signal waveforms are generated as $\tilde{\mathbf{s}}(b) = \mathbf{T}^{1/2}\bar{\mathbf{s}}(b)$, $b = 1, \ldots, B$, where $\mathbf{T}$ is the source correlation matrix such that $T_{l,l'} = \rho^{|l-l'|}$, where $l, l' = 1, \ldots, L_0$, L_0 is the actual number of sources, $0 \leq \rho \leq 1$ determines the correlation among sources and $\{\bar{\mathbf{s}}(b)\}$ are generated as zero-mean circularly symmetric i.i.d. complex Gaussian random processes with unit variance. The resulting correlated signal waveforms $\{\tilde{\mathbf{s}}(b)\}$ are then normalized so that

$\frac{1}{B}\sum_{b=1}^{B}|\tilde{s}_l(b)|^2 = P_l$ for $l = 1, \ldots, L_0$ to yield the signal waveforms $\{\mathbf{s}(b)\}$, which are used to generate the measurement vector $\{\mathbf{y}(b)\}$ using Eq. 2–2. The signal-to-noise ratio (SNR), which is defined as the ratio between the signal power and the noise power, is set to 0 dB and $B = 500$ FFT blocks are used in all the examples.

We first consider the performance of MACS with SADA when the array center of SADA is at $(x, y, z) = (0, 0, 0)$ m and the array extends along the xy-plane. Four monopole sources are placed at $(x, y, z) = (-0.20, 0.20, 1.48)$ m (source #1), $(-0.20, -0.20, 1.48)$ m (source #2), $(0.20, -0.20, 1.48)$ m (source #3) and $(0.20, 0.20, 1.48)$ m (source #4) and each source is assumed to have a signal power of 20 dB. The scanning region in both the x- and y-axes range from -0.4 m to 0.4 m and the resolution in both directions is 0.05 m. Note that with this scanning grid, $L = 289$ and CMF-C or DAMAS-C would be impractical to implement as the number of their real-valued unknowns is equal to $L^2 = 83,521$. (Note that the height of the sources was selected to be 1.48 m because this was the case with experimental data analyzed later on.)

Figure 5-1 shows the beamforming images obtained using DAS-C and MACS when the correlation between the sources is $\rho = 0.2$ and the frequency is 15 kHz. In the figures we compare the estimated signal auto-correlation levels, i.e., the diagonal of $\hat{\mathbf{P}}$, with the true signal auto-correlation levels (or true signal powers), i.e., the diagonal of $\mathbf{P}$. Let the scanning grid corresponding to the source at $(x, y, z) = (-0.20, 0.20, 1.48)$ m be denoted as l_0. Then, we also compare the modulus of the l_0^{th} rows of $\hat{\mathbf{P}}$ and $\mathbf{P}$, i.e., we compare the cross-correlation between all the scanning points and the l_0^{th} scanning point with the actual cross-correlation values. The "x" marks in the figures indicate the true source locations. The values estimated with MACS at the four source locations are also shown in the figures. It is observed that DAS-C fails to provide any clear information and suffers severely from high sidelobe levels, whereas MACS is able to distinguish the sources and estimate their signal powers successfully. Next, we increase the correlation level between the sources to $\rho = 0.8$ and show the resulting beamforming images in Figure 5-2. It is

observed that MACS is still able to resolve the sources and provide accurate estimates for both the auto- and cross-correlation levels.

In the second example of this section, we consider the use of LAMDA. The array center of LAMDA is at $(x, y, z) = (0, 0, 0)$ m and the array extends along the xy-plane. Four monopole sources are placed at $(x, y, z) = (-0.30, 0, 1.48)$ m (source #1), $(-0.10, 0, 1.48)$ m (source #2), $(0.10, 0, 1.48)$ m (source #3) and $(0.30, 0, 1.48)$ m (source #4) to resemble a line source. Line sources, for which the correlations between sources diminish with increased spatial distance, are frequently encountered in aeroacoustic applications. In this example, $\rho = 0.9$ was used. The signal powers, SNR and the number of blocks are kept the same as in the previous example. Figure 5-3 shows the beamforming images obtained using DAS-C and MACS at a frequency of 3 kHz (note that the frequency is lower compared to the previous example since LAMDA has a larger aperture and hence higher resolution than SADA). Similar observations as in the previous examples can be made here as well. MACS is able to localize the sources and estimate their auto- and cross-correlation levels accurately even when the sources are highly correlated.

In the examples above, we used the minimum description length (MDL) information criterion as described in [66] for estimating the number of sources $\hat{L}$. It was in fact empirically observed that MACS is quite insensitive to the selection of $\hat{L}$. However, choosing an $\hat{L}$ much larger than the number of sources will result in unnecessarily increased computation times. Therefore, $\hat{L}$ should be chosen only slightly larger than a rough estimate of the number of sources. Figure 5-4 shows the estimation performance of MACS with different values of $\hat{L}$ for the example with four sources arranged in a line (see Figure 5-3). It is observed that underestimating $\hat{L}$ is more harmful than overestimating it (as expected) and that errors in $\hat{L}$ do not result in drastic performance degradation. Note that the computation times for MACS were 17.2, 79.9, 126.2, and 245.1 seconds on a 32-bit personal computer with a 2.53 GHz processor and 3 Gbytes of RAM running MATLAB when $\hat{L} = 1, 3, 4$ and 6, respectively.

5.5.2 Experimental Results

Consider the experimental setup shown in Figure 4-2 C with two speakers generating coherent broadband noise. We saw in the previous chapter how DAS, DAMAS, SC-DAMAS, CMF and CLEAN-SC all failed with this example at 2 kHz (see Figure 4-17). In Figure 5-5, we show the beamforming results obtained with DAS, DAMAS, and CMF with the scanning resolution used in this chapter for a more fair comparison at 2 kHz. In Figure 5-6, the auto- and cross-correlation estimates obtained by DAS-C and MACS are shown again at 2 kHz. It is observed that MACS estimates the locations of the two sources accurately. Since the two sources are coherent, the cross-correlation between the source at $(x, y, z) = (-0.20, 0, 1.48)$ m and all the scanning points should be zero except at the source locations. MACS successfully estimates the cross-correlation between the two sources to be of approximately the same strength as shown in Figure 5-6. The resulting correlation coefficient, which is obtained by dividing the cross-correlation between the two sources to the square root of the auto-correlation of each source, is 0.96. (Note that even though the same waveform is fed to the speakers, the transmitted acoustic signals might be slightly different due to hardware disparities and hence the sources might not be perfectly coherent).

5.6 Conclusions

In this chapter, we have first presented the CMF-C algorithm, which is the extension of CMF to the correlated source case. We argued that DAMAS-C and CMF-C were impractical computation-wise even when the number of scanning points is small. Therefore, we have also presented a new beamforming approach, called MACS, for the efficient mapping of correlated acoustic signals in aeroacoustic measurements. MACS consists of basically two steps: one step requires solving a convex optimization problem, and the other step is based on the matrix singular value decomposition and has a closed-form solution. These two steps are implemented in a cyclic manner until convergence is achieved (MACS converges in about 5 iterations). Due to its cyclic

property, MACS is guaranteed to converge at least locally. It was shown via both simulations and experimental data, and by using two different types of arrays (with different aperture sizes and numbers of microphones), that MACS is able to effectively locate and estimate the auto- and cross-correlation levels between uncorrelated, partially correlated and coherent sources. The computation time of MACS was shown to be around 1 to 2 minutes with 289 scanning grid points and 2 to 4 correlated sources, respectively, using a 63-element microphone array. This is a significant improvement in terms of computational complexity over the existing deconvolution approaches for correlated sources, such as DAMAS-C and CMF-C, which are impractical for a reasonable scanning resolution with today's computing technology. Evaluation of MACS using further experimental data, especially with flow, appears to be an interesting topic that is left for future research.

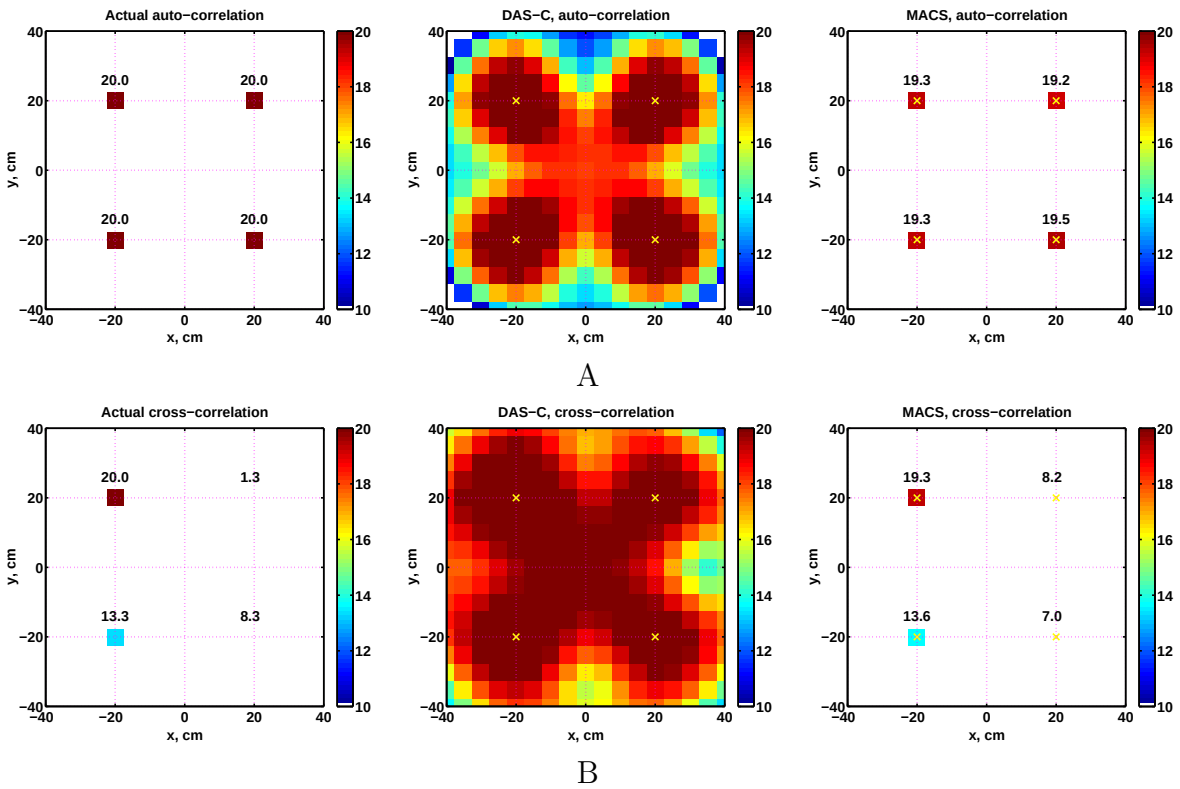

Figure 5-1. Four correlated sources with $\rho = 0.2$ at 15 kHz and using SADA. 500 FFT blocks are used and SNR = 0 dB. A) Comparison of the auto-correlation levels. B) Comparison of the cross-correlation levels between all the scanning points and the source at $(x, y, z) = (-0.2, 0.2, 1.48)$ m (the one on the upper left corner of each figure). The true signal auto- and cross-correlation levels are shown in the left most plots. In both A) and B), "x" indicates the true source locations. The MACS estimated levels are shown on the figure. All levels are in dB.

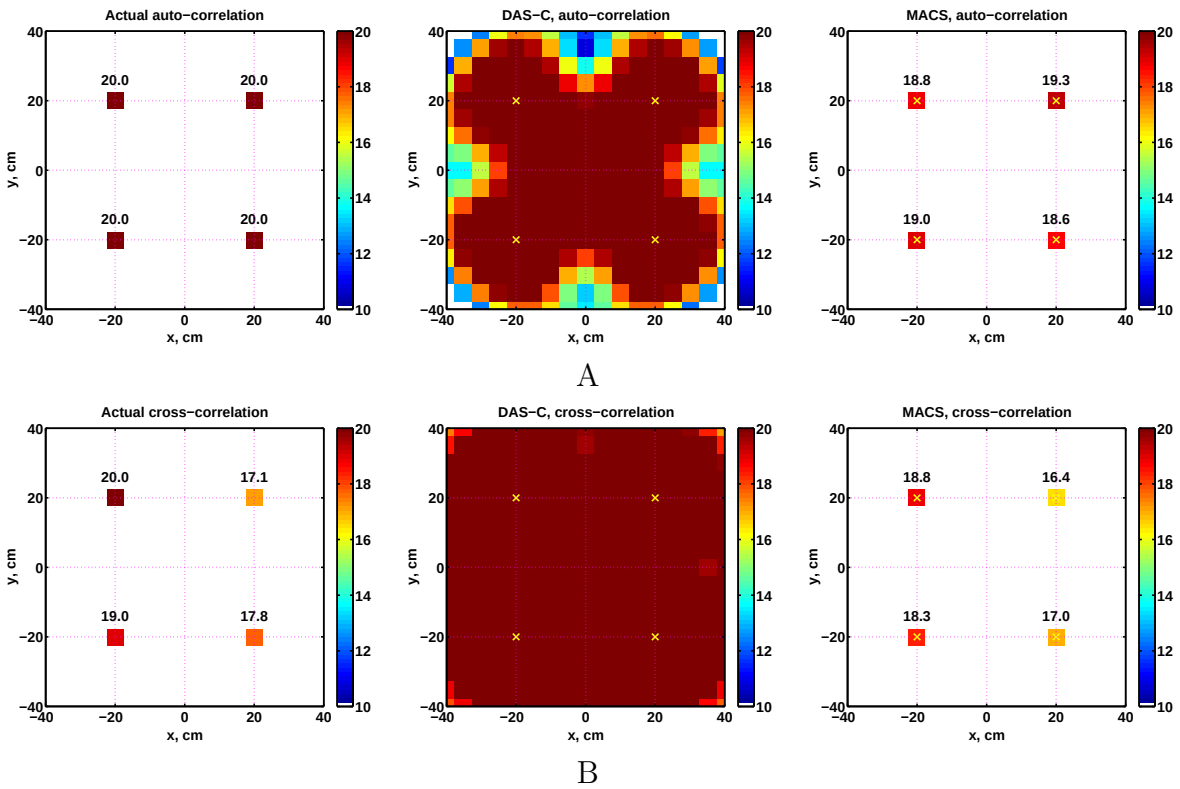

Figure 5-2. Four correlated sources with $\rho = 0.8$ at 15 kHz and using SADA. 500 FFT blocks are used and SNR = 0 dB. A) Comparison of the auto-correlation levels. B) Comparison of the cross-correlation levels between all the scanning points and the source at $(x, y, z) = (-0.2, 0.2, 1.48)$ m (the one on the upper left corner of each figure). The true signal auto- and cross-correlation levels are shown in the left most plots. In both A) and B), "x" indicates the true source locations. The MACS estimated levels are shown on the figure. All levels are in dB.

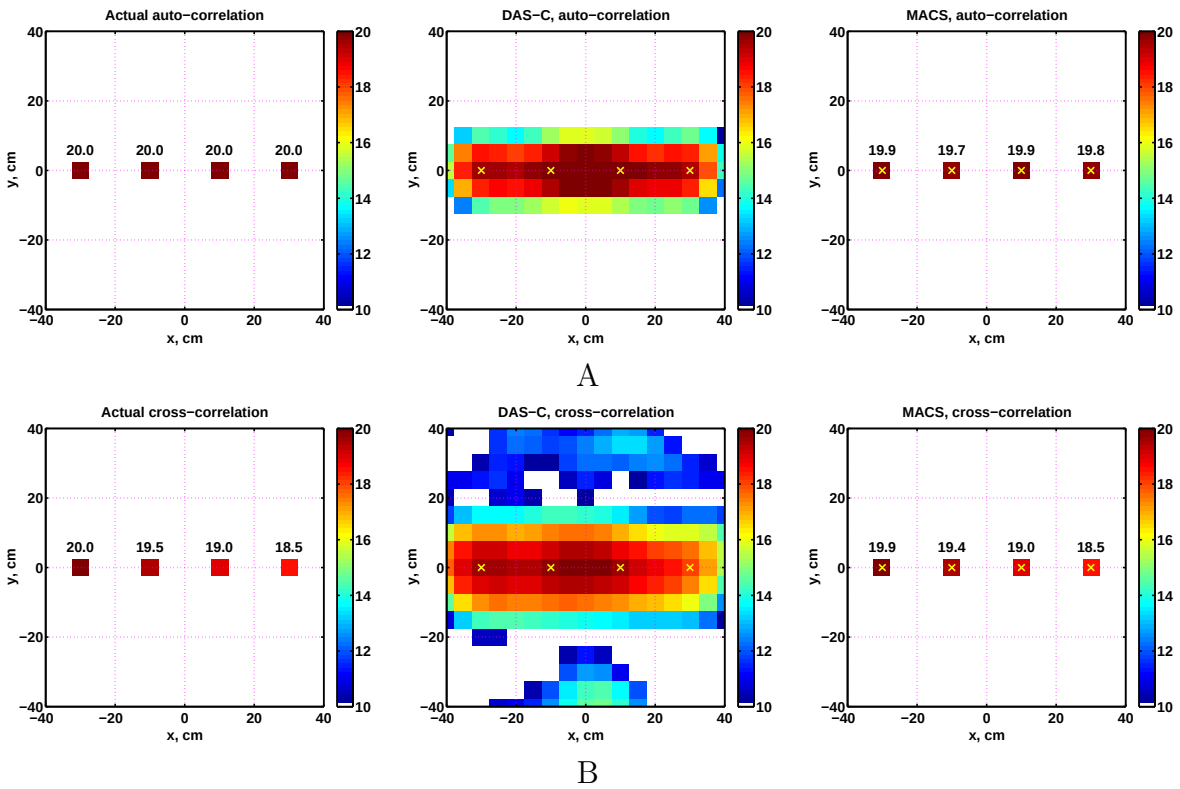

Figure 5-3. Four correlated sources with $\rho = 0.9$ at 3 kHz and using LAMDA. 500 FFT blocks are used and SNR = 0 dB. A) Comparison of the auto-correlation levels. The true signal auto-correlation levels are shown in the left most plot. B) Comparison of the cross-correlation levels between all the scanning points and the source at $(x, y, z) = (-0.3, 0, 1.48)$ m (the left-most source in each figure). In both A) and B), "x" indicates the true source locations. The MACS estimated levels are shown on the figure. All levels are in dB.

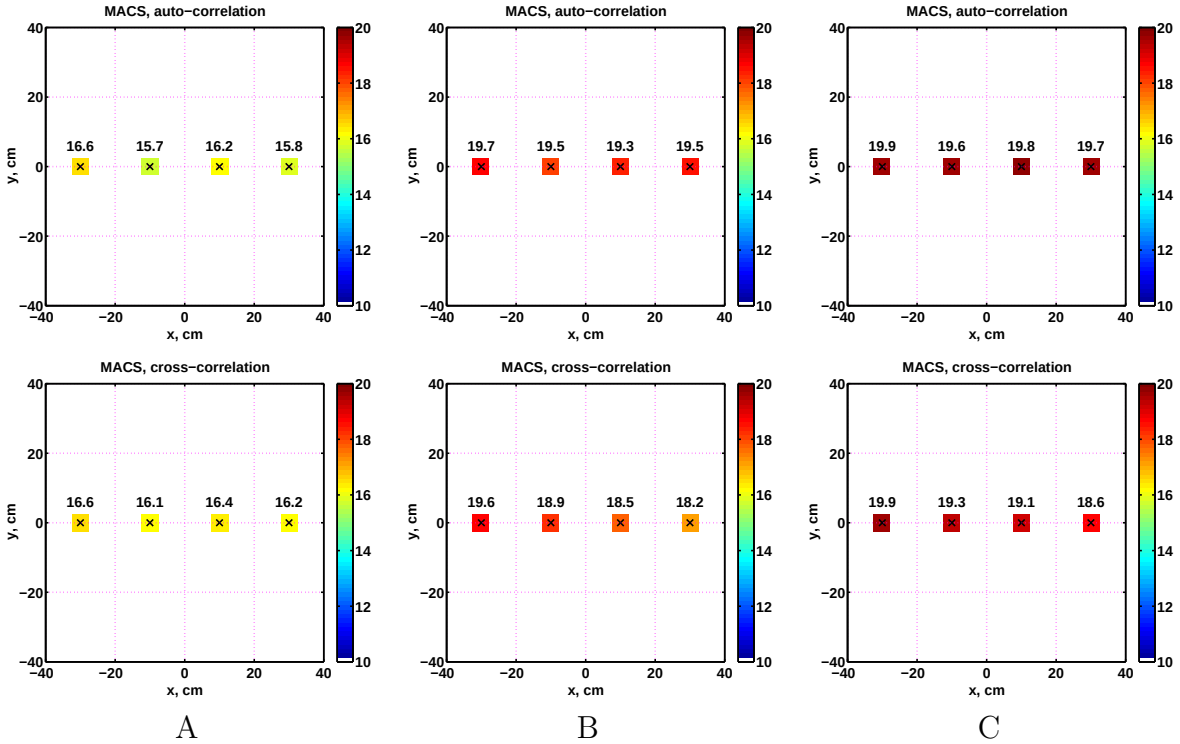

Figure 5-4. The performance of MACS when $\hat{L}$ is varied. A) $\hat{L} = 1$, B) $\hat{L} = 3$, and C) $\hat{L} = 6$. Compare with Figure 5-3.

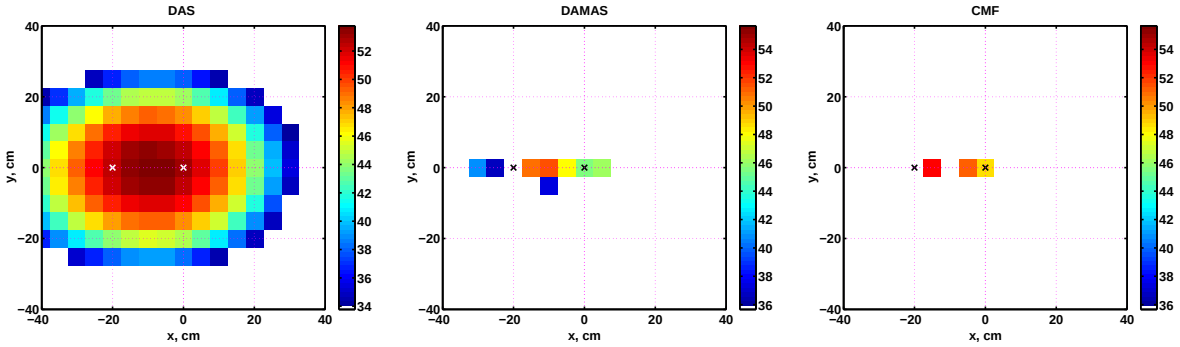

Figure 5-5. Beamforming images (levels in dB) obtained using DAS, DAMAS and CMF for two coherent sources located 0.20 m apart from each other. The true source locations are indicated by the "x" marks. Beamforming frequency is 2 kHz. The results are obtained using experimental data.

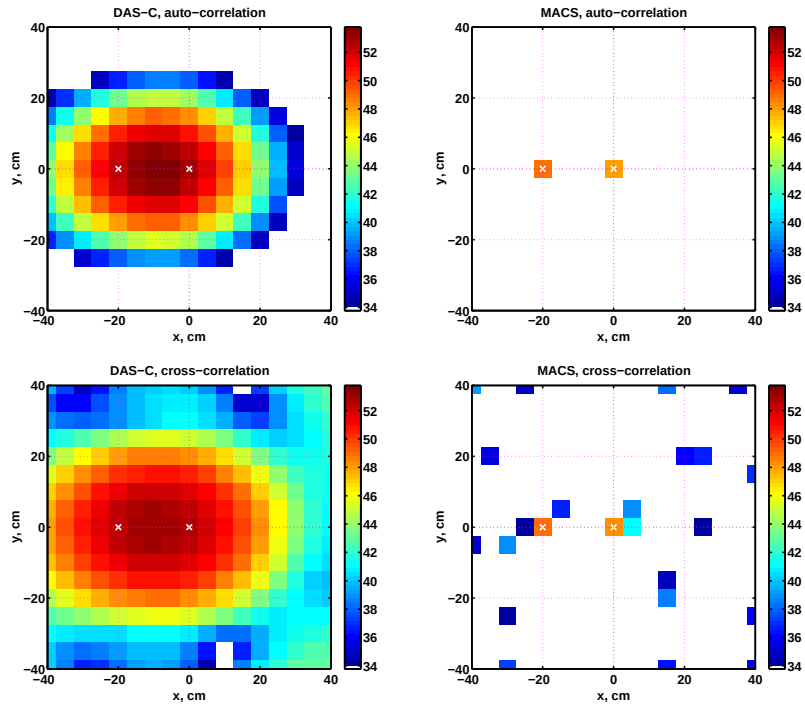

Figure 5-6. The auto-correlation at each scanning point and the cross-correlation of each scanning point with the source at $(x, y, z) = (-0.2, 0, 1.48)$ m estimated with DAS-C and MACS are shown (all levels are in dB). The setup consists of two coherent sources located 0.20 m apart from each other. The true source locations are indicated by the "x" marks. Beamforming frequency is 2 kHz. The results are obtained using experimental data.

Table 5-1. Pseudocode of MACS.

Calculate the EVD of $\hat{\mathbf{G}}$: $\hat{\mathbf{G}} = \mathbf{U}\mathbf{\Lambda}\mathbf{U}^H$
$\beta = \mathrm{tr}(\mathbf{\Lambda})$, $\xi = \sqrt{\beta L \hat{L}}$
$\mathbf{Q} = \mathbf{I}$
$\tilde{\mathbf{G}} = \mathbf{U}_{\hat{L}}(\mathbf{\Lambda}_{\hat{L}})^{1/2}$
repeat (5 times)
  Solve $\hat{\mathbf{C}} = \underset{\mathbf{C}}{\mathrm{argmin}} \ \|\tilde{\mathbf{G}}\hat{\mathbf{Q}}^H - \mathbf{A}\mathbf{C}\|_{\mathrm{F}}^2, \ \text{s.t.} \quad \|\mathbf{c}\|_1 \leq \xi,$
  Calculate the SVD of $\tilde{\mathbf{G}}^H\mathbf{A}\hat{\mathbf{C}} : \tilde{\mathbf{G}}^H\mathbf{A}\hat{\mathbf{C}} = \hat{\mathbf{U}}\tilde{\mathbf{\Sigma}}\tilde{\mathbf{U}}^H$
  $\hat{\mathbf{Q}} = \tilde{\mathbf{U}}\hat{\mathbf{U}}^H$
end repeat
$\hat{\mathbf{P}} = \hat{\mathbf{C}}\hat{\mathbf{C}}^H$

CHAPTER 6
UNCERTAINTY ANALYSIS

Uncertainty analysis answers the question of how good the results of an experiment are and, without such an analysis, it is difficult to state the confidence in the obtained estimates [67]. A standard method to calculate the output uncertainties is to propagate the uncertainties of the input variables through the data reduction equation (the equation used to estimate the quantities of interest from the measurements). The data reduction equation is a function of multiple input variables, most of which are obtained from separate measurements. Note that the uncertainties of the input variables are not necessarily uncorrelated. For instance, the DAS data reduction equation (see Eq. 2–9) contains both real- and complex-valued input variables and, in general, the real and imaginary components of the complex-valued components are correlated. As will be shown below, this leads to increased complexity in the uncertainty analysis.

Both complex multivariate and Monte-Carlo uncertainty analyses will be considered in this chapter. The multivariate analysis is based on a first-order Taylor series expansion of the quantities of interest and assumes that the perturbations are relatively small, and hence, the nonlinear terms in the Taylor series expansion are negligible. It also assumes that the output distributions are Gaussian in order to compute the confidence intervals. The multivariate uncertainty analysis differs from the classical uncertainty techniques in that it estimates the correlation of the output variables [68]. The Monte-Carlo method, on the other hand, uses assumed distributions for the input variables, which may be correlated. Random perturbations for the input variables are drawn from these distributions and the data reduction equation is evaluated using the perturbed input variables. This process is repeated until the distributions of the output variables have converged, after which the uncertainty estimate can be readily obtained from these distributions. The advantage of the multivariate analysis is that it is analytical and can estimate the uncertainties relatively quickly. However, more often than not, closed-form

expressions for the derivatives involved in the Taylor series expansion are not available or very cumbersome, and the input perturbations are not small enough to assume linearity. In addition, the Gaussian-type assumptions made when estimating the confidence intervals from the sample covariance matrices might be violated in practice. Monte-Carlo analysis provides much more flexibility in terms of designing the experiments since the data reduction equation is already implemented for the experimental analysis and embedding the perturbations of the input variables to this equation is in general straightforward.

Castellini et al. [69] study the uncertainty of the DAS beamformer for a 2D linear array and far-field noise propagation where the source locations are parameterized by angles ranging from 0 to π rather than being parameterized by 3D locations. Moreover, the analysis provided is not targeted directly for aeroacoustic applications and does not consider the uncertainties in the CSM, calibration or integrated DAS sound pressure levels. In this chapter, we specifically analyze the uncertainty of the DAS beamformer as implemented in aeroacoustic measurements [1, 2, 4, 17].

6.1 Uncertainty Analysis Techniques

As mentioned above, we consider two uncertainty analysis techniques: *i)* multivariate uncertainty analysis, which is based on a first-order Taylor series expansion, and *ii)* Monte-Carlo uncertainty analysis, which is based on assuming distributions for each input variable. We apply both multivariate and Monte-Carlo uncertainty analyses to the DAS beamformer, whereas we apply Monte-Carlo uncertainty analysis to calibration (due to the complexity of the nonlinear eigen-decomposition involved in the procedure). The following analyses consider only a single beamforming location (in particular, the lth one) and should be repeated for every point in the scanning grid, i.e., L times.

6.1.1 Multivariate Uncertainty Analysis

The classical uncertainty analysis technique estimates the uncertainty of the output variables by making use of a first-order Taylor series expansion. The uncertainties of the input variables should be sufficiently small so that the linear approximation remains valid.

The resulting sample standard deviation or the standard uncertainty of a variable, P_l in our case (see Eq. 2–9), is then computed by

$$g_{P_l} = \sqrt{\sum_{t=1}^{T'} \left(\frac{\partial P_l}{\partial V_t}\right)^2 \Gamma_{V_t,V_t} + 2\sum_{t=1}^{T'-1}\sum_{u=t+1}^{T'} \frac{\partial P_l}{\partial V_t}\frac{\partial P_l}{\partial V_u}\Gamma_{V_t,V_u}}, \tag{6–1}$$

where T' is the number of input variables, Γ_{V_t,V_t} is the standard uncertainty squared of the tth input variable, $\frac{\partial P}{\partial V_t}$ is called the sensitivity coefficient of the tth input variable, and Γ_{V_t,V_u} is the sample covariance between the tth and u^{th} input variables. Note that t and u run from 1 to T' and $t+1$ to T', respectively.

In the DAS data reduction equation, the power estimate P_l is real-valued and the input variables are complex-valued. However, Eq. 6–1 is derived for real variables and therefore the complex input variables should be separated into their real and imaginary components before being propagated through the data reduction equation [70–72]. One important reason for treating the real and imaginary parts of the input variables separately is because these components can be correlated in many applications. (Note that the second term in the square root in Eq. 6–1 accounts for the correlation between such components.) For the DAS beamformer, since only one real-valued power level is considered at a time, the multivariate and classical uncertainty analysis methods are similar [72].

Eq. 6–1 can also be written in matrix form as follows [70–72]

$$g_{P_l} = \sqrt{\mathbf{J}\boldsymbol{\Gamma}\mathbf{J}^T}, \tag{6–2}$$

where $\boldsymbol{\Gamma}$ is the $2T' \times 2T'$ real-valued and symmetric sample covariance matrix of the real and imaginary parts of all the input variables, i.e., the variables

$$\{\mathrm{Re}\{V_1\}, \ldots, \mathrm{Re}\{V_{T'}\}, \mathrm{Im}\{V_1\}, \ldots, \mathrm{Im}\{V_{T'}\}\} \tag{6–3}$$

and $\mathbf{J}$ is the $1 \times 2T'$ real-valued Jacobian matrix (a vector in our case) defined as

$$\mathbf{J} = \left[\frac{\partial P_l}{\partial \mathrm{Re}\{V_1\}}, \ldots, \frac{\partial P_l}{\partial \mathrm{Re}\{V_{T'}\}}, \frac{\partial P_l}{\partial \mathrm{Im}\{V_1\}}, \ldots, \frac{\partial P_l}{\partial \mathrm{Im}\{V_{T'}\}} \right]. \tag{6–4}$$

Consider a simple example with 2 real variables, V_1 and V_2, where V_1 and V_2 are assumed to be uncorrelated and let the output variable P_l be a function of V_1 and V_2. Then Eq. 6–1 or Eq. 6–2 becomes

$$g_{P_l} = \sqrt{\begin{bmatrix} \frac{\partial P_l}{\partial V_1} & \frac{\partial P_l}{\partial V_2} \end{bmatrix} \begin{bmatrix} \Gamma_{V_1,V_1} & 0 \\ 0 & \Gamma_{V_2,V_2} \end{bmatrix} \begin{bmatrix} \frac{\partial P_l}{\partial V_1} \\ \frac{\partial P_l}{\partial V_2} \end{bmatrix}} = \sqrt{\left(\frac{\partial P_l}{\partial V_1}\right)^2 \Gamma_{V_1,V_1} + \left(\frac{\partial P_l}{\partial V_2}\right)^2 \Gamma_{V_2,V_2}}, \tag{6–5}$$

where the squared uncertainties of the variables V_1 and V_2 are scaled by the sensitivity coefficients $\frac{\partial P_l}{\partial V_1}$ and $\frac{\partial P_l}{\partial V_2}$ squared, respectively, and summed up to generate the final uncertainty squared.

In general, 95% confidence intervals are used when reporting the uncertainty results. In order to obtain the confidence intervals, g_{P_l} should be multiplied by a coverage factor which is simply taken as 2 in our case assuming a Gaussian distribution for the univariate output variable [72]. (Note that $(P_l - \bar{P}_l)/S_{P_l}$, where $\bar{P}_l$ and S_{P_l} are the sample mean and sample standard deviation of P_l, respectively, follows the t distribution with number of Monte-Carlo trials minus one degrees of freedom. It is recommended that a coverage factor of 2 is used when the degrees of freedom is larger than 31 [67].)

6.1.2 Monte-Carlo Uncertainty Analysis

When the perturbations are relatively large (so that the linear assumption of the multivariate analysis is violated) and/or the output distributions are non-Gaussian, the multivariate method can no longer yield reliable uncertainty estimates. In addition, the sensitivity coefficients are often difficult to evaluate in closed-form. Therefore, a Monte-Carlo uncertainty analysis is preferable. In Monte-Carlo uncertainty analysis, a distribution is assumed for all of the input variables and then each variable is randomly perturbed using a perturbation value drawn from its uncertainty distribution (note that

the input variables are not necessarily uncorrelated) [67, 72]. Next, the perturbed input variables are propagated through the data reduction equation in order to obtain the perturbed output. This process is repeated until the distribution of the output variables converge (it was observed that 1000 iterations were sufficient for convergence in our examples) [68]. The resulting distribution is then used to obtain the mean, variance (covariance) and 95% confidence intervals for the quantities of interest.

6.2 Application of Uncertainty Analysis to the Delay-and-Sum Beamformer

In this section we describe how the aforementioned uncertainty analysis techniques can be applied to the DAS data reduction equation given in Eq. 2–9. Let

$$\mathbf{G} = \begin{bmatrix} G_{11} & C_{12} + jQ_{12} & \dots & C_{1M} + jQ_{1M} \\ C_{12} - jQ_{12} & G_{22} & \dots & C_{2M} + jQ_{2M} \\ \vdots & \vdots & \ddots & \vdots \\ C_{1M} - jQ_{1M} & C_{2M} - jQ_{2M} & \dots & G_{MM} \end{bmatrix}, \tag{6–6}$$

where $C_{mn} = \mathrm{Re}\{G_{mn}\}$ and $Q_{mn} = \mathrm{Im}\{G_{mn}\}$, $m \neq n$, $m, n = 1, \dots, M$. Similarly, let

$$\tilde{\mathbf{D}} = \begin{bmatrix} D_1 + jE_1 & 0 & \dots & 0 \\ 0 & D_2 + jE_2 & \dots & 0 \\ \vdots & \vdots & \ddots & \vdots \\ 0 & 0 & \dots & D_M + jE_M \end{bmatrix}, \tag{6–7}$$

where $\tilde{D}_m = D_m + jE_m$, $D_m = \mathrm{Re}\left\{\tilde{D}_m\right\}$ and $E_m = \mathrm{Im}\left\{\tilde{D}_m\right\}$, $m = 1, \dots, M$.

The input variables contained in Eq. 2–9 can be expressed as

$$\mathbf{V} = [\mathbf{V}_{\mathrm{CSM}}, \mathbf{V}_{\mathrm{Calib}}, \mathbf{V}_{\mathrm{Locs}}, V_{\mathrm{Temp}}], \tag{6–8}$$

where

$$\mathbf{V}_{\mathrm{CSM}} = [G_{11}, \dots, G_{MM}, C_{12}, \dots, C_{1M}, C_{23}, \dots, C_{M-1,M}, Q_{12}, \dots, Q_{1M}, Q_{23}, \dots, Q_{M-1,M}], \tag{6–9}$$

$$\mathbf{V}_{\text{Calib}} = [D_1, \ldots, D_M, E_1, \ldots, E_M], \tag{6–10}$$

$$\mathbf{V}_{\text{Locs}} = [x_1, \ldots, x_M, y_1, \ldots, y_M, z_1, \ldots, z_M], \tag{6–11}$$

and, finally,

$$V_{\text{Temp}} = [T]. \tag{6–12}$$

Table 6-1 lists the four categories of input variables as considered above.

The Jacobian matrix for P_l is defined as (see Eq. 6–4)

$$\mathbf{J} = \left[\underbrace{\frac{\partial P_l}{\partial G_{11}}, \ldots, \frac{\partial P_l}{\partial Q_{M-1,M}}}_{\mathbf{J}_{\text{CSM}}}, \underbrace{\frac{\partial P_l}{\partial D_1}, \ldots, \frac{\partial P_l}{\partial E_M}}_{\mathbf{J}_{\text{Calib}}}, \underbrace{\frac{\partial P_l}{\partial x_1}, \ldots, \frac{\partial P_l}{\partial z_M}}_{\mathbf{J}_{\text{Locs}}}, \underbrace{\frac{\partial P_l}{\partial T}}_{J_{\text{Temp}}} \right] \tag{6–13}$$

and therefore the 95% confidence interval for P_l is given by (see Eq. 6–2)

$$\begin{aligned} 2g_{P_l} &= 2\left(\mathbf{J}\mathbf{g}_{(\text{CSM,Calib,Locs,Temp})}\mathbf{J}^T\right)^{1/2} \\ &= 2(\mathbf{J}_{\text{CSM}}\mathbf{g}_{\text{CSM}}\mathbf{J}_{\text{CSM}}^T + \mathbf{J}_{\text{Calib}}\mathbf{g}_{\text{Calib}}\mathbf{J}_{\text{Calib}}^T \\ &+ \mathbf{J}_{\text{Locs}}\mathbf{g}_{\text{Locs}}\mathbf{J}_{\text{Locs}}^T + J_{\text{Temp}}g_{\text{Temp}}J_{\text{Temp}}^T)^{1/2}, \end{aligned} \tag{6–14}$$

where $\mathbf{g}_{(\text{CSM,Calib,Locs,Temp})}$ is the sample covariance matrix of $\mathbf{V}$ and $\mathbf{g}_{\text{CSM}}$ is the sample covariance matrix of $\mathbf{V}_{\text{CSM}}$ ($\mathbf{g}_{\text{Calib}}$, $\mathbf{g}_{\text{Locs}}$ and g_{Temp} are defined in a similar manner). (It is assumed that the CSM, calibration, microphone location and temperature errors are independent of each other.)

In order to evaluate Eq. 6–14, we need to compute the sample covariance matrices of the input variables, $\mathbf{g}_{\text{CSM}}$, $\mathbf{g}_{\text{Calib}}$, $\mathbf{g}_{\text{Locs}}$, and g_{Temp}, as well as the Jacobian matrices, $\mathbf{J}_{\text{CSM}}$, $\mathbf{J}_{\text{Calib}}$, $\mathbf{J}_{\text{Locs}}$ and J_{Temp}. We need the sample covariance matrices also for the Monte-Carlo analysis, since these will be the covariance matrices of the Gaussian distributions from which the random perturbations are drawn. The Jacobian matrices for each category of input variables, i.e., the terms in Eq. 6–13, are derived in Appendix A. When computing $\mathbf{g}_{\text{CSM}}$, we consider the random errors associated with using the finite averaging method in Eq. 2–8. The expression for each component of $\mathbf{g}_{\text{CSM}}$ is given in Table 9.1 of Bendat

and Piersol [54] for two microphones ($M = 2$). We extend this analysis to the case of M microphones, where M can be any number greater than 1, and list our findings in Table 6-2. Appendix B provides the details on how the covariances in Table 6-2 are computed. Note that when overlapping blocks are used to compute the CSMs, the number of blocks, B, should be replaced by the effective number of blocks, $\omega_1 B$, in Table 6-2, where ω_1 is used to account for the correlation between overlapping blocks. For instance, for a Hanning window with 50% or 75% overlap, $\omega_1 = 0.947$ or $\omega_1 = 0.520$, respectively [54]. The covariance matrices due to calibration and location errors are taken as diagonal matrices with the corresponding uncertainties along the diagonals.

When perturbing $\mathbf{G}$ in the Monte-Carlo uncertainty analysis, a Gaussian random vector, say $\tilde{\mathbf{V}}_{\text{CSM}}$, with covariance matrix $\mathbf{g}_{\text{CSM}}$ as given in Table 6-2 and a zero mean vector is generated every trial (Appendix C briefly discusses one way of doing this) to obtain the perturbations of each variable contained in $\mathbf{V}_{\text{CSM}}$. The perturbation values are then used to form a perturbation matrix $\mathbf{G}_{\text{p}}$ (by properly indexing the variables) and the perturbed CSM is computed as $\mathbf{G} + \mathbf{G}_{\text{p}}$. When perturbing the input variables contained in $\mathbf{V}_{\text{Calib}}$, $\mathbf{V}_{\text{Locs}}$ and V_{Temp}, i.i.d. Gaussian random variables with zero mean and given uncertainty values are generated, and these perturbations are added to the nominal values.

6.3 Numerical and Experimental Results

This section presents the uncertainty analysis of the calibration procedure and the DAS beamformer using numerical as well as experimental data. Both the individual and the cumulative effects of the input parameters are analyzed to understand the dominant sources of uncertainty. LAMDA is used for the analysis.

6.3.1 Calibration Uncertainty

As mentioned in Chapter 2, when all the assumptions are met, the array calibration procedure will provide accurate correction factors for a source near the calibration speaker location. However, in practice, many sources of uncertainty are present during calibration such as the uncertainties in the CSM and reference microphone levels. This section

will analyze the sensitivity of the calibration procedure to such errors. The calibration performance will also degrade when the calibration source is not a perfect monopole and/or there are reflections in the calibration setup. However, we do not consider such modeling errors and instead focus our attention on the uncertainty of the calibration procedure when the underlying data model is correct. (Similarly, when evaluating the uncertainty of the DAS beamformer, the data model is assumed to be correct.)

The uncertainty analysis of the calibration procedure is conducted using Monte-Carlo simulations (a Taylor series based analysis is omitted due to the complexity of the eigen-decomposition and due to the increased flexibility provided by the Monte-Carlo method). The input variables that are perturbed include the CSM, the sound pressure level of the reference microphone, and the individual microphone sensitivities (real-valued and in mV/Pa). The individual microphone sensitivities and phases are usually obtained from manufacturer specifications or from individual calibrations with respect to some high quality microphone. We assume that a frequency independent sensitivity value is used for all the microphones with a nominal value of 30 mV/Pa (which is the sensitivity used with the Panasonic WM-61A microphones at the UFAFF), and we assume that the nominal phase of each microphone is 0°. The SNR is set to 25 dB in the calibration setup, where SNR is defined as $10\log_{10}(\sum_{b=1}^{B}\|\mathbf{a}_{\text{cal}}s_{\text{cal}}(b)\|_2^2) - 10\log_{10}(\sum_{b=1}^{B}\|\mathbf{e}(b)\|_2^2)$. In order to model the uncertainties in the calibration procedure, we simulate microphone pressure measurements from an ideal monopole source located at (0, 0, 1.48) m. The array center is located at (0, 0, 0) m (nominally). The sampling frequency $f_s = 65,536$ Hz and the block length $H = 4096$ (see Section 2.1). All B values shown represent effective number of blocks. The frequency is set at 5 kHz, and 1000 Monte-Carlo trials have been implemented. Due to the observation that the output distributions are Gaussian, 2 times the sample standard deviation is considered as the uncertainty in the plots of this section.

First, we consider the effects of perturbing the individual microphone sensitivities while keeping the other input variables at their nominal values. As observed from Figure

6-1, there is a one-to-one relationship between the relative uncertainties in the microphone sensitivities and the magnitude of the calibration factors. In the figures presented in this section, the average (over all microphones) uncertainty in the magnitude and phase of the microphone correction factors are plotted. Note that the averages are taken after finding the uncertainty of each individual microphone. One important note here is that a higher uncertainty is not necessarily detrimental since the goal of calibration is to correct for such errors. Therefore, we find it more appropriate to consider the effects of microphone sensitivity and phase errors, temperature errors and microphone location errors in the following sections where we analyze the overall DAS uncertainty.

The effect of the number of blocks, B, on the uncertainty of the calibration procedure can be observed from Figure 6-2, where all the other variables are kept at their nominal values. There is approximately a one-to-two ratio in the uncertainties as expected since the error in the CSM drops with $\sqrt{B}$. Although the uncertainties in the magnitude appears to be large (10%) for a conventional B such as 1000, the final effect on the DAS estimate is within reasonable limits as will be shown below. For instance, with a nominal sensitivity of 30 mV/Pa, a positive 10% perturbation in all the microphone sensitivities will yield $|20\log_{10}(30/33)| = 0.83$ dB difference in the source levels. We observe that the phase uncertainty is relatively low even for small B.

Next, we examine the uncertainties in the reference microphone sound pressure levels only in Figure 6-3. Such errors might rise from the imperfect calibrations of the reference microphone. As expected, there is a one-to-one relation between the calibration uncertainty and the reference microphone level uncertainty. The phase is not affected since the second stage of calibration is for magnitude correction only.

Finally, in Figure 6-4, where the uncertainties in the microphone sensitivities and reference microphone level are set to 10% and $B = 1000$, the uncertainty of calibration with varying frequency is plotted. It is observed that the uncertainty is independent of frequency. This is because the microphone sensitivity and reference microphone level

uncertainties are assumed to be frequency-independent in our analysis. (Note that in practice, the uncertainties might vary somewhat with frequency, in which case the calibration uncertainty will also vary with frequency.) In the next section, we will see that when the microphone locations or the temperature are perturbed, the frequency will be important since these perturbations will be multiplied by the wavenumber.

Based on the above observations, the accurate calibration of the reference microphone is very important since this will determine the array power estimates directly. Moreover, it appears that during calibration, it is beneficial to acquire data for as long as possible. As mentioned above, the uncertainties in calibration due to microphone sensitivity and phase errors, temperature errors and microphone location errors are better analyzed within the context of beamforming.

6.3.2 Delay-and-Sum Beamformer Uncertainty

Unless otherwise stated, in all the simulations in this section, a monopole source with 50 dB signal power (power is defined at the nominal array center) is simulated at (0, 0, 1.48) m where the array center is nominally located at (0, 0, 0) m as in the calibration case. (Note that the calibration speaker at UFAFF produces approximately 50 dB signal power at the array center.) 1000 Monte-Carlo trials have been implemented and the frequency is set at 5 kHz. The SNR is 25 dB. The scanning region is set from -0.50 m to 0.50 m with 0.02 m resolution in both the x and y directions. The room temperature is $T_0 = 293$ K and the nominal sound speed is 343 m/s.

6.3.2.1 Comparison of Multivariate and Monte-Carlo Analyses

In this section we show that the multivariate and Monte-Carlo uncertainty analysis of the DAS beamformer yield consistent results when the perturbations are relatively low and that the two methods differ when the perturbations become larger. We consider the perturbations in the calibration factors and the microphone locations, and similar conclusions can be made when the CSM and microphone correction factors are perturbed.

In order to analyze the effects of the calibration uncertainty on the DAS estimates, we perturb $\tilde{\mathbf{D}}$ (see Eq. 2–9) using the values obtained in Section 6.3.1 as a guideline. The uncertainties in the real and imaginary components of the calibration factors can be found by either using a simple Monte-Carlo analysis or using multivariate uncertainty propagation given the uncertainties in magnitude and phase [72]. The resulting sample covariance matrix from this procedure is then used to generate (possibly correlated) perturbation values for D_m and E_m at each Monte-Carlo iteration, where $m = 1, \ldots, M$. Figure 6-5 shows the difference in dB between the true source power, P_0, and $P_0 + 2\sigma_l$, where σ_l is the sample standard deviation estimated via each of the two methods at the lth scanning point. The results of the two methods match well and it was observed that this is the case even for large perturbation values in microphone calibration factors (results not shown).

Next, we consider two perturbation settings for the microphone locations. The microphone locations are perturbed with i.i.d. Gaussian random variables of standard deviations 1 mm and 10 mm in Figures 6-6 A and B, and Figures 6-6 C and D, respectively. It is observed that the two uncertainty analysis methods give different results when the perturbations are larger. Note that 1 mm and 10 mm perturbations translate into relative uncertainties of 0.2% and 2.3%, respectively, in terms of microphone to source distances.

As the uncertainties in the input variables increase, the first-order linear approximation with the Taylor series does not suffice to model the overall uncertainty due to the nonlinearities. To increase the accuracy of this method, more terms need to be considered in the Taylor series expansion [68]. However, the algebra can quickly become cumbersome for Eq. 2–9. Even if the Taylor series expansion involved as many terms as needed, when the resulting distributions are not Gaussian, the standard deviation estimates of the multivariate method cannot be used to obtain 95% confidence intervals. These limitations and some other reasonings provided below make Monte-Carlo analysis a better candidate for analyzing the DAS beamformer uncertainty.

6.3.2.2 Uncertainty Analysis with Simulations

This section considers the uncertainty of the DAS beamformer using Monte-Carlo simulations. We consider the uncertainties in microphone sensitivity and phase, microphone location, array broadband distance, temperature and CSM. In the multivariate uncertainty method, the calibration effects had to be analyzed through $\tilde{\mathbf{D}}$. However, in the Monte-Carlo method, $\tilde{\mathbf{D}}$ will be estimated from calibration, which is done at each Monte-Carlo iteration using the perturbed inputs, and directly substituted in the data reduction equation. In the Monte-Carlo method, we estimate the distribution of the DAS power estimates at each scanning point and then obtain the 95% confidence intervals and mean values. Then, these values are converted into dB. The reason for showing 95% confidence intervals instead of sample standard deviations is that the resulting distributions are in general asymmetrical about their mean values. For instance, for a scanning point where the DAS estimate is relatively low, since the power estimate is constrained to be positive, ± 2 times the standard deviation cannot be used to obtain the confidence intervals when the mean is less than twice the standard deviation. The 95% confidence intervals are therefore best estimated from the distributions and standard deviations might be insufficient in modeling the uncertainties.

First, we investigate the microphone location uncertainty in detail while keeping the other input variables at their nominal values. Figure 6-7 and Figure 6-8 show the 95% confidence intervals at each scanning point when the x, y and z components of the microphone locations are perturbed using i.i.d. Gaussian random variables with zero means and standard deviations of $\sigma_{\text{Locs}} = 10$ mm and $\sigma_{\text{Locs}} = 1$ mm, respectively. These perturbation values can be normalized by the wavelength (at 5 kHz) to obtain dimensionless values of 0.146 (for 10 mm) and 0.015 (for 1 mm). Note that calibration is not applied in these plots. The 3D plots (see, e.g., Figure 6-7 A) show the mean, and the upper and lower limits of the 95% confidence intervals at each scanning location. The true source location and power are indicated with the dashed line and the dot at

its tip, respectively. The 2D plots (see, e.g., Figure 6-7 B), on the other hand, show two slices from the 3D plots taken at $x = 0$ m and $x = 0.06$ m. Note that in the 2D plots, the confidence intervals in the region from $y = 0.2$ m to 0.5 m are omitted since they resemble closely the confidence intervals in the region from $y = -0.5$ m to 0.2 m. Instead, a zoomed in view of the main beam, which is of relatively more interest, is provided (the nominal curve is omitted in the zoomed in plots). One important observation that can be made from Figure 6-7 is that the power estimates are biased downwards with respect to the nominal value. Appendix D provides an explanation for this rather non-intuitive phenomenon. To further elaborate on the bias issue, we show the peak location of the DAS beamforming image at each Monte-Carlo trial when $\sigma_{\text{Locs}} = 10$ mm together with the histogram of the peak location in Figures 6-9 A and 6-9 B. Note that the DAS peak location exhibits a discrete pattern due to the finite scanning resolution which is set to 5 mm in Figure 6-9 A. The mean of the peak locations over all the trials is indicated with the empty circle. It is observed that the DAS peak occurs either at the true source location or in its vicinity and that the mean location of the peaks coincides with the true source location. However, even when the peak appears at the true source location, the estimated power value is less than the nominal value (as discussed in Appendix D). This can also be observed from Figure 6-9 C where slices from the beamforming map at x = 0 m from 4 different samples are shown together with the nominal value. We observe that there are large fluctuations at almost every scanning point due to the location errors, consistent with the plots in Figure 6-7.

As observed above, microphone location errors can cause significant problems if not accounted for. Since calibration is specifically designed for such errors, we expect it to improve the results. In Figure 6-10, we again show the 95% confidence intervals at each scanning point but now with calibration applied. It is observed that calibration greatly reduces the variations of the DAS power estimates due to location errors. In Figure 6-9D) is shown that the power estimates from trial-to-trial now line up nicely as opposed to

Figure 6-9 C. When finding the calibration factors, we assumed that all the input variables except the microphone locations are at their nominal values.

To analyze the performance of the calibration in the presence of sources at different locations than the calibration speaker, we consider a scenario where two monopole sources of equal strength (50 dB) are placed at $(0, 0, 1.48)$ m and $(0, -0.20, 1.48)$ m. In Figures 6-11 and 6-12, the 95% confidence intervals are shown when calibration is not applied and when calibration is applied, respectively. Similar observations to the single source case can be made. It seems that although the second source is not at the same location as the calibration speaker, calibration still helps to reduce the uncertainties.

The application of calibration thus seems essential when we anticipate errors in our location measurements. Even though the location errors of the microphones on the array plane, i.e., in the x and y directions, can be measured very accurately, the non-uniformity of the array surface can result in unknown location errors. In the examples considered above, we assumed that the temperature was the same in the calibration and test data. However, in the presence of flow, the non-uniformity of temperature in the test section will cause sound speed differences in the calibration and test cases. Furthermore, in practice, there is a certain uncertainty associated with the array broadband distance, especially with complex test models.

Note that in the examples that follow, we only show the 2D slices from the beamforming images since they appear to be more informative than the 3D ones when the confidence intervals are relatively small.

To represent the uncertainty in the model to array distance, we perturb the array broadband distance together with the array microphone locations, and apply calibration as before. Figures 6-13 A and 6-13 B show the 95% confidence intervals when the relative uncertainties in the array broadband distance are set to 2.5% and 5%, respectively. Note that in our case, these correspond to net uncertainties of 0.04 m and 0.07 m. Keeping in mind that the nominal broadband distance of the source is 1.48 m, such errors might be

realizable in practice, especially when testing models with complex geometries. We also analyze the deterministic error in the estimated power levels when the array broadband distance is varied. Figure 6-14 shows the power estimated at $(x, y) = (0, 0)$ m when the array broadband distance is varied from 1.1 m to 1.9 m with increments of 0.5 mm. It is observed that the estimated source levels exhibit a concave behavior with a peak at the true source height.

In Figure 6-15, we analyze the 95% confidence intervals when the block size B used in computing the CSM is varied and the other variables are kept at their nominal values. The CSM of the calibration is also perturbed assuming that the block size of calibration was 1000. We observe that $B = 1000$ case reduces the uncertainty by about 0.5 dB compared to the $B = 200$ case.

Figure 6-16 and Figure 6-17 show the 95% confidence intervals when the individual microphone sensitivities and phases are perturbed. It is assumed that the microphone sensitivities and phase values remain the same during calibration and testing. We observe that the uncertainties are somewhat large for 15% relative uncertainty in the microphone sensitivities and that when the calibration input variables are at their nominal values, the phase errors are corrected accurately.

Figure 6-18 shows the 95% confidence intervals when the temperature is perturbed. In practice, the errors in temperature will be negligible during calibration due to the absence of flow. However, during model testing, the temperature uncertainty could be significant. Here we consider 0.1° C (Figure 6-18 A) and 3° C (Figure 6-18 B) uncertainty in temperature during testing and 0.1° C uncertainty during calibration. It appears that the beamforming procedure is quite insensitive to temperature uncertainties provided that calibration is applied. Note that a 3° C uncertainty in temperature will cause a relative perturbation of 0.5% in sound speed. We emphasize that the temperature uncertainty has only been considered through its effect on the sound speed. In practice, microphone

transfer functions as well as microphone locations (due to the expansion/contraction of the array plate) could be affected by temperature, resulting in larger uncertainties.

Finally, in Figure 6-19 we consider the overall uncertainty when the microphone location uncertainties are 10 mm, relative array broadband distance uncertainty is 5%, temperature uncertainty is 3° C for testing and 0.1° C for calibration, CSM uncertainty is calculated using 1000 blocks for both calibration and testing, and microphone sensitivity and phase uncertainties are 15% and 10°, respectively. It is observed that the 95% confidence interval at the source location is around [-0.84, 0.45] dB of the mean value.

6.3.2.3 Uncertainty Analysis with Experimental Data

The Monte-Carlo method is now demonstrated on experimental data taken at the UFAFF using LAMDA with the purpose of investigating the uncertainty in the integrated DAS levels (see Section 4.4 for the description of integrated levels). In the Monte-Carlo trials, the psf is calculated at each iteration with the perturbed values when calculating the normalization factor for DAS.

The first test setup consists of a single speaker placed at $(0, 0, 1.48)$ m similar to the scenario considered earlier with simulations. The data analysis parameters are as follows: a Hanning window with 75% overlap has been applied to blocks of size 4096 samples, the sampling frequency is 65,536 Hz and the data acquisition time is 15 seconds resulting in 498 effective blocks and a frequency resolution of 16 Hz. The scanning region extends from -0.50 m to 0.50 m with a resolution of 0.02 m in both the x and y directions. The beamforming map at 2 kHz is shown in Figure 6-20 A. 1000 Monte-Carlo trials have been run and the resulting 95% confidence intervals of the integrated DAS levels versus frequency have been plotted in Figure 6-20 B for a frequency range of 1 kHz to 10 kHz. In this figure, the uncertainties for the CSM are calculated for an effective block size of 498 for testing and 1000 for calibration, the uncertainties for individual microphone sensitivities and phases are set to 15% and 15 degrees, respectively, the temperature uncertainty is set to 1% for testing and 0.1% for calibration, the microphone location

uncertainties in all the x, y and z directions are set to 10 mm, and the array broadband distance uncertainty is set to 2.5%. (10 mm standard deviation in microphone locations corresponds to dimensionless perturbations of 0.029 and 0.292 at 1 kHz and 10 kHz, respectively, when normalized by the wavelength). The uncertainties are defined with respect to the assumed nominal values and with experimental data, the "nominal" values might not be identical to the unknown true values. It is observed that the estimated levels are within ±0.5 dB of the mean value.

As a final case, we analyze the uncertainty in the integrated DAS levels of the NACA 63-215 Mod B airfoil [47, 59]. (This is the same model considered in Section 4.10.) The beamforming image of the airfoil at 2.5 kHz is shown in Figure 6-21 A, where two locations with dominant noise can be identified. Note that in the beamforming map, the scanning region extends from -0.5 m to 0.5 m in the x direction and from -0.6 m to 0.6 m in the y direction with a common resolution of 0.02 m, and the model is at a broadband distance of 1.30 m with respect to the array plane. The Mach number is 0.17. Due to the presence of flow during the airfoil testing, DR is applied, i.e., the diagonal of $\mathbf{G}$ is removed in the DAS data reduction equation (see Section 3.2). Moreover, SLC has also been employed [1, 55]. The data acquisition parameters are the same as in Section 4.10 and repeated here for completeness. The data acquisition time was 5 seconds, sampling frequency was 65,536 Hz and the block length was 2048 samples (frequency resolution of 32 Hz). A Hanning window with 75% overlap has been employed leading to 331 effective averages [47]. The resulting uncertainties in the integrated levels are shown in Figure 6-21 B where the input uncertainties are set to the same values used in the previous example. (10 mm standard deviation in microphone locations corresponds to dimensionless perturbations of 0.022 and 0.073 at 0.75 kHz and 2.5 kHz, respectively, when normalized by the wavelength). We observe that the estimated levels are within ±1 dB of the mean values over a frequency range of 0.75 kHz to 2.5 kHz. (Note that the uncertainties due to shear layer corrections have not been considered.)

6.4 Conclusions

This chapter has presented the uncertainty analysis of the array calibration technique and the DAS beamformer. It was shown that the DAS uncertainty obtained from the multivariate and Monte-Carlo methods are similar when the perturbations are relatively small. However, when the component uncertainties are relatively large, the two methods differ due to the breakdown of the first-order assumption of the multivariate technique. It was also shown that the Monte-Carlo method is simpler to implement and provides more flexibility in terms of analyzing the DAS data reduction equation along with calibration. However, the Monte-Carlo method requires approximately 4 times more computation than the analytic multivariate method for 1000 iterations with the scanning resolutions implemented in the numerical examples above.

The calibration procedure was shown to be essential when errors are expected in microphone frequency responses, microphone locations and/or temperature measurements. With calibration, the DAS beamformer was shown to be affected mostly by the uncertainty in the array broadband distance followed by the uncertainties in the CSM and individual microphone sensitivities. In addition, the uncertainty in the integrated DAS levels of experimental data was also considered. In particular, the 95% confidence intervals were found to be around ± 0.5 dB for a single monopole source also used for calibration, whereas with the NACA 63-215 Mod B airfoil model, the 95% confidence intervals of the integrated levels were found to be larger than ± 1 dB. It should be noted that if the conditions of calibration and testing are significantly different (for instance, if the microphone transfer functions change from calibration to testing), the calibration procedure will be less effective. Therefore, the uncertainties and the confidence intervals provided in this chapter could be considered as lower bounds on the errors that will be encountered in practice.

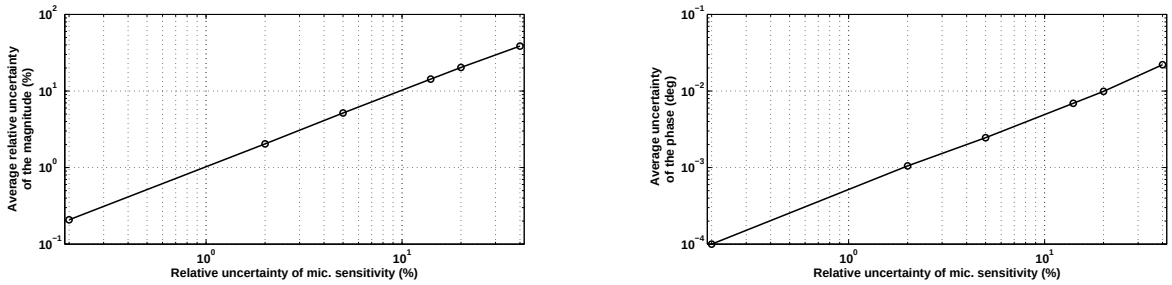

A B

Figure 6-1. The average (over all microphones) uncertainty of the A) magnitude and B) phase terms of the microphone correction factors when the individual microphone sensitivities are perturbed. Frequency is 5 kHz.

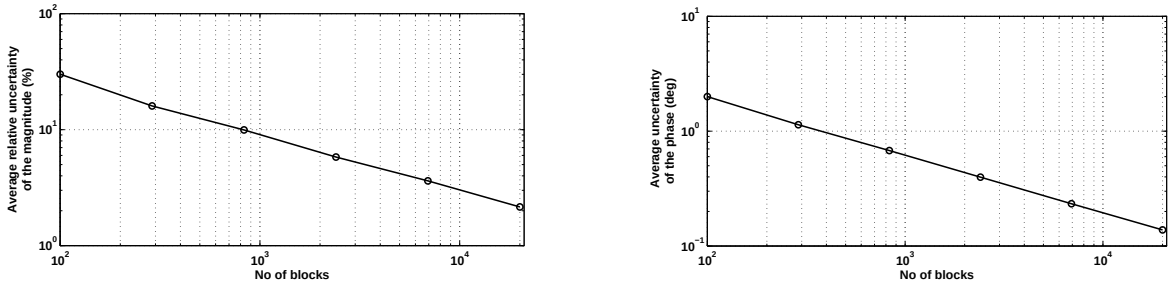

A B

Figure 6-2. The average (over all microphones) uncertainty of the A) magnitude and B) phase terms of the microphone correction factors when the CSM is perturbed. Frequency is 5 kHz.

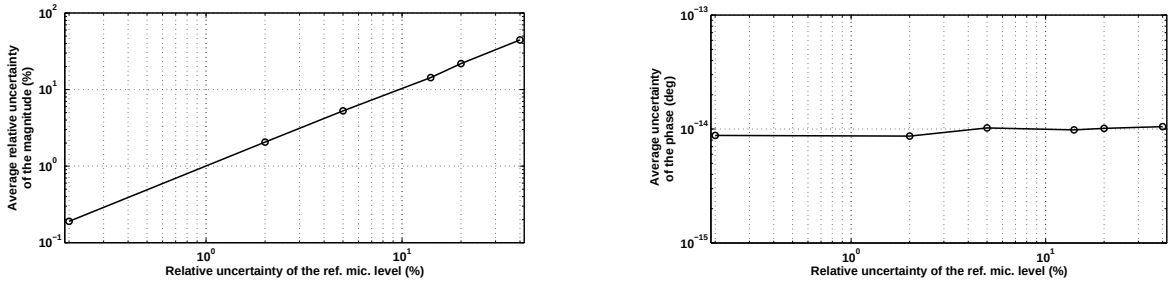

A B

Figure 6-3. The average (over all microphones) uncertainty of the A) magnitude and B) phase terms of the microphone correction factors when the reference microphone level is perturbed. Frequency is 5 kHz.

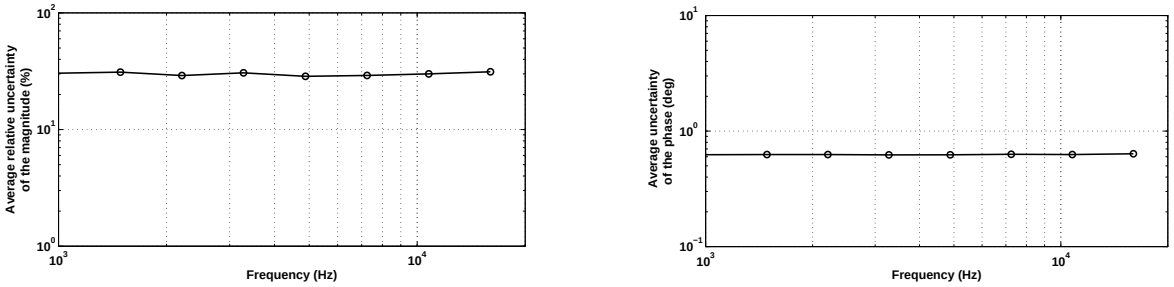

A B

Figure 6-4. The average (over all microphones) uncertainty of the A) magnitude and B) phase terms of the microphone correction factors for varying frequency where the relative uncertainty in microphone sensitivities and reference microphone level are 10% and the number of blocks is 1000.

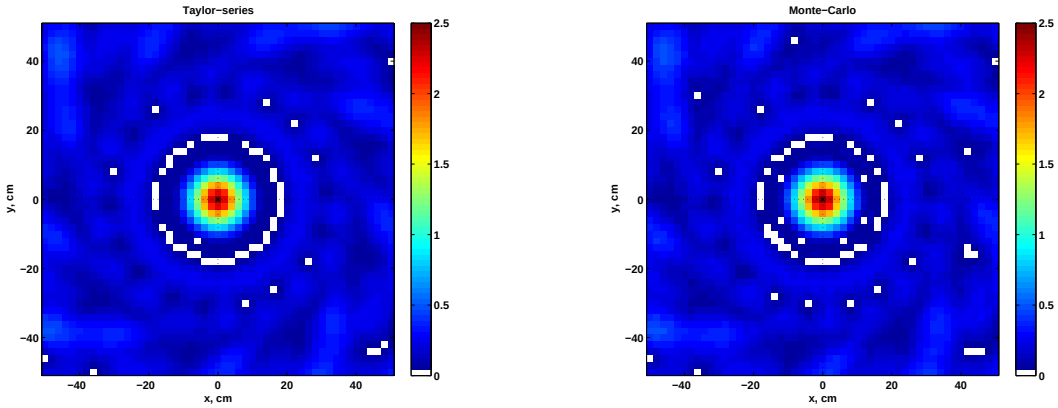

A B

Figure 6-5. Comparison of A) multivariate and B) Monte-Carlo methods when microphone correction factors are perturbed. The difference in dB between the true source power, P_0, and $P_0 + 2\sigma_l$, where σ_l is the sample standard deviation estimated via each of the two methods at the lth scanning point. The relative uncertainty of the microphone correction factor magnitude is 5% and the uncertainty of the microphone correction factor phase is 1°. Frequency is 5 kHz.

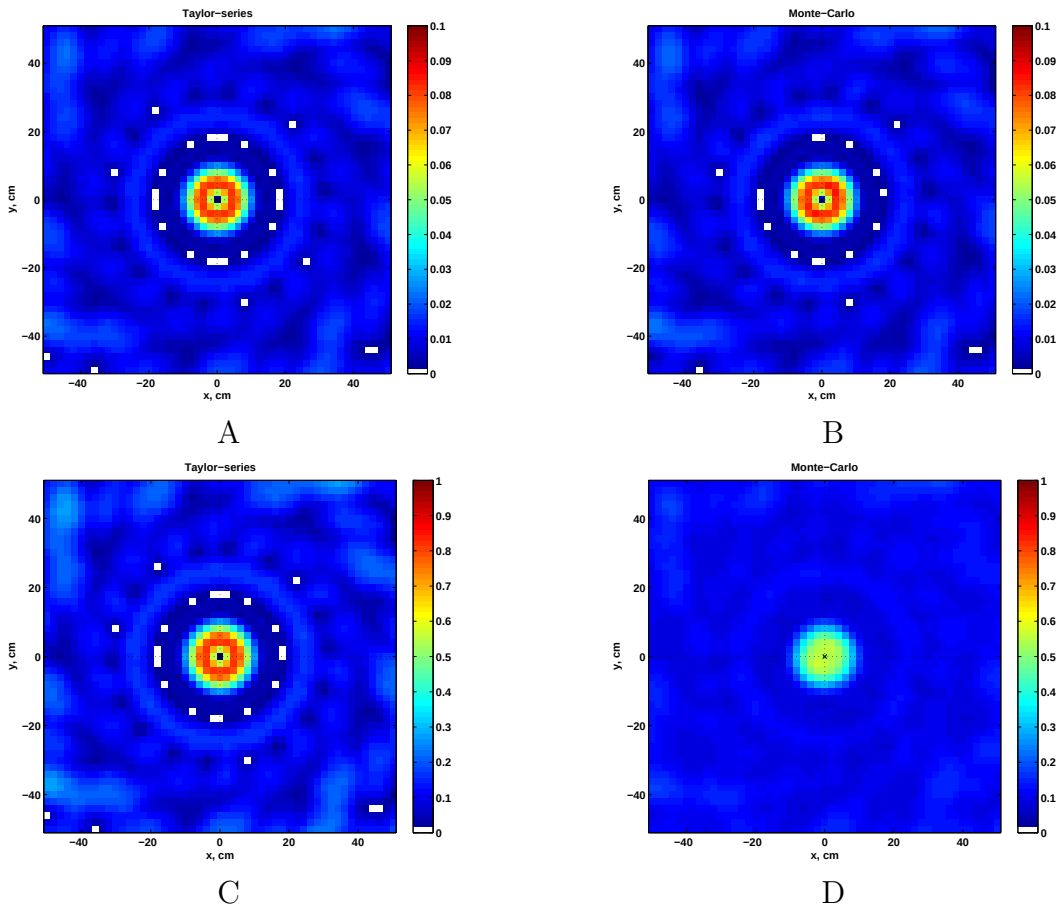

Figure 6-6. Comparison of A) and C) multivariate and B) and D) Monte-Carlo methods when microphone locations are perturbed. The difference in dB between the true source power, P_0, and $P_0 + 2\sigma_l$, where σ_l is the sample standard deviation estimated via each of the two methods at the lth scanning point. The microphone locations are perturbed with i.i.d. Gaussian random variables of standard deviations 1 mm in A) and B), and 10 mm in C) and D). Frequency is 5 kHz.

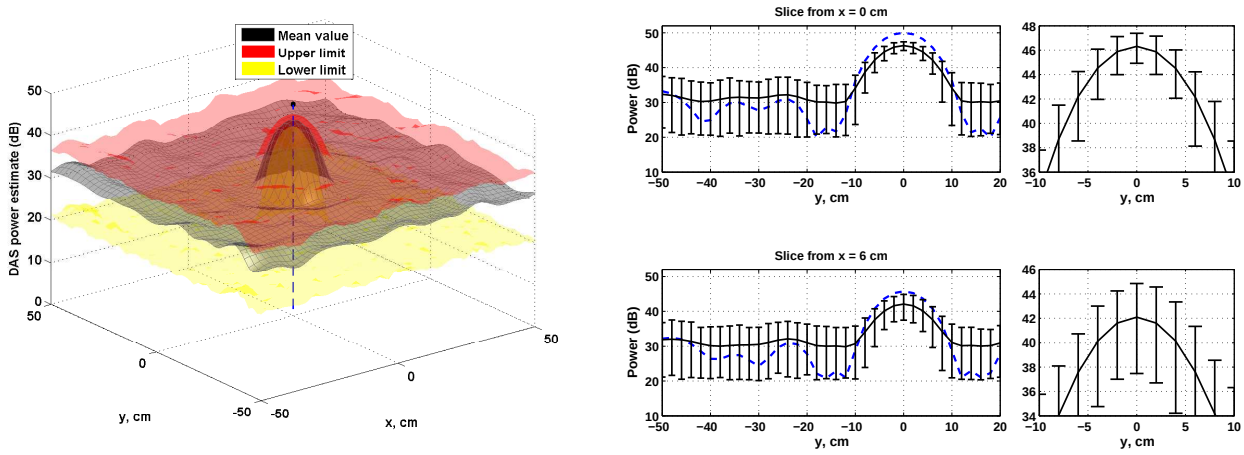

A B

Figure 6-7. Microphone locations are perturbed with a standard deviation of 10 mm. A) 3D plot showing the mean and the 95% confidence intervals. The true source location and power are indicated with the dashed line and the dot at its tip, respectively. B) Two slices from the plot in A) to further illustrate the 95% confidence intervals. The black solid line and the blue dashed line indicate the mean values and the nominal values, respectively. A zoomed in view of the main beam region is also provided. Frequency is 5 kHz.

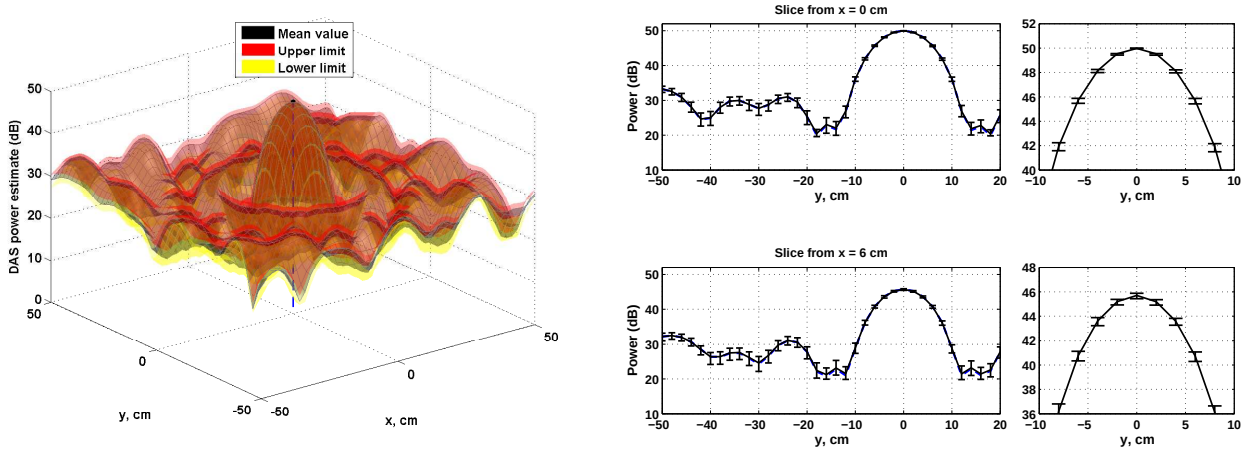

A B

Figure 6-8. Microphone locations are perturbed with a standard deviation of 1 mm. A) 3D plot showing the mean and the 95% confidence intervals. The true source location and power are indicated with the dashed line and the dot at its tip, respectively. B) Two slices from the plot in A) to further illustrate the 95% confidence intervals. The black solid line and the blue dashed line indicate the mean values and the nominal values, respectively. A zoomed in view of the main beam region is also provided. The nominal and the mean values are indistinguishable at most y values. Frequency is 5 kHz.

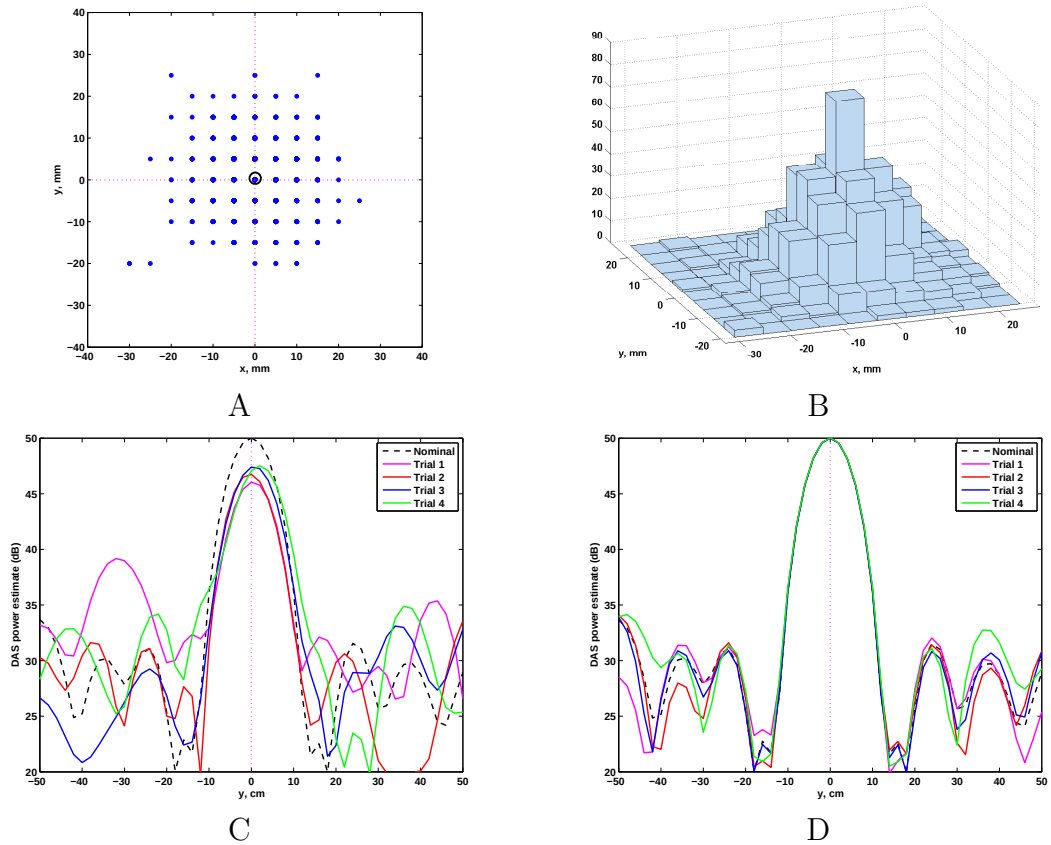

Figure 6-9. Microphone locations are perturbed with a standard deviation of 10 mm. A) The location of the DAS peak estimate at each Monte-Carlo trial is marked with a dot and the mean location of the peaks is marked with the empty circle. B) The histogram of the locations of the peaks. C)&D) The DAS power estimates at 4 arbitrary trials together with the nominal estimate. No calibration is applied in A)-C) and calibration is applied in D). Slices from the beamforming images at $x = 0$ m are shown in C) and D). Note that the units in A) and B) are in mm. Frequency is 5 kHz.

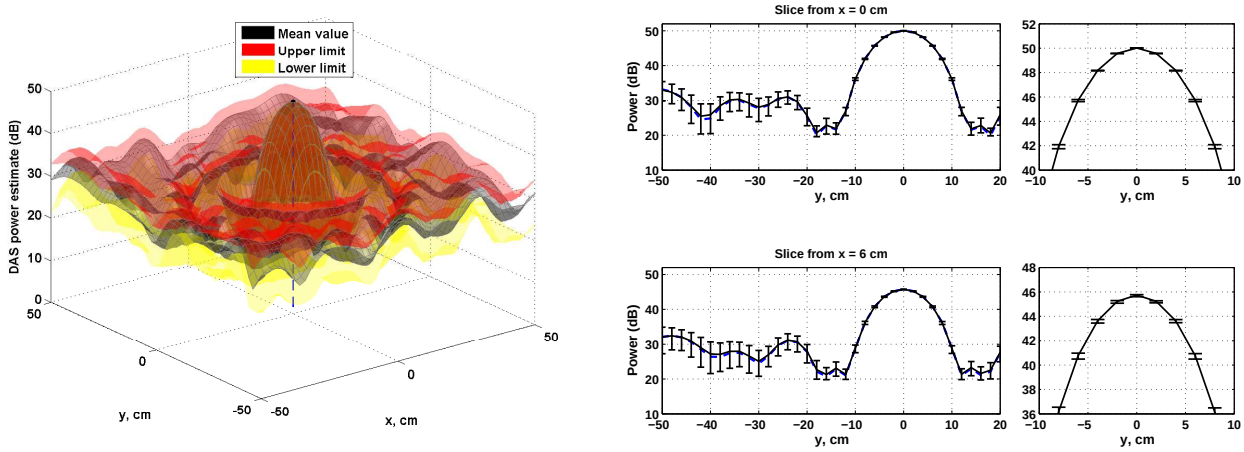

A B

Figure 6-10. Microphone locations are perturbed with a standard deviation of 10 mm and calibration is applied. A) 3D plot showing the mean and the 95% confidence intervals. The true source location and power are indicated with the dashed line and the dot at its tip, respectively. B) Two slices from the plot in A) to further illustrate the 95% confidence intervals. The black solid line and the blue dashed line indicate the mean values and the nominal values, respectively. A zoomed in view of the main beam region is also provided. The nominal and the mean values are indistinguishable at most y values. Frequency is 5 kHz.

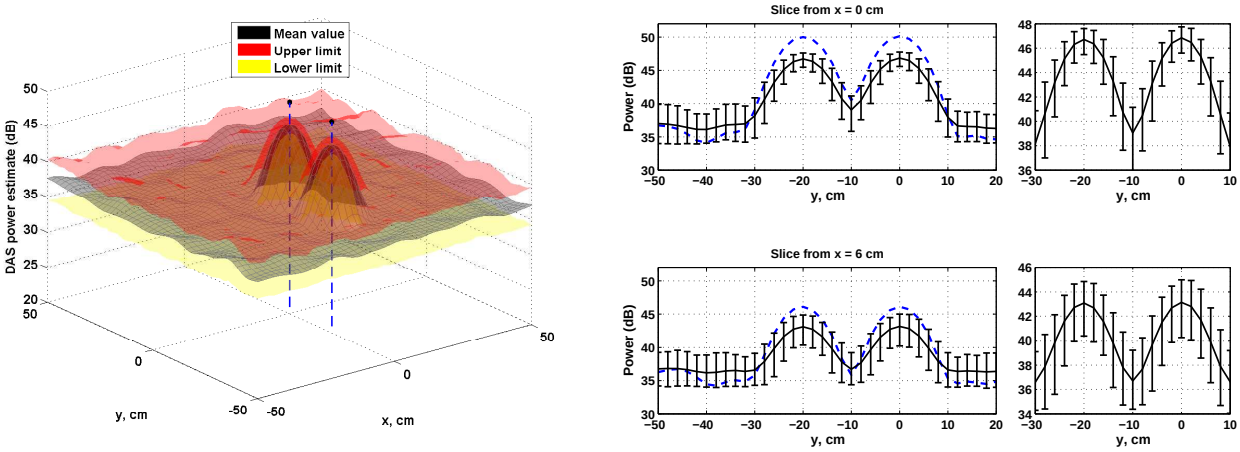

A B

Figure 6-11. Two sources are placed at (0, 0, 1.48) m and (0, -0.20, 1.48) m with equal strengths of 50 dB. Microphone locations are perturbed with a standard deviation of 10 mm and calibration is not applied. A) 3D plot showing the mean and the 95% confidence intervals. The true source location and power are indicated with the dashed line and the dot at its tip, respectively. B) Two slices from the plot in A) to further illustrate the 95% confidence intervals. The black solid line and the blue dashed line indicate the mean values and the nominal values, respectively. A zoomed in view of the main beam region is also provided. Frequency is 5 kHz.

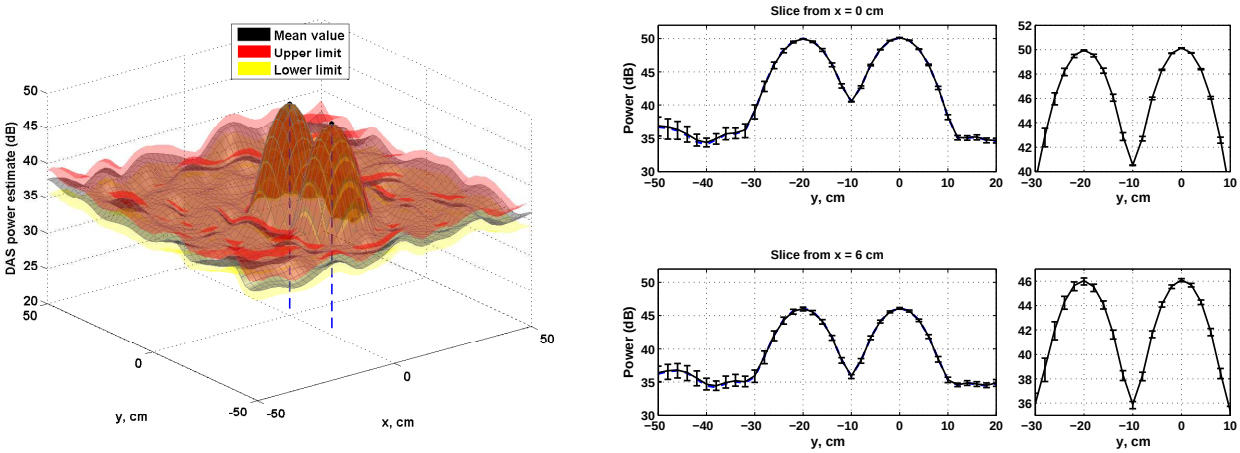

A B

Figure 6-12. Two sources are placed at (0, 0, 1.48) m and (0, -0.20, 1.48) m with equal strengths of 50 dB. Microphone locations are perturbed with a standard deviation of 10 mm and calibration is applied. A) 3D plot showing the mean and the 95% confidence intervals. The true source location and power are indicated with the dashed line and the dot at its tip, respectively. B) Two slices from the plot in A) to further illustrate the 95% confidence intervals. The black solid line and the blue dashed line indicate the mean values and the nominal values, respectively. A zoomed in view of the main beam region is also provided. The nominal and the mean values are indistinguishable at most y values. Frequency is 5 kHz.

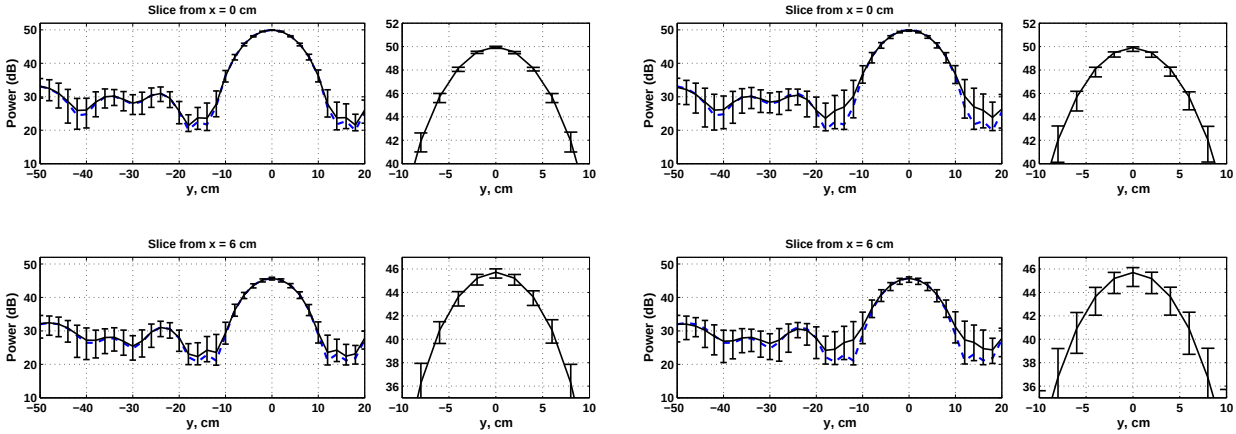

Figure 6-13. The 95% confidence intervals of the DAS power estimates when the array broadband distance is perturbed. Two slices from the beamforming image at $x = 0$ cm and $x = 6$ cm are considered. The relative uncertainty in array broadband distance is A) 2.5%, and B) 5%. The black solid line and the blue dashed line indicate the mean values and the nominal values, respectively. A zoomed in view of the main beam region is also provided. The nominal and the mean values are indistinguishable at some y values. Frequency is 5 kHz.

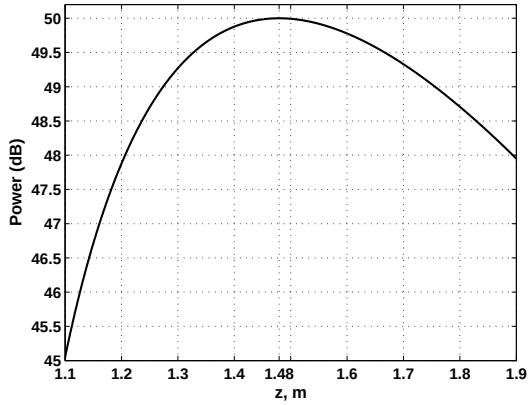

Figure 6-14. The power estimated at $(x, y) = (0, 0)$ m when the array broadband distance (in particular, z) is varied from 1.1 m to 1.9 m with increments of 0.5 mm. The true source distance to array is 1.48 m and the true source power is 50 dB. Frequency is 5 kHz.

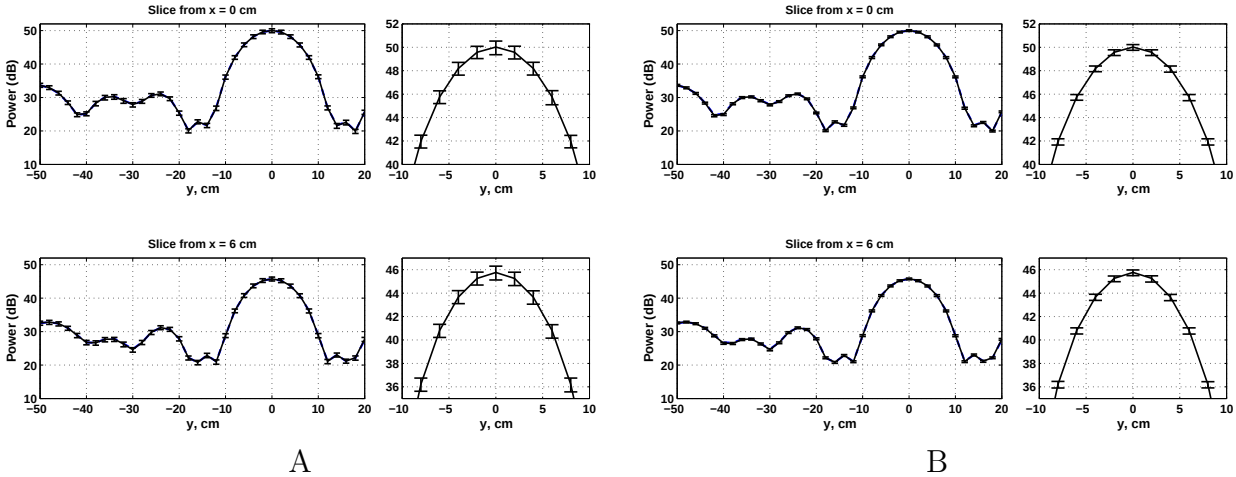

Figure 6-15. The 95% confidence intervals of the DAS power estimates when the CSM is perturbed. Two slices from the beamforming image at $x = 0$ cm and $x = 6$ cm are considered. Number of blocks are A) $B = 200$, and B) $B = 1000$. The black solid line and the blue dashed line indicate the mean values and the nominal values, respectively. A zoomed in view of the main beam region is also provided. The nominal and the mean values are indistinguishable at most y values. Frequency is 5 kHz.

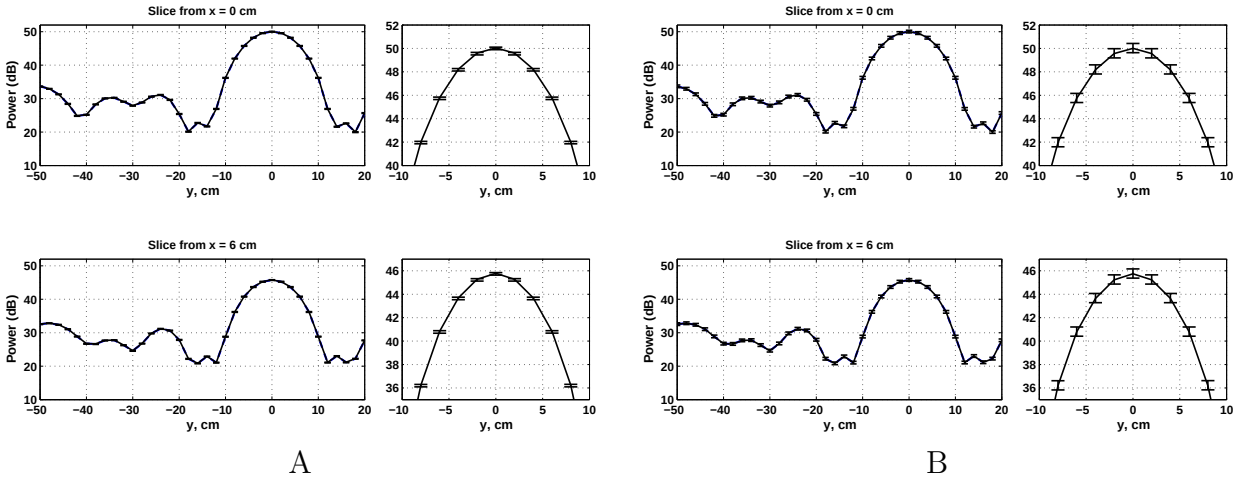

Figure 6-16. The 95% confidence intervals of the DAS power estimates when the individual microphone sensitivities are perturbed. Two slices from the beamforming image at $x = 0$ cm and $x = 6$ cm are considered. The relative input uncertainties are A) 5%, and B) 15%. The black solid line and the blue dashed line indicate the mean values and the nominal values, respectively. A zoomed in view of the main beam region is also provided. The nominal and the mean values are indistinguishable at most y values. Frequency is 5 kHz.

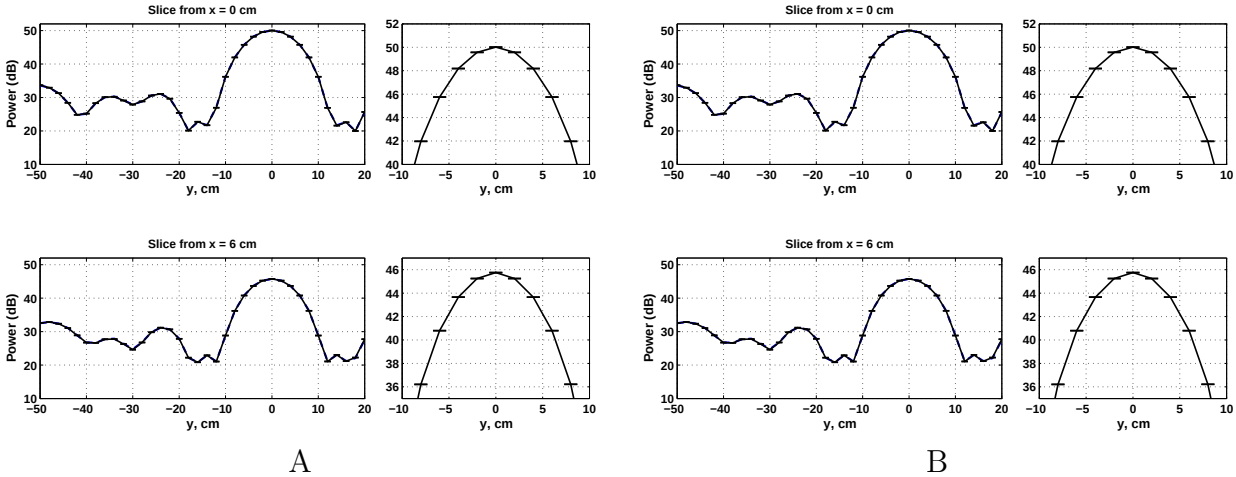

Figure 6-17. The 95% confidence intervals of the DAS power estimates when the individual microphone phases are perturbed. Two slices from the beamforming image at $x = 0$ cm and $x = 6$ cm are considered. The relative input uncertainties are A) 1°, and B) 10°. The black solid line and the blue dashed line indicate the mean values and the nominal values, respectively. A zoomed in view of the main beam region is also provided. The nominal and the mean values are indistinguishable at most y values. Frequency is 5 kHz.

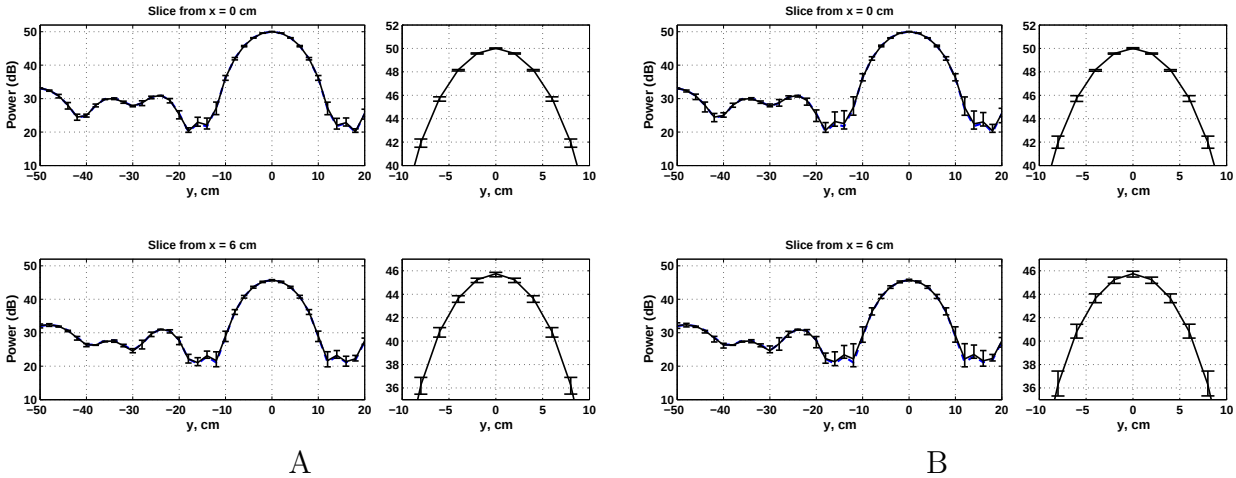

Figure 6-18. The 95% confidence intervals of the DAS power estimates when the temperature is perturbed. Two slices from the beamforming image at $x = 0$ cm and $x = 6$ cm are considered. The relative input uncertainties are A) 0.1° C, and B) 3° C. The black solid line and the blue dashed line indicate the mean values and the nominal values, respectively. A zoomed in view of the main beam region is also provided. The nominal and the mean values are indistinguishable at most y values. Frequency is 5 kHz.

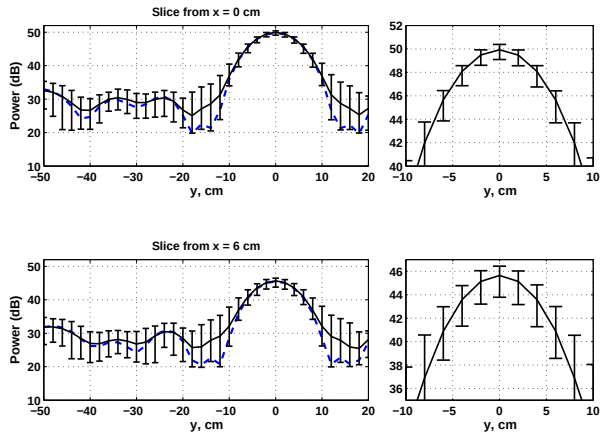

Figure 6-19. The 95% confidence intervals of the DAS power estimates when all the input variables are perturbed. See the text for specific perturbation values. Two slices from the beamforming image at $x = 0$ cm and $x = 6$ cm are considered. The black solid line and the blue dashed line indicate the mean values and the nominal values, respectively. A zoomed in view of the main beam region is also provided. The nominal and the mean values are indistinguishable at most y values. Frequency is 5 kHz.

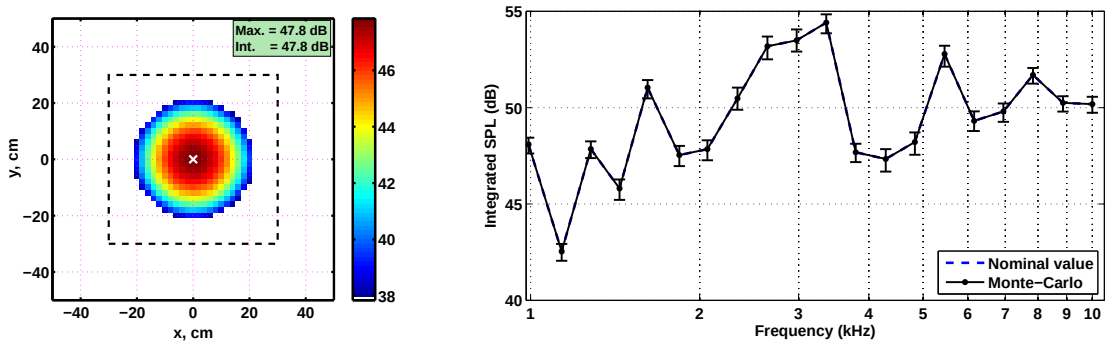

A B

Figure 6-20. Analysis of experimental data with a single source. A) The beamforming image at 2 kHz. The integration region is indicated with the dashed square and the true source location is indicated with the "x". The maximum (Max.) and integrated (Int.) levels are indicated on the plot. B) The 95% confidence intervals of the integrated DAS levels versus frequency. See the text for the input uncertainties. The nominal and the mean values are indistinguishable at most of the frequencies.

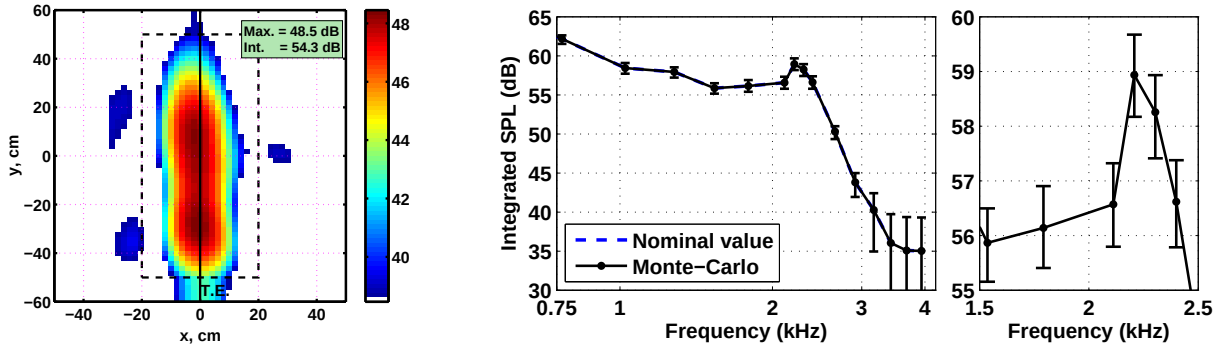

A B

Figure 6-21. Analysis of the NACA 63-215 Mod-B airfoil. A) The beamforming image at 2.5 kHz. The integration region is indicated with the dashed rectangle and the trailing edge (T.E.) is shown with the solid line. The maximum (Max.) and integrated (Int.) levels are indicated on the plot. B) The 95% confidence intervals of the integrated DAS levels versus frequency. See the text for the input uncertainties. A zoomed in view of the confidence intervals in the frequency range from 1.5 kHz to 2.5 kHz is also provided. The nominal and the mean values are indistinguishable at most of the frequencies.

Table 6-1. Error sources for the DAS beamformer.

Name	Error source	No. of variables
$\mathbf{V}_{\text{CSM}}$ (variables in $\mathbf{G}$)	Random averaging error	M^2
$\mathbf{V}_{\text{Calib}}$ (variables in $\mathbf{C}$)	Calibration errors	$2M$
$\mathbf{V}_{\text{Locs}}$ (microphone locations)	Distance measurement errors	$3M$
V_{Temp} (temperature)	Temperature measurement errors	1

Table 6-2. Covariances of the CSM variables (the elements in $\mathbf{g}_{\text{CSM}}$).

Variables	Covariance
G_{mm}, G_{mm}	$\lvert G_{mm}\rvert^2/B$
G_{mm}, G_{nn}	$\lvert G_{mn}\rvert^2/B$
G_{mm}, C_{np}	$(C_{mn}C_{mp} + Q_{mn}Q_{mp})/B$
G_{mm}, Q_{np}	$(C_{mn}Q_{mp} - Q_{mn}C_{mp})/B$
C_{mn}, C_{pq}	$(C_{mp}C_{nq} + Q_{mp}Q_{nq} + C_{mq}C_{np} + Q_{mq}Q_{np})/(2B)$
C_{mn}, Q_{pq}	$(C_{mp}Q_{nq} + Q_{mq}C_{np} - Q_{mp}C_{nq} - C_{mq}Q_{np})/(2B)$
Q_{mn}, Q_{pq}	$(C_{mp}C_{nq} + Q_{mp}Q_{mq} - C_{mq}C_{np} - Q_{mq}Q_{np})/(2B)$

CHAPTER 7
DIRECTIVE SOURCES AND SPATIALLY NON-WHITE NOISE

Most existing array processing algorithms for aeroacoustic noise measurement applications assume the presence of monopole sources in which case the steering vector for a given scanning point is a function of only the distance between each sensor and the scanning point (see Eq. 2–3). However, when the array aperture is large and the frequency is relatively high, directivity might no longer be negligible and the steering vectors now become a function of both the impinging angles from the scanning points to each sensor and the distances in between. Beamforming with directive sources is challenging since there is no prior knowledge on the directivity patterns of the sources; this makes the actual steering vectors unknown to the beamforming algorithm. Moreover, with directive sources, each sensor might encounter substantially different signal levels as opposed to the non-directive case. Although DAS can still be used to get a rough estimate of the source distribution, its performance might degrade significantly.

Beamforming with other types of sources besides monopoles has been analyzed by Suzuki [73]. This method uses the eigen-modes of the CSM together with a sparsity constraint to resolve the source parameters. Yet, this method assumes that the steering vectors of the non-monopole sources are known. CLEAN-SC is one of the few algorithms considering the case of unknown steering vectors [57]. As mentioned in Chapter 1, a disadvantage of CLEAN-SC is that it requires the selection of four user parameters. Dougherty suggests that the EVD of the CSM can be used to estimate the unknown steering vectors and the source powers [2]. It is well-known that subspace based beamforming algorithms are sensitive to measurement noise [8]. In this chapter, we present an iterative algorithm using convex programming for estimating the noise covariance matrix. This program is able to work with both diagonal (i.e., the noise is uncorrelated among sensors but may be of different power levels) and non-diagonal (i.e., the noise can be correlated or coherent among sensors) noise covariance matrices. The estimated signal

covariance matrix, determined by removing the estimated noise covariance matrix from the array covariance matrix, can then be used to estimate the source parameters using the aforementioned eigen-decomposition based technique.

7.1 Problem Formulation

Consider the data model introduced in Eq. 2–4. Under the monopole sources assumption, the array steering vector corresponding to the lth source was defined as (see Eq. 2–2):

$$\mathbf{a}_l^{(\text{mono})} = [e^{-jkr_{l,1}}/r_{l,1}, \ldots, e^{-jkr_{l,M}}/r_{l,M}]^T, \quad l = 1, \ldots, L_0. \tag{7–1}$$

Recall that L_0 is the number of sources. In the presence of directive sources, the steering vector for the lth source becomes: $\mathbf{a}_l = \mathbf{a}_l^{(\text{mono})} \odot \mathbf{d}_l$, where $\mathbf{d}_l = [D_l(\theta_{l,1}), \ldots, D_l(\theta_{l,M})]^T$ consists of the directivity terms ($\mathbf{d}_l = [1, 1, \ldots, 1]^T$ for a monopole source). For instance, when the lth source is a piston in an infinite baffle, the far-field expression for $\{D_l(\theta_{l,m})\}$ is:

$$D_l(\theta_{l,m}) = \frac{2J_1(kr\sin(\theta_{l,m}))}{kr\sin(\theta_{l,m})}, \tag{7–2}$$

where r is the radius of the plane piston, $J_1(\cdot)$ denotes the Bessel function of the first kind and $\theta_{m,l}$ denotes the emission angle of the lth source at the mth sensor (see Figure 7-1) [48]. (The directivity $D_l(\theta_{l,m})$ is assumed to be independent of the azimuth angle, i.e., $\theta_{m,l}$ is axisymmetric for a given m and l.) We assume that the modulus of the maximum directivity for each source is normalized to 1 in order to avoid ambiguity when estimating the source power levels.

Directive Source Localization

Recall from Eq. 3–2 that $\mathbf{G} = \mathbf{APA}^H$ in the noiseless case, where $\mathbf{P}$ is a diagonal matrix with the unknown source powers on its diagonal assuming that the sources are uncorrelated. Consequently, we obtain [2]

$$\mathbf{G}\mathbf{a}_l = (P_l\|\mathbf{a}_l\|_2^2)\mathbf{a}_l + \sum_{l'=1, l'\neq l}^{L_0} P_{l'}\mathbf{a}_{l'}(\mathbf{a}_{l'}^H\mathbf{a}_l), \quad l = 1, \ldots, L_0. \tag{7–3}$$

This equation shows that the actual steering vectors can be obtained from the EVD of $\mathbf{G}$. Since the second term on the right hand side of Eq. 7–3 is relatively small for widely separated sources and can be neglected, $\mathbf{a}_l/\|\mathbf{a}_l\|_2$ is approximately an eigenvector of $\mathbf{G}$ and $P_l\|\mathbf{a}_l\|_2^2$ is the corresponding eigenvalue [2]. Consequently, let $\mathbf{G} = \mathbf{U}\mathbf{\Lambda}\mathbf{U}^H$ be the EVD of $\mathbf{G}$, where the columns of the unitary matrix $\mathbf{U}$ denote the eigenvectors of $\mathbf{G}$ and the diagonal elements of the diagonal matrix $\mathbf{\Lambda}$ denote the corresponding eigenvalues $\{\lambda_m\}_{m=1}^M$ such that $\lambda_1 \geq \ldots \geq \lambda_M$. Let $\mathbf{u}_l$ denote the lth column of $\mathbf{U}$. The monopole steering vectors are used to estimate the locations of the dominant directive sources in the field. The location of the lth source corresponds to $\text{argmax}_{l'=1,\ldots,L}\left\{\frac{|(\mathbf{a}_{l'}^{(\text{mono})})^H\mathbf{u}_l|}{\|\mathbf{a}_{l'}^{(\text{mono})}\|_2^2}\right\}$. Recall that L is the number of scanning points in the image plane.

We can estimate the lth directivity vector as $\hat{\mathbf{d}}_l = \mathbf{u}_l./\mathbf{a}_l^{(\text{mono})}$, $l = 1,\ldots,L_0$, where "./" denotes the element-wise division. Note that $\hat{\mathbf{d}}_l$ is an estimate of a scaled version of the true $\mathbf{d}_l$ due to $\mathbf{u}_l$ being an orthonormal eigenvector of $\mathbf{G}$. In order to estimate the power levels accurately, $\hat{\mathbf{d}}_l$ should be normalized appropriately. One option is to normalize $\hat{\mathbf{d}}_l$ so that its largest element has unit modulus. An alternative is to fit a polynomial (a 4th-order polynomial is satisfactory) to the modulus of $\hat{\mathbf{d}}_l$ and normalize $\hat{\mathbf{d}}_l$ so that the maximum value of this polynomial over the entire angle range equals 1. It was empirically observed that these two methods yield almost identical results (since at least one sensor is likely to sample the directivity pattern near its maximum value), and hence the former easier approach is used in our examples. After $\hat{\mathbf{d}}_l$ is normalized (and still denoted as $\hat{\mathbf{d}}_l$), the power of the lth source is estimated as $\hat{P}_l = \frac{\lambda_l}{\|(\mathbf{a}_l^{(\text{mono})}\odot\hat{\mathbf{d}}_l\|_2^2}$, $l = 1,\ldots,L_0$. We refer to this algorithm as the directive source localizer (DSL). Note that DSL is similar to the procedure described by Dougherty [2] but it is more general since it can estimate the power levels even when $\|\mathbf{a}_l\|_2^2 \neq 1$, $l = 1,\ldots,L_0$.

The performance of DSL can be degraded when the array covariance matrix is contaminated with measurement noise unless the noise covariance matrix is a scaled identity matrix (in which case the eigenvectors are not affected). In practice, the noise

covariance matrix might be diagonal with unequal diagonal elements or non-diagonal since the noise in sensors that are close to each other can be highly correlated or even coherent. This will affect the subspace of $\mathbf{G}$, and the eigenvectors of $\mathbf{G}$ may no longer correspond to the true source steering vectors. Note that when the measurement noise is no longer diagonal, Eq. 3–2 becomes $\mathbf{G} = \mathbf{G}_{L_0} + \mathbf{G}_{\mathrm{E}}$, where $\mathbf{G}_{L_0} = \mathbf{APA}^H$ denotes the signal covariance matrix and $\mathbf{G}_{\mathrm{E}}$ denotes the measurement noise covariance matrix (note earlier, we have assumed that $\mathbf{G}_{\mathrm{E}} = \sigma^2\mathbf{I}$). To account for non-white measurement noise, a covariance matrix fitting methodology similar to CMF (see Section 3.4) can be used, where the noise covariance matrix and the source covariance matrix are estimated from $\mathbf{G}$ using an iterative procedure.

Assume that $\mathbf{G}_{L_0}$, which is a rank-L_0 matrix, is given. $\mathbf{G}_{\mathrm{E}}$ can then be estimated by solving the following convex optimization problem using SeDuMi [50]:

$$\hat{\mathbf{G}}_{\mathrm{E}} = \underset{\mathbf{G}_{\mathrm{E}}}{\operatorname{argmin}} \ \|\mathbf{G} - \mathbf{G}_{L_0} - \mathbf{G}_{\mathrm{E}}\|_{\mathrm{F}}^2 + \eta\|\mathbf{g}_{\mathrm{E}}\|_1, \tag{7–4}$$

where $\mathbf{g}_{\mathrm{E}} = \mathrm{vec}(\mathbf{G}_{\mathrm{E}})$ and η is a user parameter. In Eq. 7–4, the sparsity of the non-diagonal noise covariance matrix is enforced since it is assumed that the noise in only closely spaced sensors will be highly correlated with each other. Note that the minimizer of Eq. 7–4 must satisfy $\hat{\mathbf{G}}_{\mathrm{E}} \succeq 0$ and $\mathbf{G} - \hat{\mathbf{G}}_{\mathrm{E}} \succeq 0$ since $\hat{\mathbf{G}}_{\mathrm{E}}$ and $\mathbf{G} - \hat{\mathbf{G}}_{\mathrm{E}}$ are covariance matrices. Imposing the constraints $\mathbf{G}_{\mathrm{E}} \succeq 0$ and $\mathbf{G} - \mathbf{G}_{\mathrm{E}} \succeq 0$ to the program defined in Eq. 7–4 results in the so-called SDP [52], which is convex. Although these constraints will preserve the convexity of the optimization problem in Eq. 7–4, they will increase the computational complexity significantly, especially for large M. It is empirically observed that the solution to Eq. 7–4 satisfies these constraints automatically. (Alternatively, the negative eigenvalues of $\hat{\mathbf{G}}_{\mathrm{E}}$ and $\mathbf{G} - \hat{\mathbf{G}}_{\mathrm{E}}$ can be set to zero to enforce the positive semi-definiteness of the covariance matrices.)

Given $\mathbf{G}_{\mathrm{E}}$, the signal covariance matrix $\mathbf{G}_{L_0}$ can be estimated as the best rank-L_0 approximation to $\tilde{\mathbf{G}} = \mathbf{G} - \mathbf{G}_{\mathrm{E}}$ in the Frobenius norm sense. The solution is $\hat{\mathbf{G}}_{L_0} =$

$\tilde{\mathbf{U}}\tilde{\mathbf{\Gamma}}\tilde{\mathbf{U}}^H$, where $\tilde{\mathbf{\Gamma}}$ contains only the largest L_0 eigenvalues of $\tilde{\mathbf{G}}$ on its diagonal and $\tilde{\mathbf{G}} = \tilde{\mathbf{U}}\mathbf{\Gamma}\tilde{\mathbf{U}}^H$ is the EVD of $\tilde{\mathbf{G}}$.

As mentioned above, estimating $\mathbf{G}_{\mathrm{E}}$ requires $\mathbf{G}_{L_0}$ and vice versa. Therefore, the problem can be solved iteratively by first fixing $\mathbf{G}_{\mathrm{E}}$ and estimating $\mathbf{G}_{L_0}$ and then fixing $\mathbf{G}_{L_0}$ and estimating $\mathbf{G}_{\mathrm{E}}$. $\mathbf{G}_{\mathrm{E}}$ can be initialized as all zeros. After a certain number of iterations (25 in our examples), the so-obtained $\hat{\mathbf{G}}_{L_0}$ is used instead of $\mathbf{G}$ in DSL. At each iteration, η can be chosen simply as $\|\mathbf{G} - \hat{\mathbf{G}}_{L_0} - \hat{\mathbf{G}}_{\mathrm{E}}\|_{\mathrm{F}}^2 / \|\hat{\mathbf{g}}_{\mathrm{E}}\|_1$, where $\hat{\mathbf{G}}_{L_0}$ and $\hat{\mathbf{G}}_{\mathrm{E}}$ are the latest estimates of $\mathbf{G}_{L_0}$ and $\mathbf{G}_{\mathrm{E}}$, respectively. The initial value of $\|\mathbf{g}_{\mathrm{E}}\|_1$ can be computed as $C\sum_{l=L_0+1}^{M}\lambda_l$, where C is a constant. Since $\mathbf{G}_{\mathrm{E}}$ can be non-diagonal, C is used to compensate for the off-diagonal terms of $\mathbf{G}_{\mathrm{E}}$. ($C = 20$ in our examples.) This procedure is referred to as DSL with noise extraction (DSL-NE). DSL-NE is not very sensitive to the selection of C. Moreover, it is empirically observed that after a certain number of iterations, η converges to a fixed value and hence the algorithm becomes cyclic, i.e., the cost function in Eq. 7–4 is guaranteed to not increase at each iteration (note that an iterative algorithm is not necessarily cyclic, whereas a cyclic algorithm is iterative). The cyclic property of DSL-NE ensures that it will converge at least locally. Finally, note that since $\mathbf{G}$ is not available in practice, it is replaced by the CSM, i.e., $\hat{\mathbf{G}}$, as usual.

7.2 Numerical Examples

This section evaluates the performance of DAS, CLEAN-SC, DSL and DSL-NE for two uncorrelated directive sources and with LAMDA. Figure 7-2 A shows the simulated directivity (computed by Eq. 7–2 with $r = 0.03$ m and $kr = 9.9$) of a source, which is placed 0.2 m off-center in both the x- and y-axes and at a height of 1 m, versus its emission angle. The circles in Figure 7-2 A denote the directivity values encountered by the array sensors for this source. Figures 7-2 B and 7-2 C show the reduction relative to the source axis (in dB) incurred at each array sensor by a monopole source and a directive source, respectively, which are placed at 0.2 m off-center in both the x- and y-axes and 1 m above the array plane. It is observed that directivity results in severe amplitude

differences among different sensors (even very closely spaced ones) and that the monopole weighting applied by DAS, which is designed to compensate for the loss in Figure 7-2 B, will be unable to compensate for the loss due to directivity.

We first consider two directive sources (with their directivity pattern shown in Figure 7-2 A): one placed at the origin (with 60 dB power) and the other one at $x = y = 0.2$ m (with 55 dB power). Both sources are placed 1 m above the array plane. The signal and noise waveforms are generated as zero-mean circularly symmetric i.i.d. complex Gaussian random processes. The noise covariance matrix is a scaled identity matrix, the SNR is 0 dB and $B = 500$. (The SNR is defined as $10\log_{10}$ of the ratio of the minimum source power to the noise variance.) Figure 7-3 shows the beamforming images obtained by DAS, CLEAN-SC and DSL (DSL-NE image is identical to the DSL image and hence is not shown). We observe that DAS suffers from poor resolution whereas CLEAN-SC, DSL and DSL-NE can clearly identify the two dominant sources. The power estimates of the algorithms are also noted in the figures. DAS and CLEAN-SC are unable to estimate the power levels correctly.

In the second example, we keep the sources, as well as their locations and powers, the same as in the previous example but let the noise covariance matrix be non-diagonal: the non-diagonal noise covariance matrix is generated as $\mathbf{Q}^H\mathbf{Q}$, where $\mathbf{Q}$ is a symmetric $M \times M$ matrix with its $(m, m')^{\text{th}}$ entry equal to 1 if sensors m and m' $(m, m' = 1, \ldots, M)$ are closer to each other than 0.15 m. SNR is set at -5 dB and $B = 500$. (With the non-diagonal noise covariance matrix, the SNR is defined as $10\log_{10}$ of the ratio of the minimum source power to the largest diagonal element of the noise covariance matrix.) We observe that in this case, DSL cannot identify the location of the weaker source correctly whereas DSL-NE can still accurately identify both of the sources. CLEAN-SC also fails to resolve the off-center source clearly and the background clutter is high. The computation times of DSL, DSL-NE and CLEAN-SC in this example were 0.3, 31.2 and 2.1 seconds, respectively. DSL-NE takes the longest time due to solving Eq. 7–4 at each iteration.

Note that we have assumed that the number of sources L_0 is known while running DSL and DSL-NE. In results not shown, it was observed that the algorithms, especially DSL-NE, can still provide reasonable performance when the assumed number of sources is larger than the actual number of sources.

7.3 Conclusions

A beamforming algorithm (named DSL) based on the eigen decomposition of the array covariance matrix can be used for the localization of directive sources with unknown directivity patterns [2]. An extension of DSL, DSL-NE, has been presented to extract the noise covariance matrix from the array covariance matrix using an iterative algorithm and convex optimization to achieve better estimation performance. It has been shown via numerical examples that DSL and DSL-NE show better performance than DAS and CLEAN-SC and that DSL-NE shows better performance than DSL with spatially non-white measurement noise.

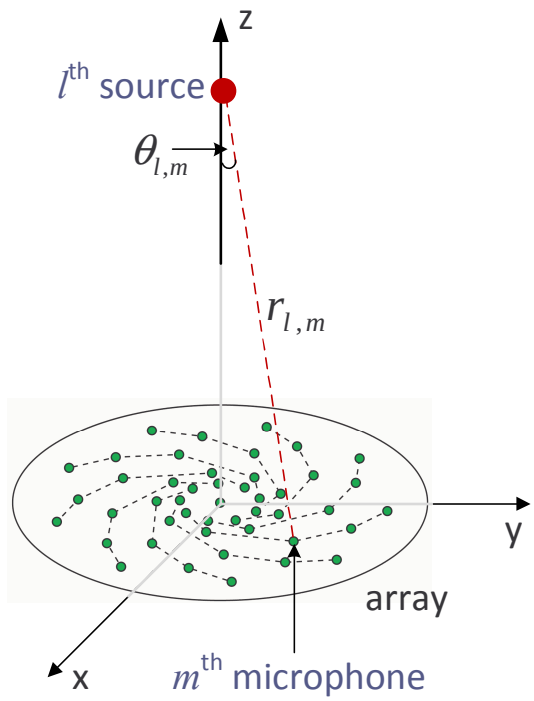

Figure 7-1. A planar microphone array extending in the xy-plane with M microphones (shown by the circles) and in the presence of a directive source.

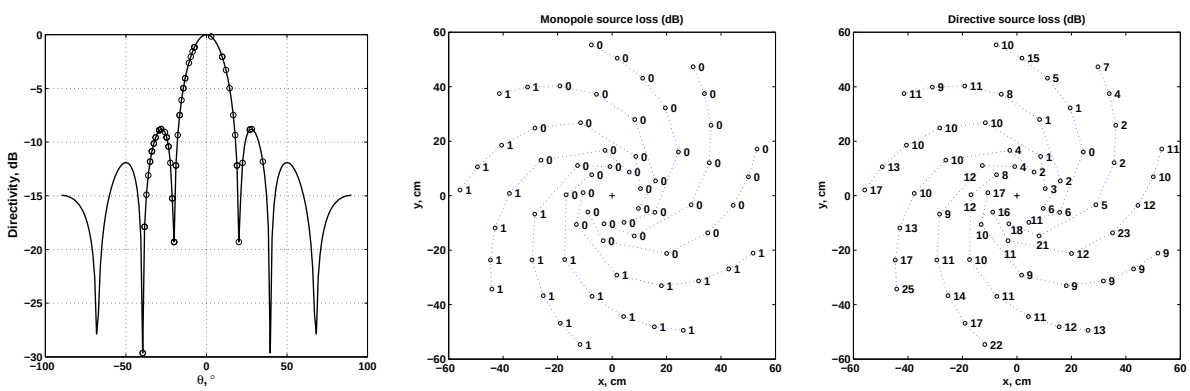

A B C

Figure 7-2. The directivities observed at the array microphones. A) Absolute value of the directivity versus the emission angle. The circles show the directivity values that the array sensors encounter with the directive source placed at $x = y = 0.2$ m and 1 m above the array plane. Absolute value (rounded and in dB) of the propagation loss at each microphone for a source at $x = y = 0.2$ m and 1 m above the array plane: B) monopole source, and C) directive source.

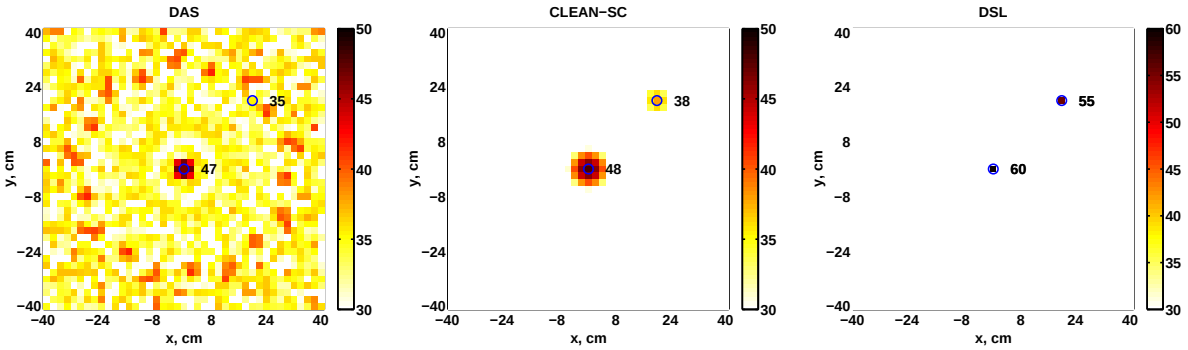

Figure 7-3. Two directive sources located at $x = y = 0$ m (60 dB) and $x = y = 0.2$ m (55 dB) (as indicated by the circles). Both sources are located 1 m above the array plane. Noise with scaled identity covariance matrix is applied. SNR = 0 dB. The power estimates of the algorithms are noted in the figures. DSL-NE image is identical to the DSL image and hence is not shown.

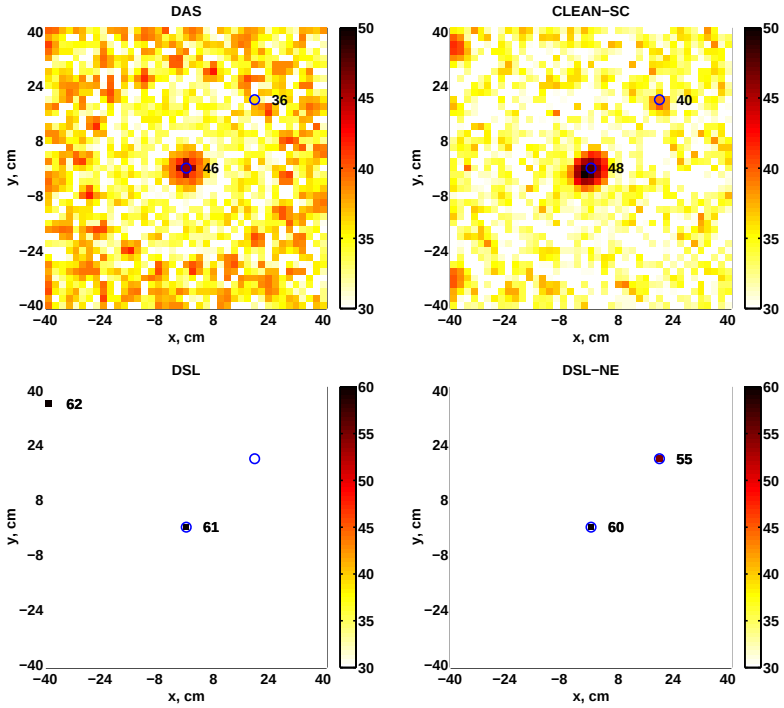

Figure 7-4. Two directive sources located at $x = y = 0$ m (60 dB) and $x = y = 0.2$ m (55 dB) (as indicated by the circles). Both sources are located 1 m above the array plane. Noise with a non-diagonal covariance matrix is applied. SNR = -5 dB. The power estimates of the algorithms are noted in the figures.

CHAPTER 8
CONCLUSIONS AND FUTURE WORK

8.1 Conclusions

In this dissertation we have discussed various aspects of microphone array processing for aeroacoustic measurements. We have shown the challenges involved in noise source localization and power estimation, and developed a number of new array processing techniques. These techniques were evaluated using both simulated and experimental data.

First, we have discussed deconvolution methods for eliminating the effects of the array response from the DAS beamforming result assuming that the sources are uncorrelated. We have proposed two deconvolution approaches, namely SC-DAMAS and CMF, based on sparsity and convex optimization. We have shown that by leveraging sparsity, improvements in estimation accuracy and computation time can be achieved. We have then evaluated the proposed algorithms with experimental test cases and a NACA 63-215 Mod B airfoil tested in the presence of flow. It was shown that the proposed algorithms are as effective with experimental data as they are with simulated data.

Next, we have discussed deconvolution methods for correlated sources. We have proposed a new deconvolution algorithm, namely CMF-C, by extending CMF. However, this algorithm is computationally very demanding. Therefore, we have also presented another approach, called MACS, for the efficient mapping of correlated acoustic sources in aeroacoustic measurements. This algorithm was demonstrated to be effective with simulated and experimental data.

We have also presented a systematic uncertainty analysis of the DAS beamformer and the array calibration procedure. Our analysis showed that with experimental data and in the presence of flow, errors in the range of ± 1 dB are to be expected when reporting integrated levels with DAS.

Finally, we have presented a beamforming method, named DSL-NE, that can deal with directive sources and non-diagonal measurement noise covariance matrices. It was

shown with numerical data that DSL-NE can localize directive sources given that they are well-separated.

8.2 Future Work

There are a number of possible future research directions that could be pursued. We list some ideas below.

An uncertainty analysis of the calibration procedure has been presented in this dissertation. In addition to this analysis, the sensitivity of the calibration procedure to the validity of its assumptions (monopole source, no reflections and so on) could be analyzed. This is of practical interest since the individual calibration of hundreds of microphones is an expensive task.

The fast beamforming method proposed in Chapter 5 can be analyzed by further experiments resembling the simulated examples. This is important as most of the existing deconvolution techniques assume that the sources are uncorrelated and the effects of source coherence on the beamforming maps obtained with these methods is unclear.

We have presented the uncertainty analysis of the DAS beamformer. The same analysis can be extended to estimate the uncertainty of more advanced algorithms such as DAMAS. This might involve the development of new uncertainty analysis techniques as the multivariate and Monte-Carlo based methods will most likely be computationally infeasible with the advanced beamforming algorithms.

Moreover, the further development and analysis of the proposed algorithm in Chapter 7 for directive source localization might be of interest. Measurement noise covariance matrix estimation is another topic of big interest [74] as the current method of diagonal removal is not very appealing from a theoretical point of view.

Finally, we note that an iterative adaptive approach (IAA) was developed during this dissertation study for applications similar to aeroacoustic noise measurements. IAA was shown to be promising in a number of applications including passive far-field array processing [44, 75], radar/sonar range-Doppler imaging [44], underwater multi-input

multi-output (MIMO) communications [76], and MIMO range-Doppler-angle imaging [77]. IAA was shown to be an approximation to another iterative technique based on likelihood maximization (called IAA-ML) [78, 79]. Furthermore, DAMAS can be shown to be an approximation to IAA-ML. Therefore, these algorithms can be analyzed within the aeroacoustic measurements framework and compared with the methods presented in this dissertation.

APPENDIX A
JACOBIAN MATRIX

This appendix derives the closed-form expressions for the Jacobian matrices with respect to all of the input variables in $\mathbf{V}$ (see Section 6.2). Note that the Jacobians are evaluated using the nominal values of the input variables.

A.1 Jacobian Matrix for the CSM

The derivatives of P_l with respect to the CSM elements are

$$\frac{\partial P_l}{\partial G_{mm}} = \frac{1}{M^2}|\tilde{D}_m|^2\left(\frac{r_{l,m}}{r_{l,0}}\right)^2, \quad m = 1,\ldots,M, \tag{A–1}$$

$$\frac{\partial P_l}{\partial C_{mn}} = \frac{2}{M^2}\frac{r_{l,m}r_{l,n}}{r_{l,0}^2}\mathrm{Re}\left\{\tilde{D}_m\tilde{D}_n^* e^{jk(r_{l,m}-r_{l,n})}\right\}, \quad m,n = 1,\ldots,M,\ m \neq n, \text{ and} \tag{A–2}$$

$$\frac{\partial P_l}{\partial Q_{mn}} = -\frac{2}{M^2}\frac{r_{l,m}r_{l,n}}{r_{l,0}^2}\mathrm{Im}\left\{\tilde{D}_m\tilde{D}_n^* e^{jk(r_{l,m}-r_{l,n})}\right\}, \quad m,n = 1,\ldots,M,\ m \neq n. \tag{A–3}$$

A.2 Jacobian Matrix for the Calibration Factors

The derivative of P_l with respect to D_m can be written as

$$\frac{\partial P_l}{\partial D_m} = \frac{2}{M^2 r_{l,0}^2}\left(r_{l,m}^2 D_m G_{mm} + \mathrm{Re}\left\{r_{l,m}e^{-jkr_{l,m}}\sum_{p=1,p\neq m}^{M} r_{l,p}e^{jkr_{l,p}}\tilde{D}_p G_{pm}\right\}\right), \quad m = 1,\ldots,M. \tag{A–4}$$

The derivative with respect to E_m is obtained by replacing D_m by E_m and the real component by the imaginary component of the argument in Eq. A–4.

A.3 Jacobian Matrix for Microphone Locations

The derivative of P_l with respect to x_m is given by

$$\frac{\partial P_l}{\partial x_m} = \frac{1}{M^2}\left[|\tilde{D}_m|^2\frac{\partial}{\partial x_m}\left(\frac{r_{l,m}^2}{r_{l,0}^2}\right) + 2\mathrm{Re}\left\{\sum_{p=1,p\neq m}^{M}\tilde{D}_p^*\tilde{D}_m r_{l,p}e^{-jkr_{l,p}}\frac{\partial}{\partial x_m}\left(\frac{1}{r_{l,0}^2}r_{l,m}e^{jkr_{l,m}}\right)\right\}\right], \tag{A–5}$$

where

$$\frac{\partial}{\partial x_m}(r_{l,m}e^{jkr_{l,m}}) = -(\tilde{x}_l - x_m)(1/r_{l,m} + jk)e^{jkr_{l,m}}, \tag{A–6}$$

$$\frac{\partial}{\partial x_m}\left(\frac{1}{r_{l,0}^2}\right) = \frac{2\,(x_l - \bar{x})}{M r_{l,0}^4}, \quad \text{and} \quad \frac{\partial r_{l,m}^2}{\partial x_m} = -2(\tilde{x}_l - x_m), \tag{A–7}$$

for $m = 1, \ldots, M$. A closed-form expression can be obtained for Eq. A–5 by using the product rule for differentiation together with Eq. A–6 and Eq. A–7. Similar expressions can be obtained for y_m and z_m by replacing $\tilde{x}_l$ with $\tilde{y}_l$ or $\tilde{z}_l$ and x_m with y_m or z_m.

A.4 Jacobian Matrix for Temperature

The derivative of P_l with respect to temperature can be calculated using

$$\frac{\partial P_l}{\partial T} = \frac{\partial P_l}{\partial k}\frac{\partial k}{\partial T}, \tag{A–8}$$

where

$$\frac{\partial P_l}{\partial k} = -\frac{2}{M^2 r_{l,0}^2}\mathrm{Im}\left\{\sum_{m=1}^{M-1}\sum_{n=m+1}^{M}\tilde{D}_m\tilde{D}_n^* r_{l,m} r_{l,n}(r_{l,m} - r_{l,n})e^{jk(r_{l,m}-r_{l,n})}G_{mn}\right\}, \tag{A–9}$$

$$\frac{\partial k}{\partial T} = -\frac{k}{2T_0}, \tag{A–10}$$

and T_0 is the room temperature.

Note that it is difficult to comment on the scaling of the sensitivity coefficients due to the complexity of the corresponding expressions and the high correlation between the input variables. For instance, although it appears that the sensitivity coefficients of the CSM decrease by M^2, the contributions from all the terms ($\mathbf{J}_{\mathrm{CSM}}\mathbf{g}_{\mathrm{CSM}}\mathbf{J}_{\mathrm{CSM}}^T$ in Eq. 6–14) will also scale with M^2 and hence the effect of M will be cancelled out.

APPENDIX B
COVARIANCE MATRIX OF THE CSM

This appendix derives the covariances between all the real and imaginary components of the $M \times M$ complex symmetric CSM, $\hat{\mathbf{G}}$ (see Section 6.2).

Let the pressures measured at microphones m and n be denoted as $p'_m(t)$ and $p'_n(t)$, respectively, where t denotes time. Note that unless otherwise stated, the indices m and n both run from 1 to M. The finite Fourier transforms of $p'_m(t)$ and $p'_n(t)$ are then defined as [54]

$$\begin{aligned} y_m(f) &= \int_0^T p'_m(t) e^{-j2\pi ft} dt = y_{m,R}(f) - j y_{m,I}(f), \text{ and} \\ y_n(f) &= \int_0^T p'_n(t) e^{-j2\pi ft} dt = y_{n,R}(f) - j y_{n,I}(f), \end{aligned} \tag{B–1}$$

where $y_{m,R}(f)$ and $y_{m,I}(f)$ denote the real and imaginary parts of $y_m(f)$, respectively, (similarly for $y_n(f)$) and $T = H/f_s$ is the finite block length in time. The raw estimate for the cross-spectrum is then given by [54]

$$G_{mn}(f_h) = \frac{2}{T} y_m(f_h) y_n^*(f_h), \quad h = 0, 1, \ldots, H/2. \tag{B–2}$$

Note that when $p'_m(t)$ and $p'_n(t)$ are assumed to be normally distributed with zero mean, so will be $y_m(f)$ and $y_n(f)$. The frequency variable f is omitted in the rest for notational simplicity. From Eq. B–1 and Eq. B–2 we obtain [54]

$$G_{mm} = \frac{2}{T}(y_{m,R}^2 + y_{m,I}^2), \;\; G_{nn} = \frac{2}{T}(y_{n,R}^2 + y_{n,I}^2), \tag{B–3}$$

and

$$C_{mn} = \frac{2}{T}(y_{m,R} y_{n,R} + y_{m,I} y_{n,I}), \;\; Q_{mn} = \frac{2}{T}(y_{m,R} y_{n,I} - y_{m,I} y_{n,R}). \tag{B–4}$$

Moreover, from Eq. B–1 evaluated at $f = f_0, f_1, \ldots, f_{H/2}$, or equivalently, at $f = 0, 1/T, \ldots, H/(2T)$, we obtain [54]

$$\begin{aligned} E[y_{m,R}y_{m,I}] &= E[y_{n,R}y_{n,I}] = 0, \\ E[y_{m,R}^2] &= E[y_{m,I}^2] = \frac{T}{4}G_{mm}, \\ E[y_{n,R}^2] &= E[y_{n,I}^2] = \frac{T}{4}G_{nn}, \end{aligned} \tag{B–5}$$

and

$$E[y_{m,R}y_{n,R}] = E[y_{m,I}y_{n,I}] = \frac{T}{4}C_{mn}, \;\; E[y_{m,R}y_{n,I}] = -E[y_{m,I}y_{n,R}] = \frac{T}{4}Q_{mn}. \tag{B–6}$$

In order to compute the covariance between C_{mn} and Q_{pq}, we need to find

$$\begin{aligned} E[C_{mn}Q_{pq}] &= \frac{4}{T^2}E[(y_{m,R}y_{n,R} + y_{m,I}y_{n,I})(y_{p,R}y_{q,I} - y_{p,I}y_{q,R})] \\ &= \frac{4}{T^2}(E[y_{m,R}y_{n,R}y_{p,R}y_{q,I}] - E[y_{m,R}y_{n,R}y_{p,I}y_{q,R}] \\ &+ E[y_{m,I}y_{n,I}y_{p,R}y_{q,I}] - E[y_{m,I}y_{n,I}y_{p,I}y_{q,R}]) \\ &= C_{mn}Q_{pq} + \frac{1}{2}(C_{mp}Q_{nq} + Q_{mq}C_{np} - Q_{mp}C_{nq} - C_{mq}Q_{np}), \end{aligned} \tag{B–7}$$

where we have used the fact that for any four Gaussian variables a_1, a_2, a_3, a_4 with zero mean values [54]

$$E[a_1, a_2, a_3, a_4] = E[a_1, a_2]E[a_3, a_4] + E[a_1, a_3]E[a_2, a_4] + E[a_1, a_4]E[a_2, a_3]. \tag{B–8}$$

Since $E[G_{mm}] = G_{mm}$, $E[G_{nn}] = G_{nn}$, $E[C_{mn}] = C_{mn}$ and $E[Q_{pq}] = Q_{pq}$ (see Eqs. (B–3)-(B–6)), it follows that

$$\mathrm{Cov}(C_{mn}, Q_{pq}) = \frac{1}{2}(C_{mp}Q_{nq} + Q_{mq}C_{np} - Q_{mp}C_{nq} - C_{mq}Q_{np}), \quad m, n, p, q = 1, \ldots, M. \tag{B–9}$$

The other covariance formulas listed in Table 6-2 can be obtained in a similar manner.

APPENDIX C
GENERATING CORRELATED GAUSSIAN RANDOM VARIABLES

This appendix provides a short description on how Gaussian random variables with a given covariance matrix can be generated (see Section 6.2).

To generate Gaussian random vectors with zero mean and covariance matrix $\mathbf{\Sigma}$, we first generate an i.i.d. Gaussian random vector with zero mean and unit variance. Denoting this random vector with $\boldsymbol{\eta}$, $\mathbf{\Lambda}\boldsymbol{\eta}$ will yield a Gaussian random vector with covariance matrix $\mathbf{\Sigma}$ and zero mean provided that $\mathbf{\Lambda}\mathbf{\Lambda}^H = \mathbf{\Sigma}$. $\mathbf{\Lambda}$ can be obtained from the Cholesky decomposition of $\mathbf{\Sigma}$ [49].

Let the number of Monte-Carlo trials be denoted by N_{trial}. We recommended that N_{trial} perturbation vectors be generated simultaneously before implementing the Monte-Carlo analysis rather than generating a single perturbation vector at each Monte-Carlo iteration (i.e., N_{trial} times) since calculating $\mathbf{\Lambda}$ can be a time-consuming process.

APPENDIX D
MORE ON MICROPHONE LOCATION ERRORS

This appendix elaborates on the bias observed in the DAS power estimates when the microphone locations are perturbed (see Section 6.3.2.2).

Assume that there is only a single source present and that there is no contaminating noise. Moreover assume that only the microphone locations are perturbed. Consequently (see Eq. 2–8),

$$\mathbf{G} = P_0 \mathbf{a}\mathbf{a}^H, \tag{D–1}$$

where P_0 is the power of the source and $\mathbf{a}$ is the steering vector corresponding to the source, i.e., $\mathbf{a} = \left[e^{-jkr_{0,1}}/r_{0,1}, \ldots, e^{-jkr_{0,M}}/r_{0,M}\right]^T$, with $r_{0,m}$ denoting the distance between the mth microphone and the source location. When the microphone locations are perturbed, the distance between the mth microphone and the source location becomes $r_{0,m} + \delta r_m$, where δr_m denotes the perturbation and it can be negative or positive. The perturbed DAS estimate of the source power is then (by omitting calibration errors in Eq. 2–9)

$$\hat{P}_0 = \frac{1}{M^2} \tilde{\mathbf{a}}_{\text{p}}^H \mathbf{G} \tilde{\mathbf{a}}_{\text{p}}, \tag{D–2}$$

where $\tilde{\mathbf{a}}_{\text{p}}$ is the perturbed version of Eq. 2–6 and is defined as

$$\tilde{\mathbf{a}}_{\text{p}} = \frac{1}{r_{0,0}} \left[(r_{0,1} + \delta r_1) e^{-jk(r_{0,1}+\delta r_1)}, \ldots, (r_{0,M} + \delta r_M) e^{-jk(r_{0,M}+\delta r_M)}\right]^T. \tag{D–3}$$

Note that $r_{0,0}$ (the distance between the source and the array center) is not going to be affected much by the perturbations since the array center will remain approximately at the same location when the microphone locations are perturbed with i.i.d. Gaussian random variables with zero mean values. Therefore,

$$\hat{P}_0 = \left| \frac{1}{M} \sum_{m=1}^{M} \left(1 + \frac{\delta r_m}{r_{0,m}}\right) e^{jk\delta r_m} \right|^2 \tilde{P}_0, \tag{D–4}$$

where $\tilde{P}_0 = P_0/r_{0,0}^2$ is the source power at the array center. Note that when the microphone locations are not perturbed, $\delta r_m = 0$, $m = 1, \ldots, M$, and hence $\hat{P}_0 = \tilde{P}_0$.

However, when $\delta r_m \neq 0$, since f is relatively large and the perturbations appear on the phase terms, even small perturbations can affect the overall result. Using the Cauchy-Schwarz inequality gives [63]

$$\left| \frac{1}{M} \sum_{m=1}^{M} \left(1 + \frac{\delta r_m}{r_{0,m}}\right) e^{jk\delta r_m} \right|^2 \leq 1 + \frac{1}{M} \sum_{m=1}^{M} \frac{2\delta r_m}{r_{0,m}} + \frac{1}{M} \sum_{m=1}^{M} \left(\frac{\delta r_m}{r_{0,m}}\right)^2 \approx 1,$$

where since $\delta r_m \ll r_{0,m}$, the second and third terms have been neglected in the last equality. So, we can approximately claim that $\hat{P}_0 \leq \tilde{P}_0$. We plot $\left(1 + \frac{\delta r_m}{r_{0,m}}\right) e^{jk\delta r_m}$, $m = 1, \ldots, M$, for a single Monte-Carlo trial in Figure D-1, where the standard deviation of the perturbation δr_m is chosen to be 1 and 10 mm. We observe that as $f\delta r_m$ gets larger, the phase $k\delta r_m = \frac{2\pi f}{c}\delta r_m$ starts to deviate from the nominal value of 0°, whereas the amplitude is always around 1 regardless of f since $\left(1 + \frac{\delta r_m}{r_{0,m}}\right) \approx 1$. Therefore, we conclude that for relatively large $f\delta r_{0,m}$, the average of the samples (marked with a cross in the plots) will have amplitude much smaller than 1 which means that the average squared, i.e., $\hat{P}_0/\tilde{P}_0$, will be even smaller.

Another rather simple argument is that since the non-perturbed $\tilde{\mathbf{a}}_l$ are designed so as to maximize the beamforming output for the lth scanning point, when the locations are perturbed, the mismatch between $\tilde{\mathbf{a}}_l$ and $\mathbf{a}_l$ will result in equal or smaller power estimates than the true power. Therefore, this will create a negative bias in the power estimates.

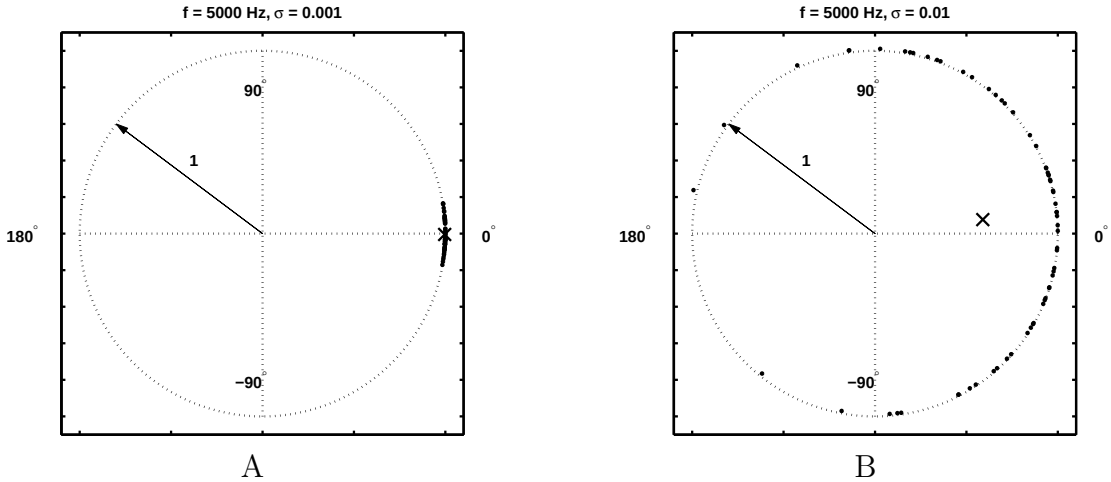

Figure D-1. The polar plot of $\left(1+\frac{\delta r_m}{r_{0,m}}\right)e^{jk\delta r_m}$, $m=1,\ldots,M$, at one Monte-Carlo trial, where the standard deviation of the perturbation δr_m is chosen to be A) 1 mm and B) 10 mm. $f=5$ kHz and $z=1.48$ m as usual. The cross marks indicate the averages of the M values in each plot.

REFERENCES

[1] W. M. Humphreys, T. F. Brooks, W. W. Hunter, and K. R. Meadows, "Design and use of microphone directional arrays for aeroacoustic measurements," *4th AIAA/CEAS Aeroacoustics Conference, AIAA-98-0471,* Reno, NV, Jan 1998.

[2] R. P. Dougherty *"Beamforming in acoustic testing", Aeroacoustic measurements,* Edited by T. J. Mueller, Springer, pp. 63–97, 2002.

[3] T. F. Brooks and W. M. Humphreys, Jr., "Effect of directional array size on the measurement of airframe noise components," *5th AIAA/CEAS Aeroacoustics Conference, AIAA-99-1958,* Bellevue, WA, May 1999.

[4] K. R. Meadows, T. F. Brooks, W. M. Humphreys, Jr., W. W. Hunter, and C. H. Gerhold, "Aeroacoustic measurements of a wing-flap configuration," *3rd AIAA/CEAS Aeroacoustics Conference, AIAA-97-1595,* Atlanta, GA, May 1997.

[5] J. R. Underbrink, *Practical Considerations in Array Design for Passive Broad-Band Source Mapping Applications.* The Pennsylvania State University, State College, PA, 1995.

[6] J. R. Underbrink *"Aeroacoustic Phased Array Testing in Low Speed Wind Tunnels", Aeroacoustic Measurements,* Edited by T. J. Mueller, Springer, pp. 99–217, 2002.

[7] D. H. Johnson and D. E. Dudgeon, *Array Signal Processing: Concepts and Techniques.* NJ: Prentice Hall, 1993.

[8] P. Stoica and R. L. Moses, *Spectral Analysis of Signals.* Upper Saddle River, NJ: Prentice-Hall, 2005.

[9] H. L. Van Trees, *Optimum Array Processing: part IV of Detection, Estimation, and Modulation Theory.* New York, NY: John Wiley & Sons, 2002.

[10] T. F. Brooks, M. A. Marcolini, and D. S. Pope, "A directional array approach for the measurement of rotor noise source distributions with controlled spatial resolution," *Journal of Sound and Vibration*, vol. 112, pp. 192–197, 1987.

[11] J. Li, Y. Xie, P. Stoica, X. Zheng, and J. Ward, "Beampattern synthesis via a matrix approach for signal power estimation," *IEEE Transactions on Signal Processing*, vol. 55, pp. 5643–5657, December 2007.

[12] J. Li, P. Stoica, and Z. Wang, "On robust Capon beamforming and diagonal loading," *IEEE Transactions on Signal Processing*, vol. 51, pp. 1702–1715, July 2003.

[13] J. Li, P. Stoica, and Z. Wang, "Doubly constrained robust Capon beamformer," *IEEE Transactions on Signal Processing*, vol. 52, pp. 2407–2423, September 2004.

[14] J. Li and P. Stoica, eds., *Robust Adaptive Beamforming.* New York, NY: John Wiley & Sons, 2005.

[15] J. Li and P. Stoica, "Efficient mixed-spectrum estimation with applications to target feature extraction," *IEEE Transactions on Signal Processing*, vol. 44, pp. 281–295, February 1996.

[16] Z. Wang, J. Li, P. Stoica, T. Nishida, and M. Sheplak, "Wideband RELAX and wideband CLEAN for aeroacoustic imaging," *The Journal of the Acoustical Society of America*, vol. 115, pp. 757–767, Feb. 2004.

[17] T. F. Brooks and W. M. Humphreys, "A deconvolution approach for the mapping of acoustic sources (DAMAS) determined from phased microphone arrays," *10th AIAA/CEAS Aeroacoustics Conference, AIAA-2004-2954,* Manchester, UK, May 2004.

[18] T. F. Brooks and W. M. Humphreys, "A deconvolution approach for the mapping of acoustic sources (DAMAS) determined from phased microphone arrays," *Journal of Sound and Vibration*, vol. 294, pp. 856–879, July 2006.

[19] K. Ehrenfried and L. Koop, "A comparison of iterative deconvolution algorithms for the mapping of acoutic sources," *12th AIAA/CEAS Aeroacoustics Conference, AIAA-2006-2711,* Cambridge, Massachusetts, May 2006.

[20] P. A. Ravetta, R. A. Burdisso, and W. F. Ng, "Noise source localization and optimization of phased array results," *12th AIAA/CEAS Aeroacoustics Conference, AIAA-2006-2713,* Cambridge, Massachusetts, May 2006.

[21] R. P. Dougherty, "Extensions of DAMAS and benefits and limitations of deconvolution in beamforming," *11th AIAA/CEAS Aeroacoustics Conference, AIAA-2005-2961,* Monterey, California, May 2005.

[22] T. F. Brooks and W. M. Humphreys, "Three-dimensional application of DAMAS methodology for aeroacoustic noise source definition," *11th AIAA/CEAS Aeroacoustics Conference, AIAA-2005-2960,* Monterey, California, May 2005.

[23] J. A. Högbom, "Aperture synthesis with a non-regular distribution of interferometer baselines," *Astronomy and Astrophysics Supplements*, vol. 15, pp. 417–426, 1974.

[24] T. F. Brooks and W. M. Humphreys, "Extension of DAMAS phased array processing for spatial coherence determination (DAMAS-C)," *12th AIAA/CEAS Aeroacoustics Conference, AIAA-2006-2654*, May 2006.

[25] D. L. Donoho and M. Elad, "Optimally sparse representation in general (nonorthogonal) dictionaries via ℓ^1 minimization," *PNAS*, vol. 100, pp. 2197–2202, March 2003.

[26] R. Tibshirani, "Regression shrinkage and selection via the lasso," *Journal of the Royal Statistical Society*, vol. 58, no. 1, pp. 267–288, 1996.

[27] S. S. Chen, D. L. Donoho, and M. A. Saunders, "Atomic decomposition by basis pursuit," *SIAM Journal of Scientific Computing*, vol. 20, no. 1, pp. 33–61, 1998.

[28] S. S. Chen, D. L. Donoho, and M. A. Saunders, "Atomic decomposition by basis pursuit," *SIAM Journal of Scientific Computing*, vol. 20, no. 1, pp. 33–61, 1998.

[29] J. A. Tropp, "Just relax: Convex programming methods for identifying sparse signals," *IEEE Transactions on Information Theory*, vol. 51, pp. 1030–1051, March 2006.

[30] J. J. Fuchs, "On sparse representations in arbitrary redundant bases," *IEEE Transactions on Information Theory*, vol. 50, no. 6, pp. 1341–1344, 2004.

[31] J. J. Fuchs, "Recovery of exact sparse representations in the presence of bounded noise," *IEEE Transactions on Information Theory*, vol. 51, no. 10, pp. 3601–3608, 2005.

[32] I. F. Gorodnitsky and B. D. Rao, "Sparse signal reconstruction from limited data using FOCUSS: A re-weighted minimum norm algorithm," *IEEE Transactions on Signal Processing*, vol. 45, no. 3, pp. 600–616, 1997.

[33] B. D. Rao and K. Kreutz-Delgado, "An affine scaling methodology for best basis selection," *IEEE Transactions on Signal Processing*, vol. 47, no. 1, pp. 187–200, 1999.

[34] K. Kreutz-Delgado, J. F. Murray, B. D. Rao, K. Engan, T. Lee, and T. J. Sejnowski, "Dictionary learning algorithms for sparse representation," *Neural Computation*, vol. 15, no. 2, pp. 349–396, 2003.

[35] B. D. Rao, K. Engan, S. F. Cotter, J. Palmer, and K. Kreutz-Delgado, "Subset selection in noise based on diversity measure minimization," *IEEE Transactions on Signal Processing*, vol. 51, no. 3, pp. 760–770, 2003.

[36] M. E. Tipping, "Sparse Bayesian learning and the relevance vector machine," *Journal of Machine Learning Research*, vol. 1, pp. 211–244, 2001.

[37] D. P. Wipf and B. D. Rao, "Sparse Bayesian learning for basis selection," *IEEE Transactions on Signal Processing*, vol. 52, no. 8, pp. 2153–2164, 2004.

[38] D. P. Wipf and B. D. Rao, "An empirical Bayesian strategy for solving the simultaneous sparse approximation problem," *IEEE Transactions on Signal Processing*, vol. 55, no. 7, pp. 3704–3716, 2007.

[39] M. A. T. Figueiredo, "Adaptive sparseness for supervised learning," *IEEE Transactions on Pattern Anal. Mach. Intell.*, vol. 25, no. 9, pp. 1150–1159, 2003.

[40] D. M. Malioutov, "A sparse signal reconstruction perspective for source localization with sensor arrays," Master's thesis, MIT, July 2003.

[41] D. M. Malioutov, M. Cetin, and A. S. Willsky, "A sparse signal reconstruction perspective for source localization with sensor arrays," *IEEE Transactions on Signal Processing*, vol. 53, no. 8, pp. 3010–3022, 2005.

[42] D. Malioutov, M. Cetin, and A. Willsky, "A sparce signal reconstruction perspective for source localization with sensor arrays," *IEEE Transactions on Signal Processing*, vol. 53, pp. 3010–3022, Aug. 2005.

[43] D. M. Malioutov, M. Çetin, and A. S. Willsky, "Source localization by enforcing sparsity through a laplacian prior: an svd-based approach," *IEEE Statistical Signal Processing Workshop*, pp. 553–556, 2003.

[44] T. Yardibi, J. Li, P. Stoica, M. Xue, and A. B. Baggeroer, "Source localization and sensing: A nonparametric iterative adaptive approach based on weighted least squares," *IEEE Transactions on Aerospace and Electronic Systems,* to appear.

[45] J. J. Fuchs, "Linear programming in spectral estimation. application to array processing," in *IEEE Proceedings of the Acoustics, Speech, and Signal Processing*, pp. 3161–3164, 1996.

[46] J. J. Fuchs, "On the application of the global matched filter to DOA estimation with uniform circular arrays," *IEEE Transactions on Signal Processing*, vol. 49, no. 4, pp. 702–709, 2001.

[47] C. Bahr, T. Yardibi, F. Liu, and L. N. Cattafesta, "An analysis of different measurement techniques for airfoil trailing edge noise," *14th AIAA/CEAS Aeroacoustics Conference, AIAA-2008-2957,* British Columbia, Canada, May 2008.

[48] D. T. Blackstock, *Fundamentals of Physical Acoustics*. New York, NY: John Wiley and Sons, 2000.

[49] G. H. Golub and C. F. Van Loan, *Matrix Computations*. Baltimore, MD: The John Hopkins University Press, 3rd edition, 1996.

[50] J. F. Sturm, "Using SeDuMi 1.02, a MATLAB toolbox for optimization over symmetric cones," *Optimization Methods and Software Online*, vol. 11-12, pp. 625–653, October 1999.

[51] J. Löfberg, "YALMIP: A toolbox for modeling and optimization in MATLAB," *The 2004 IEEE International Symposium on Computer Aided Control Systems Design*, pp. 284–289, September 2004.

[52] S. Boyd and L. Vandenberghe, *Convex Optimization*. Cambridge, United Kingdom: Cambridge University Press, 2004.

[53] T. Yardibi, J. Li, P. Stoica, and L. N. Cattafesta, "Sparsity constrained deconvolution approaches for acoustic source mapping," *The Journal of the Acoustical Society of America*, vol. 123, pp. 2631–2642, May 2008.

[54] J. S. Bendat and A. G. Piersol, *Random data: analysis and measurement procedures*. NY: Wiley, 2000.

[55] R. K. Amiet, "Refraction of sound by a shear layer," *Journal of Sound and Vibration*, vol. 58, no. 3, pp. 467–482, 1978.

[56] S. Oerlemans, L. Broersma, and P. Sijtsma, "Quantification of airframe noise using microphone arrays in open and closed wind tunnels," *International Journal of Aeroacoustics*, vol. 6, pp. 309–333, December 2007.

[57] P. Sijtsma, "Clean based on spatial source coherence," *International Journal of Aeroacoustics*, vol. 6, pp. 357–374, December 2007.

[58] T. Yardibi, C. Bahr, N. Zawodny, F. Liu, L. N. Cattafesta, and J. Li, "Uncertainty analysis of the standard delay-and-sum beamformer and array calibration," *15th AIAA/CEAS Aeroacoustics Conference, AIAA-2009-3120,* Miami, FL, May 2009.

[59] F. V. Hutcheson and T. F. Brooks, "Measurement of trailing edge noise using directional array and coherent output power methods," *International Journal of Aeroacoustics*, vol. 1, no. 4, pp. 329–354, 2002.

[60] J. A. Tropp, I. S. Dhillon, R. W. Heath, and T. Strohmer, "Designing structured tight frames via an alternating projection method," *IEEE Transactions on Information Theory*, vol. 51, pp. 188–209, January 2005.

[61] J. Li, P. Stoica, and X. Zheng, "Signal synthesis and receiver design for MIMO radar imaging," *IEEE Transactions on Signal Processing*, vol. 56, pp. 3959–3968, August 2008.

[62] P. Stoica, H. He, and J. Li, "New algorithms for designing unimodular sequences with good correlation properties," *IEEE Transactions on Signal Processing*, vol. 57, pp. 1415–1425, April 2009.

[63] W. Rudin, *Principles of Mathematical Analysis*. McGraw-Hill, 3rd ed., 1976.

[64] P. Stoica, J. Li, and X. Zhu, "Waveform synthesis for diversity-based transmit beampattern design," *IEEE Transactions on Signal Processing*, vol. 56, pp. 2593–2598, June 2008.

[65] M. Lobo, L. Vandenberghe, S. Boyd, and H. Lebret, "Applications of second-order cone programming," *Linear Algebra and its Applications, special issue on linear algebra in control, signals and image processing*, pp. 193–228, November 1998.

[66] M. Wax and T. Kailath, "Detection of signals by information theoretic criteria," *IEEE Transactions on Acoustics, Speech, and Signal Processing*, vol. ASSP-33, pp. 387–392, April 1985.

[67] H. W. Coleman and W. G. Steele, *Experimentation and uncertainty analysis for engineers*. NY: Wiley, 1998.

[68] T. Schultz, M. Sheplak, and L. N. Cattafesta, "Uncertainty analysis of the two-microphone method," *Journal of Sound and Vibration*, vol. 304, no. 1-2, pp. 91–109, 2007.

[69] P. Castellini and M. Martarelli, "Acoustic beamforming: Analysis of uncertainty and metrological performances," *Mechanical Systems and Signal Processing*, vol. 22, no. 3, pp. 672 – 692, 2008.

[70] B. D. Hall, "Calculating measurement uncertainty for complex-valued quantities," *Measurement Science and Technology*, vol. 14, pp. 368–375, 2003.

[71] B. D. Hall, "On the propagation of uncertainty in complex-valued quantities," *Metrologia*, vol. 41, pp. 173–177, 2004.

[72] T. Schultz, M. Sheplak, and L. N. Cattafesta, "Application of multivariate uncertainty analysis to frequency response function estimates," *Journal of Sound and Vibration*, vol. 305, no. 1-2, pp. 116–133, 2007.

[73] T. Suzuki, "Generalized inverse beamforming algorithm resolving coherent/incoherent, distributed and multipole sources," *14th AIAA/CEAS Aeroacoustics Conference, AIAA-2008-2954,* British Columbia, Canada, May 2008.

[74] C. Bahr, T. Yardibi, F. Liu, and L. N. Cattafesta, "Analysis of source denoising techniques," *The Journal of the Acoustical Society of America*, vol. 125, pp. 2538–2538, April 2009.

[75] L. Du, T. Yardibi, J. Li, and P. Stoica, "Review of user parameter-free robust adaptive beamforming algorithms," *Digital Signal Processing*, vol. 19, pp. 567–582, July 2009.

[76] J. Ling, T. Yardibi, X. Su, H. He, and J. Li, "Enhanced channel estimation and symbol detection for high speed multi-input multi-output underwater acoustic communications," *The Journal of the Acoustical Society of America*, vol. 125, pp. 3067–3078, May 2009.

[77] W. Roberts, P. Stoica, J. Li, T. Yardibi, and F. A. Sadjadi, "Iterative adaptive approaches to MIMO radar imaging," *IEEE Journal of Selected Topics in Signal Processing,* to appear,.

[78] T. Yardibi, J. Li, and P. Stoica, "Nonparametric and sparse signal representations in array processing via iterative adaptive approaches," *42nd Asilomar Conference on Signals, Systems and Computers,* Pacific Grove, CA, October 2008.

[79] T. W. Anderson, "Asymptotically efficient estimation of covariance matrices with linear structure," *The Annals of Statistics*, vol. 1, pp. 135–141, January 1973.

BIOGRAPHICAL SKETCH

Tarik Yardibi received his B.S. degree in electrical engineering from Hacettepe University, Ankara, Turkey in June 2004. He graduated with the highest GPA in the Faculty of Engineering at Hacettepe University. He received his M.S. degree in electrical engineering from Bilkent University, Ankara, Turkey in July 2006 and his Ph.D. degree in electrical and computer engineering from the University of Florida, Gainesville, FL, USA in August 2009. His research interests include statistical signal processing, array processing, aeroacoustic noise measurements, multiple-input multiple-output (MIMO) communications, radar/sonar signal processing, sparse signal representation and wireless sensor networks.